A multiscalar and multiproxy geoarchaeological approach to site formation processes at the Middle and Upper Palaeolithic site of La Roche-à-Pierrot, Saint-Césaire, France

Dominique Todisco, Carolina Mallol, Christelle Lahaye, Guillaume Guérin, François Bachellerie, Eugène Morin, Brad Gravina, Amélie Challier, Cédric Beauval, Jean-Guillaume Bordes, et al.

A multiscalar and multiproxy geoarchaeological approach to site formation processes at the Middle and Upper Palaeolithic site of La Roche-à-Pierrot, Saint-Césaire, France.

Dominique Todisco [a,*], Carolina Mallol [b, c, d,**], Christelle Lahaye [e], Guillaume Guérin [f], François Bachellerie [g,t], Eugène Morin [h], Brad Gravina [i,t], Amélie Challier [e,j], Cédric Beauval [k], Jean-Guillaume Bordes [t], Céline Colange [a], Laure Dayet [l], Damien Flas [m,n], François Lacrampe-Cuyaubère [k], Loïc Lebreton [o, p, q], Josserand Marot [r], Bruno Maureille [t], Alexandre Michel [s,t], Xavier Muth [u,v], Carole Nehme [a], Solange Rigaud [t], Elise Tartar [n], Nicolas Teyssandier [n], Marc Thomas [n], Hélène Rougier [w], Isabelle Crevecoeur [t]

a IDEES, UMR 6266, CNRS, Université de Rouen, Bâtiment 7, 17 rue Lavoisier, 76821 Mont Saint Aignan Cedex, France
b Instituto Universitario de Bio-Orgánica Antonio González, Universidad de La Laguna, Avda. Astrofísico Fco. Sánchez, 2. 38206 San Cristóbal de La Laguna, Tenerife, Spain
c Departamento de Geografía e Historia, UDI Prehistoria, Arqueología e Historia Antigua, Facultad de Humanidades, Universidad de La Laguna, 38206 San Cristóbal de La Laguna, Tenerife, Spain
d Department of Anthropology, University of California, One Shields Ave, Davis, CA 95616, USA
e Archéosciences Bordeaux, UMR 6034, CNRS, Université Bordeaux Montaigne, Maison de l'Archéologie, Esplanade des Antilles, 33607 Pessac, France
f Géosciences Rennes, UMR 6118, CNRS, Bâtiment 15, Campus Beaulieu, Université de Rennes 1, 35042 Rennes, France
g Archéologie Alsace, 11 rue Champollion, 67600 Sélestat, France
h Department of Anthropology, Trent University, DNA Block C, 2140 East Bank Drive, Peterborough, ON, K9J 7B8, Canada
i Musée national de Préhistoire, 1 rue du Musée, 24620 Les Eyzies-de-Tayac, France
j Department of Physics, Technical University of Denmark, DTU Risø Campus, 4500 Roskilde, Denmark
k SARL Archéosphère, 10 rue de la Rhode, 11500 Quillan, France
l EDYTEM, UMR 5204, CNRS, Université Savoie Mont Blanc, Bâtiment Pôle Montagne, 5 boulevard de la Mer Caspienne, 73376 Le Bourget du Lac Cedex, France
m Service de Préhistoire, Université de Liège, 7 Place du 20 Août, 4000 Liège, Belgium
n TRACES, UMR 5608, CNRS, Université de Toulouse Jean Jaurès, Maison de la Recherche, 5 allée Antonio Machado, 31058 Toulouse Cedex 9, France
o Institut Català de Paleoecologia Humana i Evolució Social (IPHES-CERCA), Zona Educacional 4, Campus Sescelades URV, Edifici W3, 43007 Tarragona, Spain
p Universitat Rovira i Virgili, Departament d'Història i Història de l'Art, Avinguda de Catalunya 35, 43002 Tarragona, Spain
q HNHP, UMR 7194, CNRS, Département Homme et Environnement du Muséum National d'Histoire Naturelle, CNRS-UPVD, Musée de l'Homme, 75116 Paris, France
r Service départemental de l'Archéologie, Maison du Département, 85 Boulevard de la République, 17076 La Rochelle Cedex 09, France
s Service départemental de l'Archéologie, Conseil Départemental de la Dordogne, 2 rue Paul Louis Courier, CS11200, 24019 Périgueux Cedex, France
t PACEA, UMR 5199, CNRS, Université de Bordeaux, Bâtiment B2, Allée Geoffroy Saint Hilaire, 33615 Pessac, France
u SARL Get in Situ, Place Rodolphe Théophile Bosshard 1, CH1097 Riex, Switzerland
v School of Engineering and Management Vaud, HES-SO University of Applied Sciences and Arts Western Switzerland, CH1401 Yverdon-les- Bains, Switzerland
w Department of Anthropology, California State University Northridge, 18111 Nordhoff St., Northridge, CA 91330-8244, USA

* Corresponding author.
** Corresponding author.
E-mail addresses: dominique.todisco@univ-rouen.fr (D. Todisco), cmallol@ull.edu.es (C. Mallol).

Keywords:
Geoarchaeology
Middle-to-Upper
Palaeolithic transition
Stratigraphy
Taphonomy
Micromorphology
Geochemistry

A B S T R A C T

The site of La Roche-à-Pierrot in Saint-Césaire (Charente-Maritime, France) produced a succession of Mousterian, Châtelperronian and Aurignacian occupations, and continues to play a central role in debates concerning the Middle-to-Upper Palaeolithic transition. The source of controversy surrounding the site relates to ambiguities concerning the overall archaeological sequence, the cultural association of the human remains found at the site and the limited number of robust absolute dates. Here, we present the results of a multiscalar, multiproxy geoarchaeological investigation of the site's sedimentary sequence. Our study integrates geomorphology, field lithostratigraphy, microstratigraphy, geochemistry and absolute dating methods (radiocarbon and optically stimulated luminescence) designed to characterize site formation processes. We propose a site formation model involving the evolution of a karstified limestone cliff from a semi-closed system to an exposed slope deposit, with sediments at the base of the cliff accumulating under periglacial conditions of MIS3, broadly between ca. 59.9 ± 3.9 ka and ca. 37.7 ka. The lowermost Mousterian occupations took place in a semi-closed, sheltered space in which sedimentary rates were low, involving mainly cryoclastic roof spall and episodic percolation of fine- grained sediment. This depositional environment generated a Mousterian archaeological palimpsest in the proximal area and translocated downslope. Subsequent Mousterian, Châtelperronian and Aurignacian remains embedded within diamictons were deposited in an open-air context, on a sloping surface at the apex of a palaeotalus, and possibly above the site, at the top of the cliff. The resulting diachronous surfaces and immature deposits were subject to solifluction and slopewash, with low sedimentary rates. Our geoarchaeological study sheds new light on previously noted spatial inconsistencies in the archaeological sequence and constitutes a rigorous framework for further archaeological research at the site, highlighting the potential of a multiscalar, multiproxy site formation research to improve stratigraphic investigation of Palaeolithic sites in similar geomorphological contexts.

1. Introduction

In western Europe, the transition between the Middle Palaeolithic (MP) and Upper Palaeolithic (UP) is associated with a mosaic of so-called "transitional" industries (e.g., the Châtelperronian, Uluzzian and Szeletian) that precede the first phases of the Aurignacian (Bon, 2002; Conard and Bolus, 2003, 2008; Teyssandier, 2008; Higham et al., 2014; Talamo et al., 2020). From a biological point of view, this period is also marked by the disappearance of the last Neanderthals and the arrival of the first representatives of *Homo sapiens* in Europe (Stringer et al., 1984; Vandermeersch and Hublin, 2007; Peresani et al., 2019; Hublin et al., 2020; Slimak et al., 2022). The concomitance of these two upheavals, biological and cultural, and the authors of transitional industries are at the heart of current debates concerning the degree of interaction between these two human populations.

The site of La Roche-à-Pierrot in Saint-Césaire (Charente-Maritime, France; Fig. 1) occupies a central place in debates concerning the Middle-to-Upper Palaeolithic transition because it yielded an exceptional sequence of Mousterian, Châtelperronian and Aurignacian occupations. The site is one of the few to have yielded a relatively complete Neanderthal skeleton, "Saint-Césaire 1". Discovered in 1979, the skeleton was reported as deriving from a level containing a Châtelperronian industry (Lévêque and Vandermeersch, 1980; Lévêque, 1993), a technocomplex considered at the time to have been made by the first *Homo sapiens* in Europe. This discovery has raised questions concerning the nature of Neanderthal-*Homo sapiens* interactions as well as Neanderthal cognitive abilities and behaviour (Trinkaus and Shipman, 2005), a process that continues as the chrono-cultural context of the Saint-Césaire 1 skeleton remains controversial (Bar-Yosef and Bordes, 2010; Gravina et al., 2018). As is the case with numerous other

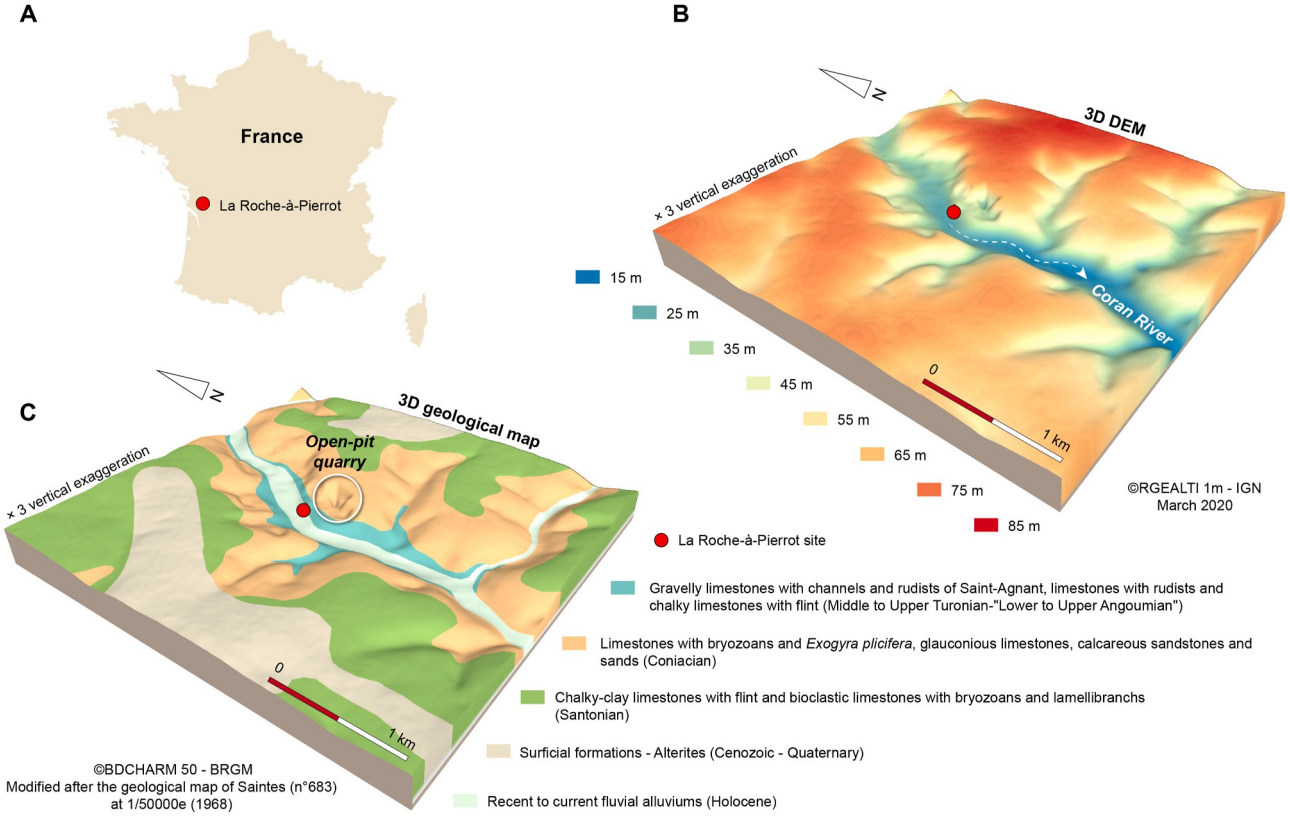

Fig. 1. Context of La Roche-à-Pierrot. A: Map of France with the location of the site (red dot). B: Three-dimensional digital elevation model (DEM) showing the Coran River incision. C: Geological map of the limestone plateau, surficial formations, and Coran River valley where the site is located (white circle: open-pit quarry). The three-dimensional models were created using QGIS software with the QGIS2threejs extension.

Middle-to-Upper Palaeolithic sequences, controversies at La Roche-à-Pierrot revolve around problems of stratigraphic ambiguity, the context of the human remains, and the limited number of robust absolute dates. In addition, the site has never been the subject of an in-depth geomorphological or geoarchaeological investigation.

In 2013, a perceived gap between the published information about the site and its importance in debates surrounding the replacement of the last Neanderthals by the first *Homo sapiens* motivated the resumption of multi-disciplinary research at the site. This included a multiscalar, geoarchaeological investigation of the site combining geomorphology, field stratigraphy, microstratigraphy, geochemistry and absolute dating with a focus on site formation processes. Here, we present the results of this research programme and discuss some of the implications for our understanding of the Middle-to-Upper Palaeolithic transition.

1.1. Geomorphological setting

La Roche-à-Pierrot is a gently sloping, open-air sedimentary deposit with an approximate maximum thickness of 4 m resting against a 6 m high limestone cliff. The site is located on the left bank of the Coran, a

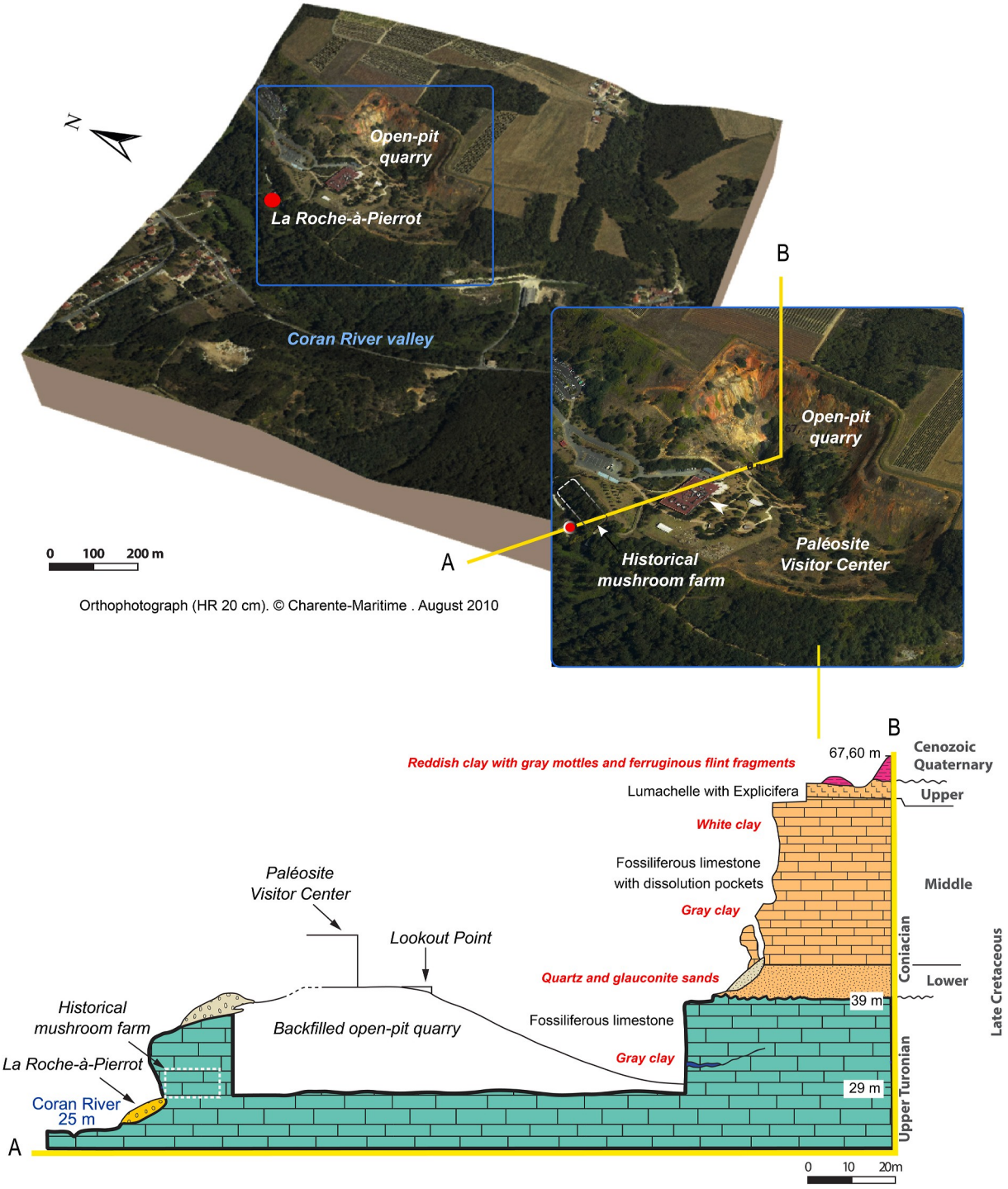

Fig. 2. View of the open-pit limestone quarry on an orthophotograph of the site's surroundings, and a schematic geological section from the Coran River to the periphery of the quarry. The three-dimensional section was created using QGIS software with the QGIS2threejs extension.

tributary of the Charente River (Fig. 1), at an altitude of 28 m above sea level (asl), and 2–4 m above the current floodplain of the Coran. This stream runs NE/SW along the back of a Cretaceous limestone cuesta, the "*Cuesta de Saint-Césaire*" (Bourgueil et al., 1968; Sellier, 2010). Near the site, the cliff face is dotted with a series of abandoned limestone quarries converted into a mushroom farm ("*champignonnière*"). These quarries feature small galleries or chambers cut into the bedrock, including a chamber adjoining the site and connected to a karstic diaclase.

The bedrock consists of Upper Turonian limestone. The section visible in an open-pit limestone quarry located around 200–280 m from the archaeological site shows a Late Cretaceous lithostratigraphy including from base to top (Fig. 2): 1) Upper Turonian fossiliferous limestone; 2) Middle Coniacian fossiliferous limestone with a bed of massive quartz and glauconitic sand at its base; and 3) Cenozoic/Quaternary reddish clay (alloterites) containing subrounded ferruginous flint fragments. The Turonian limestone is chemically weathered with karstification features (including isalterites) while the Coniacian limestone exhibits dissolution pockets or whitish alloterites.

1.2. Archaeostratigraphy of the site

Three main stratigraphic units have previously been identified at the site based on sedimentological, colorimetric, and archaeological (lithic typology) criteria observed in the main excavation profiles, particularly the reference section, in the proximal sector (the area closest to the cliff) (Miskovsky and Lévêque, 1993; Fig. 3; see SOM-Section 1, for the history of excavations; Fig. S1). From base to top, these units, originally called "*ensembles*", include: 1) a sterile, reddish unit at the base, followed by 2) a grayish unit (lower archaeological sequence) containing Middle Palaeolithic remains, subdivided into eight stratified levels, and 3) a yellowish unit (upper archaeological sequence) at the top containing stratified Mousterian, Châtelperronian (including the Saint-Césaire 1 partial Neanderthal skeleton), and Aurignacian material. This last unit was subdivided into seven levels based on the same criteria. Thermoluminescence (TL) dating indicated that flints from levels EGPF toEJO-sup. were last exposed to heat between roughly 42.4 4.8±and 32.13 ka, ± with a mean age of 36.3 ± 2.7 ka for the level (EJOP-sup) initially attributed to the Châtelperronian (Mercier et al., 1991, 1993).

Part of the lithics and a large majority of the faunal remains from La Roche-à-Pierrot have since been studied and dated by different researchers, resulting in more detailed information and new interpretations of the assemblages from the different stratigraphic layers.

Low collagen radiocarbon dates were obtained from animal bone remains, providing rough minimal ages of 42.5–52.2 cal BP for Mousterian level EGPF and 39.9–42.1 cal BP for Châtelperronian level EJOP-sup. (Higham et al., 2014; Oxcal 4.4, IntCal 20; Reimer et al., 2020). An additional radiocarbon age of *ca.* 40–42.2 cal BP was obtained from a fragment of the Saint-Césaire 1 skeleton albeit with a low collagen yield (0.77%; Hublin et al., 2012; Oxcal 4.4, IntCal 20; Reimer et al., 2020).

With respect to the archaeological assemblages, the Mousterian level EGPF has been the focus of a detailed analysis that examined its exceptional preservation and high artefact density (Thiébaut, 2005; Thiébaut et al., 2009; Morin, 2012). This contained a Denticulate Mousterian (DM) associated with the exploitation of ungulates (bison, reindeer and horse; Morin, 2012). The overlying EJOP level was reassessed with an emphasis on the archaeostratigraphic provenience of the remains, with the results indicating that:

- The basal part of EJOP (EJOP inf.) contains concentrations of boulders and a small number of artefacts, concentrated primarily towards the top of the unit. Like EGPF, EJOP inf. contains a Mousterian industry and a high representation of ungulates (Soressi, 2010, 2011; Morin, 2012).
- The EJOP sup. archaeological remains are again more abundant towards the top of the unit. This occupation is associated with the procurement of reindeer, bison and horse (Lavaud-Girard, 1993; Patou-Mathis, 1993; Morin, 2012). A detailed typo-technological and spatial analysis of a large sample of this unit's lithic assemblage demonstrated that it contains an overwhelming Mousterian component accompanied by a small fraction of Châtelperronian objects and that these two components are stratigraphically indistinguishable (Bachellerie, 2011; Gravina et al., 2018). Moreover, two-thirds of the artefacts larger than 4 cm in this mixed assemblage show mechanical edge damage, percussed ridges and heavily pati- nated surfaces (op. cit.; see also Galland et al., 2019). The assemblage also contains a substantial proportion of geofacts derived from geological outcrops found above the site. These features, combined with the strong dip and preferential strike of the artefacts between rows 6 and 9, led Gravina et al. (2018) to conclude that the EJOP sup. lithic assemblage is a syn-depositional mix of *in situ* and reworked Mousterian and Châtelperronian occupations derived in part from occupations overlying the site. Finally, this study demonstrated that the Saint-Césaire I Neanderthal remains cannot be reliably associated with either chrono-cultural component in Lévêque's EJOP sup.

No new analyses have been carried out of the EJO lithic assemblage. The faunal assemblage shows a marked increase in reindeer representation relative to the underlying units (Morin, 2010, 2012). For the upper part of the archaeological sequence (proximal area of the site), taphonomic analysis of small mammal remains indicate periods during which the site was abandoned or only sporadically occupied (Lebreton et al., 2021). Likewise, the EGC assemblage, which Lévêque and Vandermeersch (1980) assigned to the Mousterian of Acheulean Tradition (MAT), has not been reanalysed. An examination of the faunal remains from Levêque's excavation led to the discovery of two Neanderthal perinatal individuals from the basal part of the unit (Colombet, 2012; Colombet et al., 2012).

2. Material and methods

2.1. Material

This study is based on geomorphological observations, dating, and different analysis of sediment samples from the open-pit quarry, along with four stratigraphic sections from the archaeological site and an isolated sedimentary deposit from the mushroom farm located behind the site (SOM-Sections 2.1, 2.2, 2.3; Figs. S2 to S12). For this study, we focused on the sagittal and frontal sections of Lévêque's excavation and its extension (rows JKLM) in the current excavation (Fig. 3), which preserves the sequence described by F. Lévêque.

2.2. Field observations and sampling

In the field, all the exposed profiles were described with a focus on sediment texture, structure, colour attributes (hue, chroma) and stratigraphic contacts. Samples were collected for both OSL and ^{14}C dating as well as a series of bulk and oriented sediment samples for geochemistry analyses and micromorphology (Tables S1, S2, S3). We also carried out a fabric analysis of the archaeological remains to explore possible (post) depositional processes (Fig. S13). Analytical results are presented and discussed in relation to the macrofacies and the new lithostratigraphy established from field observations (Fig. S14).

2.3. X-ray diffraction (XRD)

XRD analyses targeted mineralogical characterization of the fine fraction to ascertain potential sedimentary sources. Specifically, the goal was to differentiate between endokarst sediments, including isalterites, and surficial formations, especially alloterites. Thirty-six bulk sediment samples were collected at the site, the mushroom farm behind the site and the open-pit limestone quarry exposures (Figs. S2-S7; Tables S1, S4, S5). XRD analyses were performed on non-oriented powder from a 53-

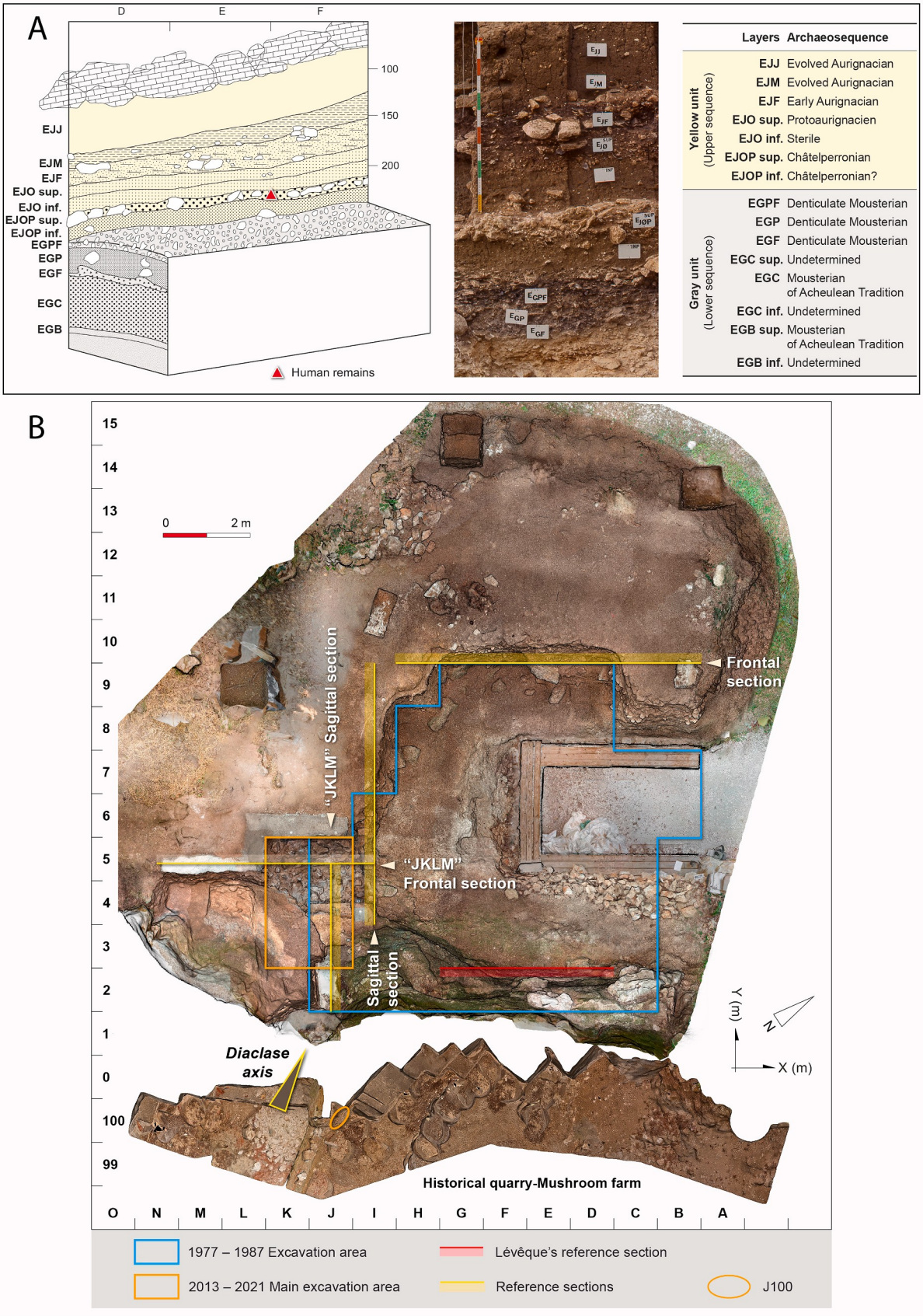

Fig. 3. A: Schematic representation (left) and photograph (middle) of the reference section from Lévêque's excavation at La Roche-à-Pierrot, and description of the associated archaeological sequence (right) (following Miskovsky and Lévêque, 1993; Lévêque, 1997). The red triangle indicates the location of the Saint-Césaire 1 Neanderthal remains. B: Zenithal orthophotograph of the La Roche-à-Pierrot (top) and the historical quarry-mushroom farm (bottom). The area corresponding to Lévêque's excavation is indicated as well as the current excavation area and the reference sections discussed in the text.

μm sieve by the XRD Analytical and Consulting Laboratory in Pretoria, South Africa, using a PANalytical Empyrean/Aeris diffractometer. Crystalline phases or mineral groups were identified using X'Pert Highscore Plus software, and relative percentages were quantified through the Rietveld refinement method (SOM-Section 2.4).

2.4. Inductively coupled plasma-optical emission spectrometry (ICP-OES) and inductively coupled plasma-mass spectrometry (ICP-MS)

Like the XRD analyses, samples were examined to determine sediment source, resulting in a dataset of 35 samples (intra-, peri- and off-site; Figs. S2-S7 and Table S1). Multi-element analysis was carried out at the CNRS, Centre de Recherches Pétrographiques et Géochimiques (CRPG), Vandoeuvre-lès-Nancy, France. Major and minor element dose percentages (SiO_2, Al_2O_3, total Fe_2O_3, MnO, MgO, CaO, Na_2O, K_2O, P_2O_5, TiO_2; Table S6) were measured through inductively coupled plasma optical emission spectroscopy using an ICP-OES iCap6500 ThermoFisher instrument. In addition, the loss on ignition (LOI) was determined by gravimetric analysis (calcination at 1000 °C). The concentrations of 43 additional trace elements (μg/g; ppm) were measured through inductively coupled plasma mass spectrometry using an ICP-MS iCapQ ThermoFisher instrument (Carignan et al., 2001). From these, we used the 10 trace elements showing the highest inter-sample variability (standard deviation > 20: Ba, Cr, Nb, Ni, Rb, Sr, V, Zn, Zr, Ce; Table S7). A principal component analysis (PCA) using a variance-covariance matrix was performed with the Past software (PAleontological STatistics; Hammer et al., 2001). Biplots with 95% concentration ellipses were generated to compare geochemical observations and variables simultaneously on a multidimensional dataset (components 1 and 2).

2.5. Micromorphology

In order to complete the description of the lithofacies, a micromorphological analysis was carried out (Fig. S15; Table S8). Forty-eight micromorphological samples were collected between 2013 and 2021 from the excavation profiles and surfaces, as well as from different areas outside the site (test pits above the cliff, bedrock samples from the limestone quarry and from square J100 in the mushroom farm) (Figs. S2-S6 and Table S2). The micromorphological samples were removed intact using plaster strips and processed into petrographic thin sections by different manufacturers (SOM-Section 2.5).

2.6. Fabric analysis

To explore and assess the possible impact of different taphonomic processes, such as solifluction, overland flow and bioturbation (Schick, 1987; Bertran and Texier, 1995; Lenoble and Bertran, 2004; Lenoble, 2005; McPherron, 2005, 2018; Lenoble and Agsous, 2013), we analysed the fabric of the lithic and bone remains from Mousterian to Aurignacian units with diamictic facies in the site's proximal area (squares J3, J4, J5, K4, K5). The fabric analysis examines the orientation and long axis dip of the longest archaeological objects (elongation axis >2 cm) for which measurements were available. A total of 662 measurements were used after being taken in the field during excavation with a compass and an inclinometer.

Fabric distributions were then examined using different tests derived from the field of circular statistics (Batschelet, 1981; Fisher, 1993; Landler et al., 2018; SOM-Section 2.6; Tables S9 to S12). Stereograms (Schmidt's lower hemisphere projection, equal-area), analyses of the statistical significance of point concentration/density (Kamb contouring method), as well as calculation of the conical best fit, and the Fisher mean vector for archaeological assemblages were performed using Stereonet software (Allmendinger et al., 2011). The statistical characterization of the tested squares used elongation (EL) and isotropy (IS) indices, based on the ratio of the normalized eigenvectors E1, E2 and E3 (Benn, 1994). These indices allow us to plot the fabric distributions on a triangular diagram where they can be compared with that of natural (fossil or actual) and experimental sites (Lenoble and Bertran, 2004; Lenoble and Agsous, 2013; McPherron, 2018).

2.7. Dating

To produce a robust chronology for the deposits, we combined radiocarbon data obtained on faunal remains with an optically stimulated luminescence (OSL) analysis of the sediments from the entire archaeological sequence (SOM-Sections 2.7 and 2.8; see Table S3 for sample descriptions and Figs. S2-S6 for their provenience). The radiocarbon dates were produced by the Oxford Radiocarbon Accelerator Unit at the University of Oxford. The collagen samples were, depending on their size, ultrafiltrated (Brown et al., 1988; Higham et al., 2006) or subjected to gelatinization filtration (Talamo and Richards, 2011) prior to being dated by accelerator mass spectrometry (AMS). The C-11 date was obtained on the humin fraction of the sediment (alkali-insoluble organics) by Beta Analytic. All the results were calibrated using the OxCal program version 4.4 (Bronk Ramsey, 2021) and the IntCal 20 curve (Reimer et al., 2020) (Table S13). Eighteen sedimentary samples were collected for luminescence dating between 2013 and 2019. Two of them were not suitable for dating, due to a lack of quartz and feldspars in sufficient quantities. The remaining ($n = 16$) samples were dated either by multi-grain (O-2, O-7 to O-9, O-11 and O-12) or single-grain (O-1,O-3 to O-6, O-10, O-13, O-14 to O-16) (Table S3) OSL on quartz (Huntleyet al., 1985; Murray et al., 2021).

The samples were collected by scraping sediment from the exposed profiles under controlled light conditions (dim orange light). The first ~1.5 cm of sediment, exposed to daylight during excavation, was used for dose-rate measurements. The rest of the sample was collected in black bags for luminescence measurements. Sediment samples were prepared mechanically and chemically under controlled light conditions (Wintle, 1997). The samples were wet-sieved to separate the different fractions (20–41 μm for O-7 to O-9; 180–250 μm or 200–250 μm for the others). Each selected fraction was treated with hydrochloric acid (HCl, 10%) to remove carbonates, rinsed, and then treated with hydrogen peroxide (H_2O_2, 30%) to remove organic matter.

For the samples prepared as fine-grain fractions (20–41 μm), a 1-week H_2SiF_6 treatment was applied to remove feldspars, followed by standard HCl 10% treatment to remove fluorine potentially formed during the preceding step, and finally rinsed 3 times in H_2O and sieved again through a 20 μm mesh. During the process of sand fraction (180–250 or 200–250 μm) selection, a three-step separation protocol was carried out using a different aqueous solution of sodium heteropolytungstate with controlled densities (2.58, 2.62 and 2.72 g cm^3) to isolate K-rich feldspars (<2.58 g cm^3) and quartz-rich (>2.62 g cm^3 and <2.72 g cm^3) fractions. After separation, the quartz fraction was treated with hydrofluoric acid to etch the external part of the grains which were submitted to alpha irradiation during burial. A successive HCl 10% (to remove eventually formed CaF_2) treatment was applied, followed by rinsing in demineralized water and by 180 or 200 μm wet sieving. For multi-grain (MG) measurements, the quartz grains were mounted on stainless steel cups, 9 mm in diameter, using silicone oil. Single-grain (SG) measurements were performed by inserting 1 grain in each hole in aluminum cups drilled with 100 holes of 300 μm in diameter and 300 μm deep.

Luminescence measurements were conducted using two blue light-emitting diodes (470 nm) Risø TL/OSL DA-20 readers (Bøtter-Jensen et al., 2003), coupled with 7.5 mm Hoya U-340 detection filters and with a green laser (532 nm) used with a 7.5 mm Hoya U-340 detection filter. Samples from 2014 (O-7 to O-9) were dated using a Daybreak 2200 OSL reader (Bortolot, 2000), equipped with a calibrated $^{90}Sr/^{90}Y$ beta source, with green LEDS (Nichia NSPG310) emitting at 515 nm (maximum power of 30 mW/cm^2). The signals were measured after selection by optical filters (U340 7.5 mm). The single-aliquot regenerative doses protocol (SAR; Table S14) (Wintle and Murray, 2000;

Murray and Wintle, 2003) was adopted for all 16 samples. Pseudo-LM OSL curves showed that the signal is dominated by the fast component (Bailey et al., 1997; Jain et al., 2003; Bos and Wallinga, 2012). A preheat plateau test was performed on different samples and did not show substantial or systematic variations in equivalent doses (De) values (Fig. S16). Preheat temperatures were chosen according to measurements of 200 °C or 220 °C for 10s, depending on the samples. Dose recovery tests (DRT) were also performed (Table S15). Average Dose Model (ADM: Guérin et al., 2017) was applied to all samples as well as the Finite MiXture Model (FMM: Galbraith and Green, 1990) to one sample (O-5) potentially showing a miXing of two different quartz grain populations. Equivalent doses as well as intrinsic (σ_m, from DRT measurements) and extrinsic (σ_d, from ADM) overdispersions have been determined for multi-grain (MG)-dated samples (Table S16) and single-grain (SG)-dated samples (Table S17). Analysis of the abanico plots of the SG-dated samples with De distributions (Fig. S17), and extrinsic (σ_d) values (Table S17), enabled any suspicion of incomplete bleaching to be assessed.

The sediment fraction that was exposed to daylight in the section before measurement was used to determine the sample's radioelements content. The water content (WC) at the time of collection was measured for each sample and a mean value adopted by groups of samples. The dried sediments were sieved (<2 mm), crushed, and packed in plastic boXes suited for High Purity Low Background Broad Energy Germanium gamma spectrometry measurements (Guibert and Schvoerer, 1991). The measured KUTh contents (Fig. S18; Table S18) was used to determine the alpha and beta contributions to the dose-rate using the dose-rate conversion factors from Guérin et al. (2011). Al_2O_3:C dosimeters (Richter et al., 2010; Kreutzer et al., 2018) were inserted for a minimum period of 12 months, at the precise location or very close to the sediment sampling point. These dosimeters allowed us to measure the environmental contribution (gamma and cosmic) to the total dose-rate. In three cases (O-14–O-16) the archaeological context did not allow the insertion of dosimeters in the profiles. In these cases, the gamma contribution was calculated based on the KUTh content, and the cosmic dose-rates were determined considering the burial depth of each sediment (Prescott and Hutton, 1988). Grain size attenuation factors for beta dose rates were taken from Guérin et al. (2012).

3. Results

3.1. Geomorphological observations

At the top of the cliff, just above the site, we identified archaeologically sterile, reddish clayey deposits containing ferruginous flint fragments (alloterites) similar to those that cap the geological sequence at the open-pit quarry (Fig. 2). At the site, the limestone cliff was heavily modified by historical quarrying activity. Behind the site, however, inside the mushroom farm, we observed vertical karstification features, including a chimney indicative of former dissolution by ascending flow, and other features indicative of karstogenesis such as small domes, several small dissolution pockets and a truncated, infilled (plurimetric) alveolus (large pocket) at the entrance that communicates with the surface (Figs. S8 and S9). Grayish compact alterites, with a banded structure and residual weathered limestone, occur around 29–31 m asl (6 m above the Coran alluvial plain) in association with the base of the chimney. These clayey residual alterites likely result from ghost-rock karstification (Dubois et al., 2014, 2022) and are interpreted as *in situ* weathering of the bedrock (isalterites) leaving the undissolved components in place. Locally, endokarstic features show a connection with the surface as evidenced by the presence of recent components such as rootlets and allochthonous components, including quartz sand. The Upper Turonian fossiliferous limestone also exhibits ferruginous Liesegang bands (at around 31 m asl) likely associated with a palaeo-piezometric level (Figs. S7 and S8). Outside the mushroom farm, on the cliff, we identified small-sized dissolution alveoli or vertical microkarrens carved in the bedrock. Upstream, on the banks of the Coran and near to the site, we identified a small, perched fossil subhorizontal drain (partially channelled), also likely associated with a palaeo-piezometric level. Away from the site, in the open-pit limestone quarry, we similarly observed incipient karstification features (ghos- t-rock weathering) in the Upper Turonian and Middle Coniacian limestone (grayish residual clay) (Fig. 2 and Fig. S10).

3.2. Field lithostratigraphy

3.2.1. Unit 1

Overlying the Turonian limestone bedrock, the basal part of the sequence (Unit 1) is made up of locally bedded and NW sloping, weathered, angular to subangular, centimetric, platy, white to very pale gray limestone clasts (pebbles and cobbles) in a yellowish, clayey, calcitic pseudo-sand matriX (Figs. 4, 6–8 and Fig. S14). The matriX is variably loose or compact, and granular (Facies 1a) or variably indurated (Facies 1b). At the proximal end of the sloping deposit (JKLM section), the top of Unit 1 exhibits a very pale brown to pale gray colour (Facies 1c). This unit contains few archaeological remains, mostly small (centimetric) faunal remains.

3.2.2. Unit 2

Overlying Unit 1 with a diffuse contact lies a massive matriX-supported diamicton (Unit 2; Figs. 4–8 and Fig. S14) consisting of a brownish variably pale gray to grayish pale brown sandy clay to clayey/silty sand with frequent weathered limestone pebbles and cobbles and sparse, weathered, platy clasts (Facies 2a). This layer is variably loose or compact and shows localized diffuse calcitic or redoXimorphic features (Facies 2b). It contains abundant archaeological lithic and faunal remains, some of which are vertically oriented at the slope break of the sagittal section, bedded and sloping towards the NW on the frontal section.

3.2.3. Unit 3

Unit 2 is overlain by Unit 3 with a diffuse contact (Figs. 4–8). Unit 3 is a predominantly massive, clast-supported diamicton composed of angular to subangular limestone pebbles, cobbles, and metre-sized boulders in a brownish yellow to yellowish-brown clayey to silty-sandy matriX (Facies 3a), the sediment being clayier at the base (Figs. S11 and S14). Fig. S12 shows a field view of the diamictic Facies 3a at the JKLM area, during new excavation (Fig. 3). Noteworthy is the feature found in square J5, a concentration of imbricated archaeological remains and clasts exhibiting a small buried lobate morphology. Facies 3a also shows scattered zones with calcitic features such as calcium carbonate induration or concentrations of weathered limestone clasts. Downslope, in rows 6–7, the matriX becomes olive-brown to yellowish-gray or pale yellowish gray, with redoXimorphic features. At the summit of the palaeotalus, corresponding with the JKLM area and the proXimal sagittal section, Unit 3 shows a concentration of weathered limestone clasts. In the proXimal sagittal section area, imbricated limestone boulders dipping strongly to the NW and resting on a locally compact, whitish, calcitic, silty to sandy layer, are present (Facies 3b). In the JKLM area, this whitish calcitic layer is not associated with boulders and rests against the cliff wall (Facies 3c). Locally, in the sagittal profile, Facies 3b is underlain by a lens of loose sandy clay (Facies 3d).

In the main sagittal section, the density of boulders in Unit 3 decreases downslope along with a change in the matriX colour towards grayish brown/olive grayish brown. In this zone, the matriX is also more compact and contains localized concentrations of imbricated archaeological remains at the downslope side of the boulders (Facies 3e). Further downslope, beyond the slope break towards the NW, the boulders also dip to the NW, and in the sagittal and frontal sections, the sediment exhibits lateral variability in colour (brown to pale brownish yellow/yellowish brown, Facies 3f), a localized presence of reddish pedogenic features (more pronounced in the distal part of the frontal

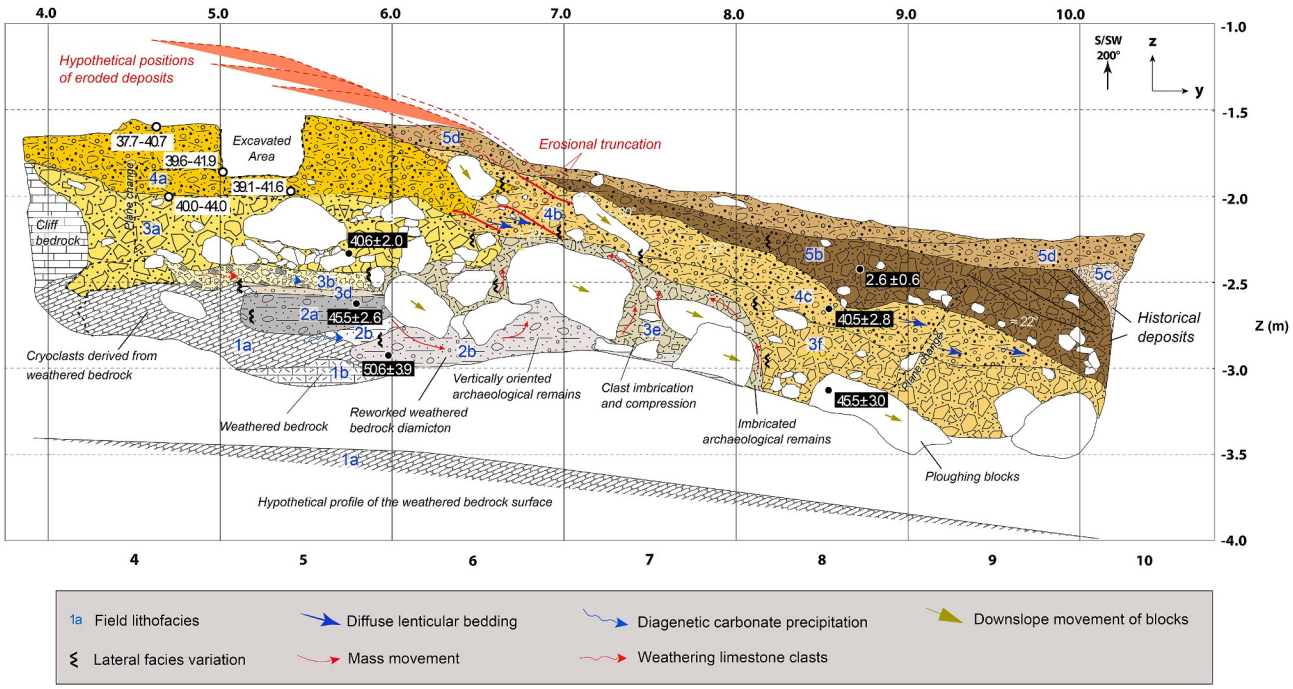

Fig. 4. Illustration of the lithostratigraphic units and subunits observed in the main sagittal section (*cf.* Fig. S14 for facies descriptions) with OSL (black dots) and 2 sigma calibrated ^{14}C (white dots) dates.

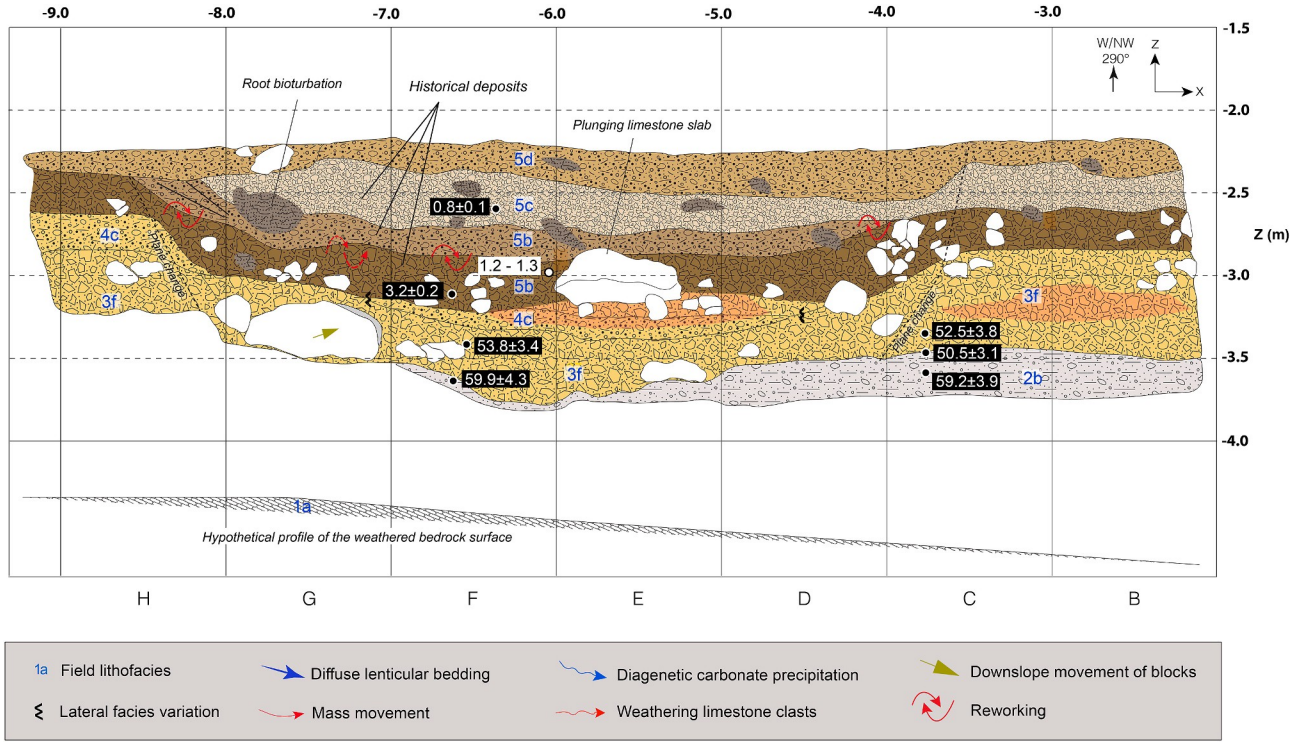

Fig. 5. Illustration of the lithostratigraphic units and subunits observed in the main frontal section (*cf.* Fig. S14 for facies descriptions) with OSL (black dots) and ^{14}C (white dot) dates. For Facies 5b, the ^{14}C age is 1343-1176 cal BP (2 sigma).

section) and bioturbation. A capping of Facies 3a sediment was observed on the frontal (downslope) face of one of the boulders.

3.2.4. Unit 4

Unit 4 is a matrix-supported diamicton overlying Unit 3 with a sharp contact (Figs. 4–8 and Fig. S14). It contains frequent limestone pebbles. These are variably weathered, subrounded, exhibit very diffuse and localized lenticular bedding, and are embedded in a brownish yellow to yellowish-brown clayey to silty-sandy matrix (Facies 4a; Fig. S11). There are localized calcitic or redoximorphic features and root bioturbation (Facies 4b). Downslope, at the slope break visible in the sagittal section, there are two strongly dipping boulders, a change in texture (sandier)

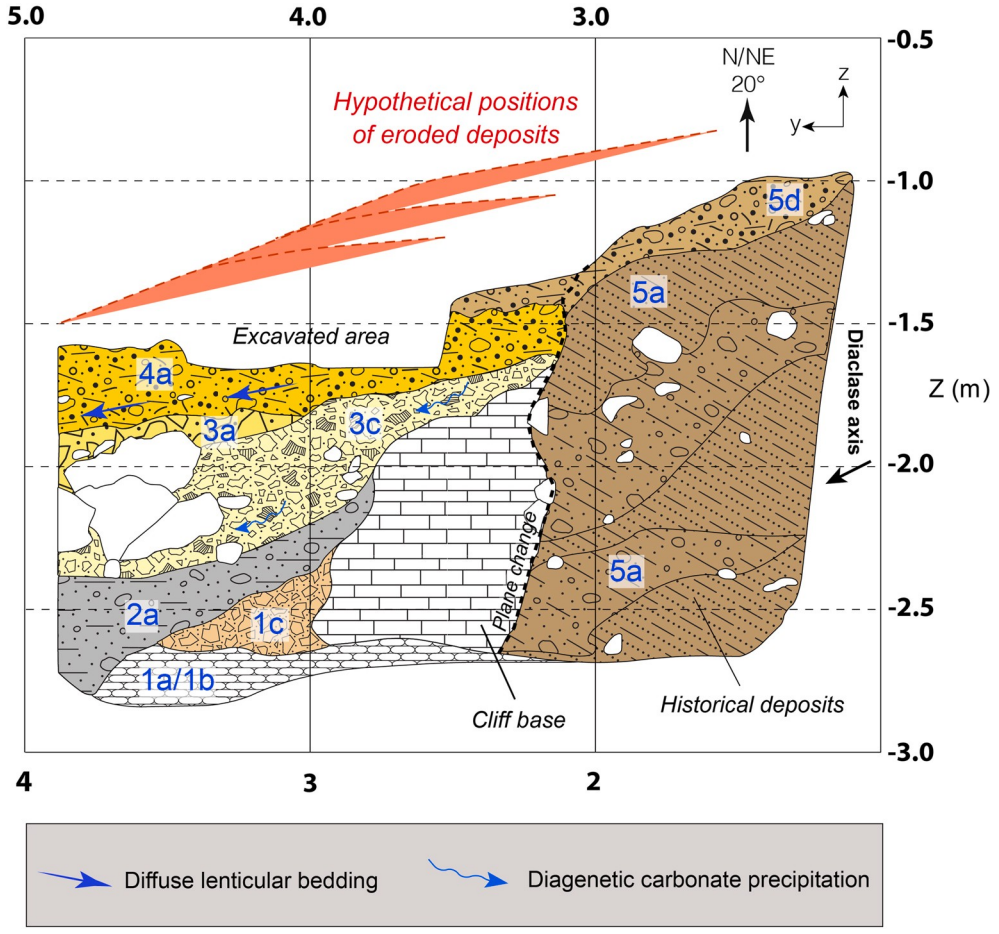

Fig. 6. Illustration of the lithostratigraphic units and subunits in the JKLM sagittal section (*cf.* Fig. S14 for facies descriptions).

and colour (darker; brown), and localized diffuse fine bedding of the pebble fraction (Facies 4c).

3.2.5. Unit 5

Capping the stratified sequence is Unit 5, which overlies Unit 4 with a sharp contact (Figs. 4–8 and Fig. S14). It is a succession of historical, anthropoturbated pedo-sedimentary facies. These are poorly sorted, matrix- or clast-supported, bioturbated diamictons with possible variable organic content, as suggested by the variable colour of the matrix (different shades of dark brown and grayish dark brown). On the sagittal section at the JKLM area there is a zone of interstratification of limestone clasts and matrix-supported facies (Facies 5a) resting against the cliff wall. The frontal JKLM section shows Facies 5a directly overlying bedrock. These uppermost deposits conform to the general dip of the underlying units. At the sagittal and frontal sections, Unit 5 is visibly organic-rich and exhibits localized diffuse bedding (Facies 5b), sloping towards the NW on the sagittal section. On the frontal section, Unit 5 is clast-supported, better sorted, and poorly stratified (Facies 5c), and exhibits pseudo-channel structures at the basal contacts of all facies, particularly 5b and 5c. The present-day anthroposol (Facies 5d) is visible on the sagittal and frontal sections and includes the backfills of the earlier excavations.

3.2.6. Unit Q1

In a small area within the mushroom farm behind the site (square J100), near the JKLM zone (axis of the diaclase; Fig. 3), there is an exposed sedimentary deposit showing two distinct facies (Fig. S6). The upper facies (Facies Q1a) shows a brownish-yellow, compact sandy clay with calcitic laminae. This facies contains very few faunal remains and lithic objects. The lower facies (Facies Q1b) is a very pale brown to very pale yellow, clayey, calcitic sand overlying weathered Turonian limestone bedrock. This facies contains a very few unburnt and burnt bone fragments.

3.3. Geochemistry and sediment sourcing

The XRD analysis identified six main crystalline phases (quartz, kaolinite, muscovite, calcite, goethite, and smectite) and four secondary phases (apatite, biotite, plagioclase, and microcline) in the sediment (Tables S4 and S5). XRD performed on unoriented powders provided complete spectra of the tested samples with the peaks corresponding to all possible particle orientations (Larqué, 2002). The principal component analysis shows an opposition in the crystalline phases between the intra-site and extra-site samples. In PC1, calcite (negative loading), quartz, kaolinite, and smectite (positive loading) are the most discriminant phases (Fig. 9A). In PC2, quartz (negative loading) is the most discriminant variable, followed by kaolinite and smectite (positive loading). Among the intra-site samples, there is a clear opposition between the sediments derived from the Turonian limestone bedrock (G-14 and G-15) and those from the frontal section associated with historical anthropoturbation (G-23 and G-24), located towards the quartz pole. Note the dual position of the square J100 samples from the mushroom farm. This is due to the elevated calcium carbonate content of sample G-34 (Facies Q1b), which is adjacent to the weathered Turonian limestone wall. Facies Q1a (G-35) plots with the intra-site samples, close to samples G-21 and G-31. Also included in this group is sample G-9 from the dissolution fissure feature aligned with the diaclase axis behind the JKLM zone of the site (the highest area of the stratified deposit; Fig. 3).

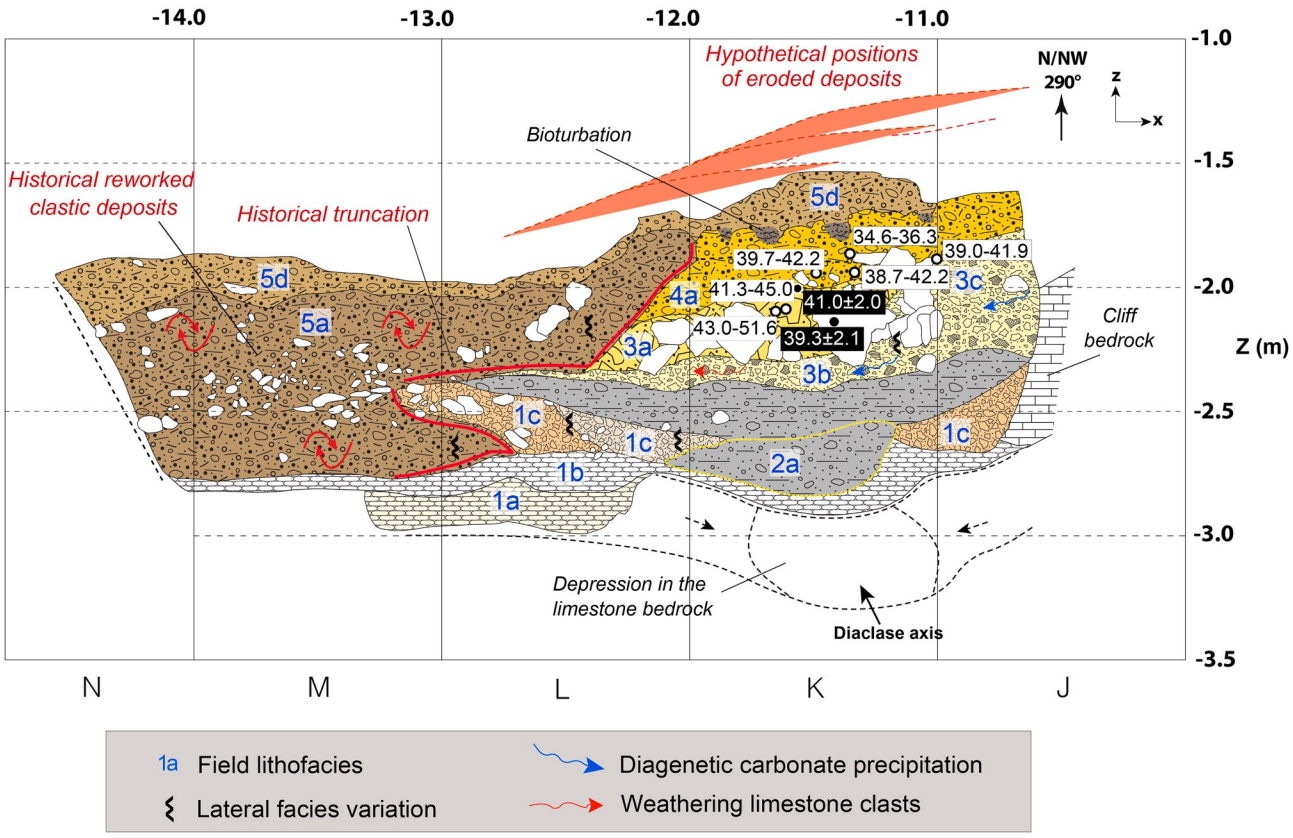

Fig. 7. Illustration of the lithostratigraphic units and subunits observed in the JKLM frontal section, with OSL (black dots) and 2 sigma calibrated ^{14}C (white dots) dates (*cf.* Fig. S14 for facies descriptions).

The remaining mushroom farm samples are clearly distinct from the intra-site and extra-site limestone quarry samples, among which the glauconite sand stands out.

A spectrometric analysis can help to discriminate among the sets and subsets revealed through XRD analysis. The principal component analysis of the ICP-OES data (Table S6) also indicates an opposition between intra-site and extra-site samples, with SiO_2, CaO and LOI as the main discriminating variables for PC1, and Al_2O_3 and total Fe_2O_3 as secondary variables (Fig. 9B). In PC2, Al_2O_3 (negative loading), SiO_2, and CaO (positive loadings) emerge as the most discriminant variables. Among the intra-site samples, a separation can be seen between the sediments derived from the Turonian limestone bedrock (samples G-14 and G-15) and those from the frontal section, associated with historical anthroturbation (samples G-23 and G-24), which plot towards the SiO_2 pole. Along the axis of this variable are the present-day Coran River sands (G-11; not analysed through XRD) and the glauconitic sands (G-6) from the limestone quarry (Fig. S7), individualized from the rest of the samples in the same context. Once again, the square J100 samples in the mushroom farm fall at both sides of the site's sample cluster. Sample G-34 (Facies Q1b) with its high calcitic content marks the transition with the weathered limestone wall and is thus close to the intra-site sediments derived from the Turonian bedrock. Among the extra-site quarry or mushroom farm samples, only sample G-9 is close to the intra-site cluster. Note that the quarry sample clusters partially overlap here.

A principal component analysis of the 10 trace elements showing the greatest inter-sample variability (Ba, Ce, Cr, Nb, Ni, Rb, Sr, V, Zn, and Zr; Table S7), also shows an opposition between intra- and extra-site samples, with Zr, Nb, and V being the most discriminating trace elements in PC1, and Cr, Rb, V, Zn, Ba (positive loadings), and Zr and Nb (negative loadings) standing out in PC2 (Fig. 9C). The cluster of the alterites from the limestone quarry is associated with an elongated distribution, in opposition to the glauconitic sands (G-6), which neighbour the Coran sands (G-11) and sample G-34 (Facies Q1b) from the mushroom farm adjacent to the JKLM zone. Among the intra-site samples, an opposition is seen between sediments derived from the Turonian limestone bedrock (G-14 and G-15) and the other samples. Finally, coupling the XRD data with most variable trace elements does not affect the geochemical discrimination clusters.

3.4. Microstratigraphy

3.4.1. The base of the deposit: Unit 1

Under the microscope, the dome-shaped, pale gray sandy deposit overlying bedrock at the base of the stratigraphic sequence is exclusively composed of unsorted, loose, variably clast- or matrix-supported *in situ* disaggregated Turonian limestone (Fig. S15). The limestone in these samples (a bedrock sample from the rock shelter's back wall, and offsite reference Turonian limestone samples) is similarly composed of a range of microsparitic mollusk pseudomorphs (Fig. 10A and B, C) and nodules (Fig. 10E and F) in a micritic cement. The sandy matrix is loose and crumbly in Facies 1a and locally cemented by micrite in Facies 1b. Some clasts have massive micritic coatings or cappings (Fig. 10A and B, E) containing very few, fine and medium sand-sized, subrounded quartz grains (Fig. 10D–F), comparable to those found in the Coniacian quartz and glauconite sand beds sampled offsite in the limestone quarry. The porosity of the more compact, matrix-rich areas is vughy or vesicular, and there are also a few parallel horizontal planes forming weakly developed lenticular microstructures. No microscopic flint and only rare, sand-sized, subrounded bone fragments were observed (Fig. 10B, Fig. S15, and Table S8 for a high-resolution scan of sample M-11-3, which contains two brown-coloured bone fragments).

3.4.2. The archaeology-rich gray deposit: Unit 2

Micromorphology samples from this unit are from the higher,

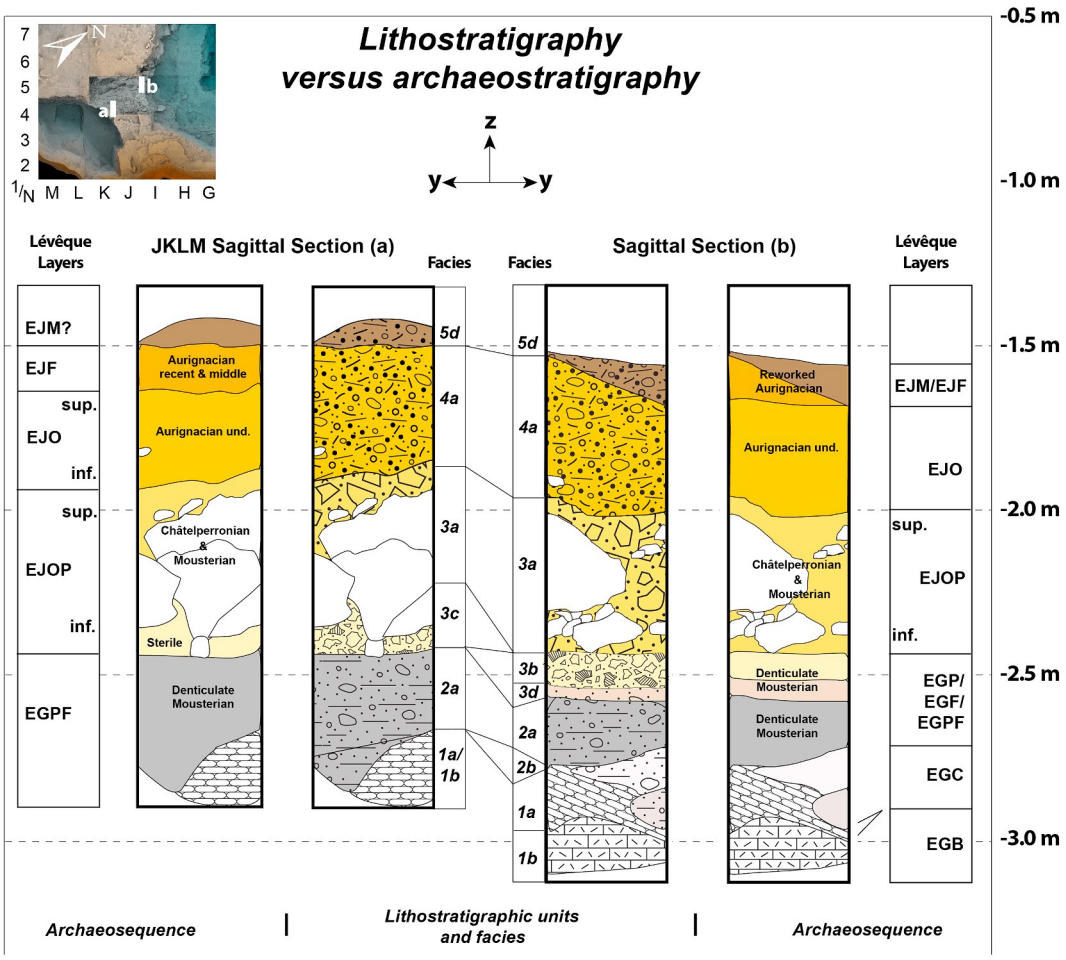

Fig. 8. Stratigraphic logs from the proximal area of the site illustrating lithostratigraphic and archaeostratigraphic correlations between the JKLM sagittal section (J4 III section "a") and Lévêque's main sagittal section (J5 IV section "b").

southeastern zone (M-20, M-23, M-24, and M-15) and from the lower, northwestern zone (M-2). The basic lithological composition of this unit is the same as in the underlying Unit 1 (Fig. 11). Facies 2b contains abundant, unsorted, subrounded, detritic Turonian limestone clasts and few detritic quartz sand-sized grains in a loose matrix made up of micritic calcite. Facies 2a contains higher proportions of quartz sand (Fig. 11) and the matrix is more compact, incorporating clay. The clayey matrix is interrupted by small vughs and a few vesicles and chambers. Facies 2a also contains detritic, exogenous rock fragments, frequent, angular flint flakes, and macro- and micro-faunal bone fragments (see high-resolution scans, Table S8). These objects are densely packed and horizontally bedded (M-20) or dip strongly towards the NW (M-15). Downslope (M-2) the objects are more dispersed and show apparent random orientations. Bone fragments throughout the unit exhibit bioerosion features (Brönnimann et al., 2018) and iron oxide staining, some of which are burned and broken *in situ* (Fig. 11D). Few possible microscopic char fragments derived from animal fat (Lambrecht et al., 2021) were observed (Fig. 11E). Towards the top of Unit 2 there is considerable geogenic input, with an increase of quartz-rich clay in the matrix (Fig. 12B, Fig. S15 and see the upper part of the high-resolution scan of sample M-20-1 in Table S8), as well as possible rotational structures (Fox and Protz, 1981; Menzies, 2000; Menzies and Meer, 2018; Menzies et al., 2019) (Fig. 12A).

3.4.3. *The brownish yellow-yellowish brown diamictons: Units 3 and 4*

All the samples from Units 3 and 4 exhibit similar microscopic sedimentary components and microstructures. Overall, the coarse fraction comprises abundant, well-sorted, weathered, subrounded Turonian limestone lithoclasts (pebbles), frequent quartz sand, and few subrounded iron-stained flint fragments (Fig. 12C). Better sorted limestone clasts and the higher frequency of quartz sand stands out in comparison to the underlying deposit. The matrix is relatively compact and clayier, showing porostriation and granostriation (Fig. 12D), as well as frequent vughs and few vesicles and chambers. Rare randomly oriented micro-fissures were also observed. In contrast with the underlying deposit, the clayey matrix in Units 3 and 4 is pedal (moderately developed subangular blocky peds) and shows common bioturbation features, including channels and calcitic root hypocoatings (Fig. 12D). Microfaunal bone remains are common and archaeological remains are scarce and subangular. Some bone fragments exhibit bioerosion and iron staining, as in the underlying units. Further micromorphological characterization of the Units 3 and 4 field facies is as follows (see Fig. S15 for further details):

- *Basal brownish yellow-yellowish brown diamicton (Facies 3a).* All the samples exhibit the general features described above, although unlike the overlying units, they show a prevalence of unsorted coarse lithoclasts (pebbles). Macrofaunal bone fragments and flint flakes (which are subangular throughout Units 3 and 4) are rare in this facies and more common towards the top, which contrasts with the abundance of microfaunal bone fragments. The samples from the JKLM area show a lithological difference from the other facies, as the lithoclasts are often angular.

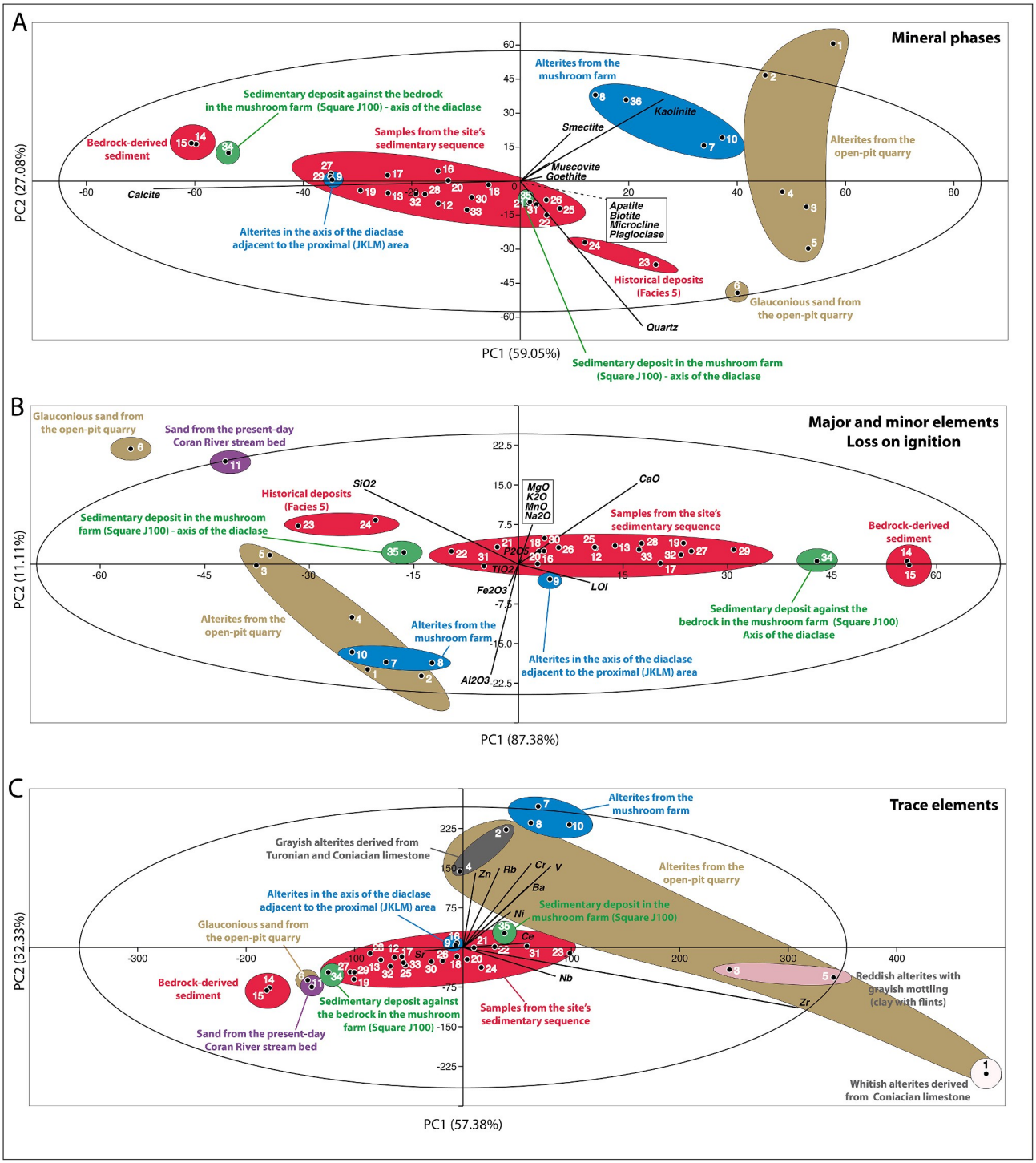

Fig. 9. A: PCA biplot (variance-covariance matrix) of mineral phases identified through XRD analysis. Sample No. 11 from the Coran River was not analysed (modern stream bed medium sand). B: PCA biplot (variance-covariance matrix) of the 10 major and minor elements (SiO_2, Al_2O_3, total Fe_2O_3, MnO, MgO, CaO, Na_2O, K_2O, P_2O_5, TiO_2) identified and loss on ignition (LOI) values. Sample No. 36 from the mushroom farm was not analysed (alterites). C: PCA biplot (variance-covariance matrix) of the 10 most variable trace elements (Ba, Cr, Nb, Ni, Rb, Sr, V, Zn, Zr, Ce). Alterites sampled from the limestone quarry are discriminated according to their geochemical signature. Sample No. 36 from the mushroom farm was not analysed (alterites). Ellipse = 95% of the variance, assuming a bivariate normal distribution.

- *Whitish, calcitic, silty-sandy layer on the sagittal section (Facies 3b).* This layer is composed of *in situ* disaggregated limestone (see high-resolution scans of M-15-1 in Table S8).
- *Loose sandy clay lens underlying 3b on the sagittal section (Facies 3d).* This lens was observed in sample M-15b. It is composed of quartz-rich clay.
- *Brownish yellow-yellowish brown pebbly diamicton (Facies 4a and 4b).* These samples show higher proportions of quartz sand and smaller-sized pebbles than the underlying deposit, and coarse lithorelics (pebbles and cobbles) are less frequent. The clayey matrix shows a more pronounced b-fabric (porostriated, granostriated and locally stipple-speckled). Microfaunal bone fragments are mostly present at

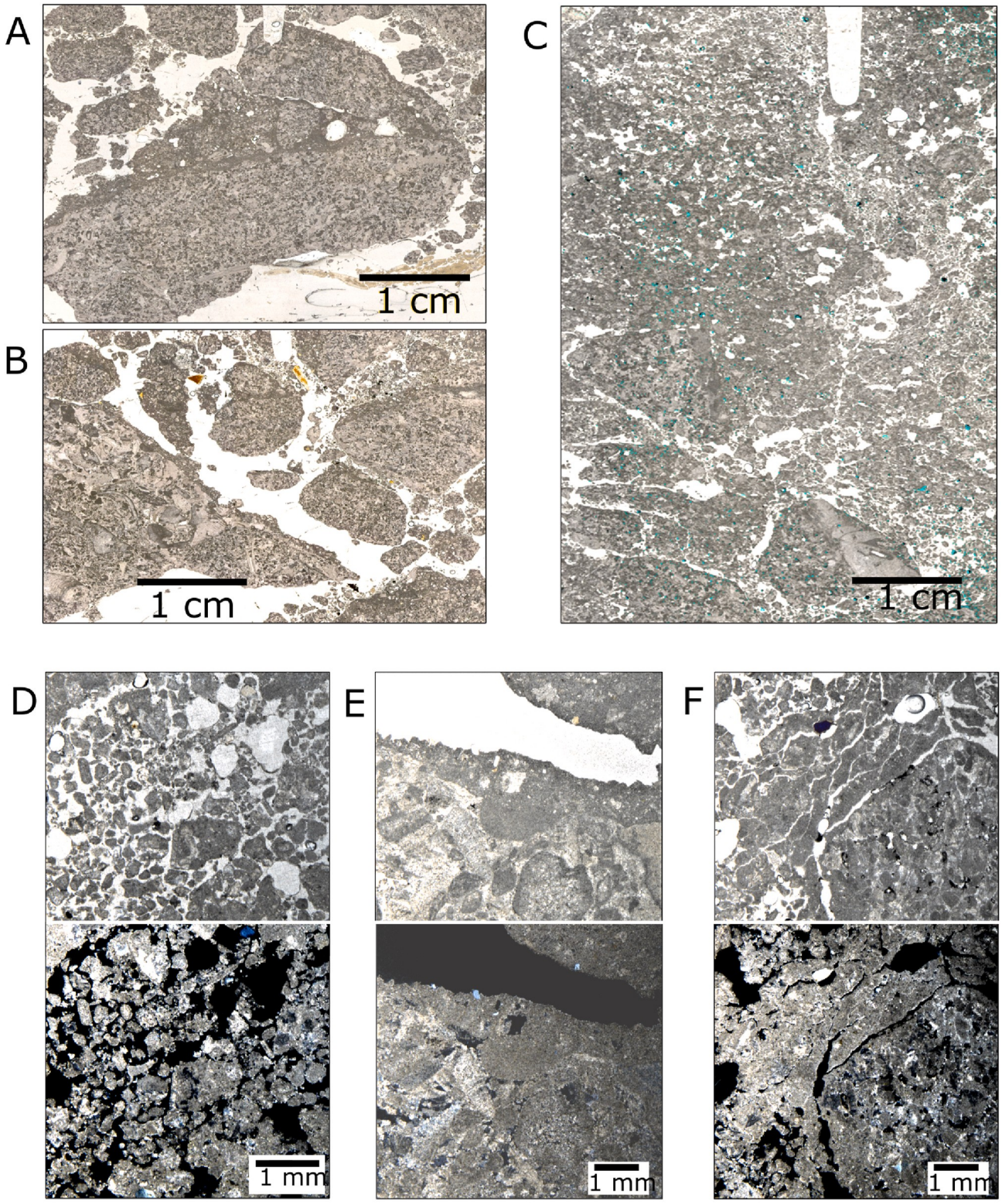

Fig. 10. A selection of Unit 1 microphotographs showing representative micromorphological features. This unit is composed of loose sediment comprising disaggregated Turonian limestone and sparse detrital quartz sand. There are locally cemented, matrix-rich areas. The limestone is micritic and fossiliferous, and exhibits good preservation states. Cryoturbation is evidenced as micritic cappings (A, B and E) and as localized zones exhibiting parallel horizontal planes forming weakly developed lenticular microstructures (base of C and the capping in F). Note the scarcity of flint, bone (two very small, orange-brown fragments visible in B), and quartz, which is present as low amounts of detrital grains (visible as small, isolated blue grains in the crossed-polarized views of D and E, and a single larger, bright white grain in F).

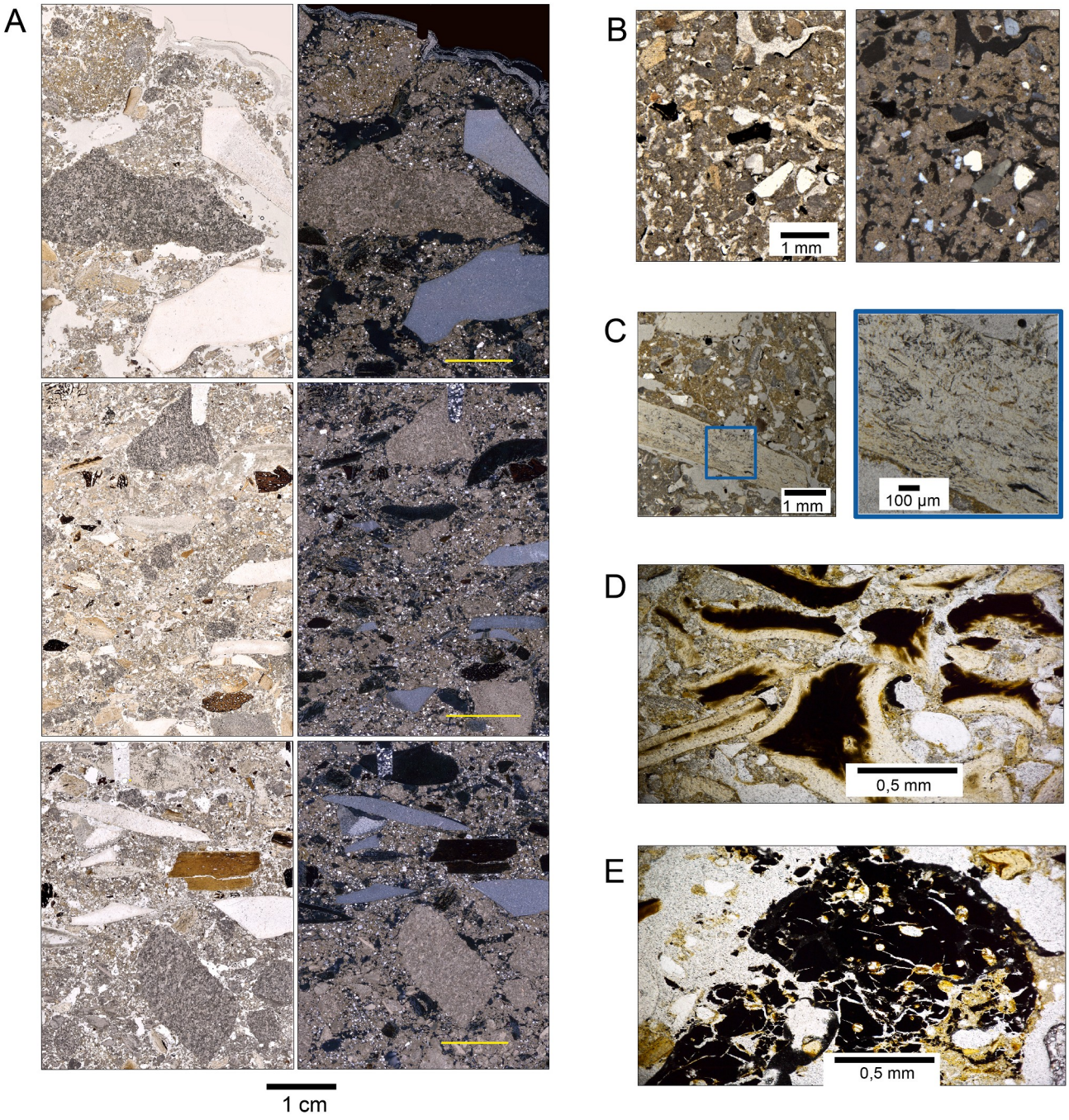

Fig. 11. Selected scan views in plane and crossed-polarized light (A) and photomicrographs (B–E) of Unit 2 thin sections. These sediments contain frequent, unsorted, subrounded limestone clasts in a matrix that is micritic at the base (A-left, bottom thin section) and clayier towards the top (A-left, middle and top thin sections; note the brown colour of the matrix). There are few to common detritic quartz sand grains (A-right side) and frequent, horizontally bedded angular flint flakes and macro- and micro-faunal bone fragments (A). The clayey matrix is pierced by small vughs (B). Bone fragments throughout the unit exhibit iron oxide staining and bioerosion features (C) and some of them are burned and broken *in situ* (D). There are also a few possibly animal-derived char fragments (E).

the base, while flint flakes (scarce and subangular) are concentrated towards the top.

3.4.4. The bioturbated, anthropoturbated diamictons: Unit 5

The samples from Unit 5 show a lithological composition similar to that of the underlying deposit, with variable proportions and variable degrees of sorting of the limestone clasts and quartz sand in the different subunits (Fig. S15). The matrix is also clayey, decalcified, and is more strongly bioturbated and shows a well-developed pedality. There is abundant dispersed organic silt. Very few subangular lithic flakes were observed, along with a single charcoal fragment (in Facies 5b) and no bone. Subrounded ferruginous flint fragments are few.

3.4.5. The sedimentary infill in the mushroom farm behind the site: Unit Q1

The sample from this infill shows a massive clayey matrix with abundant small vughs and few detritic components: subrounded Turonian limestone lithoclasts (pebbles), quartz sand and few predominantly angular and subangular bone fragments. The top part of the sample shows oblique microstrata of alternating coarse sandy and fine clayey lenses. This sequence includes crusting microfeatures. No granostriation or porostriation was observed. There are a few partially filled subrecent root channels.

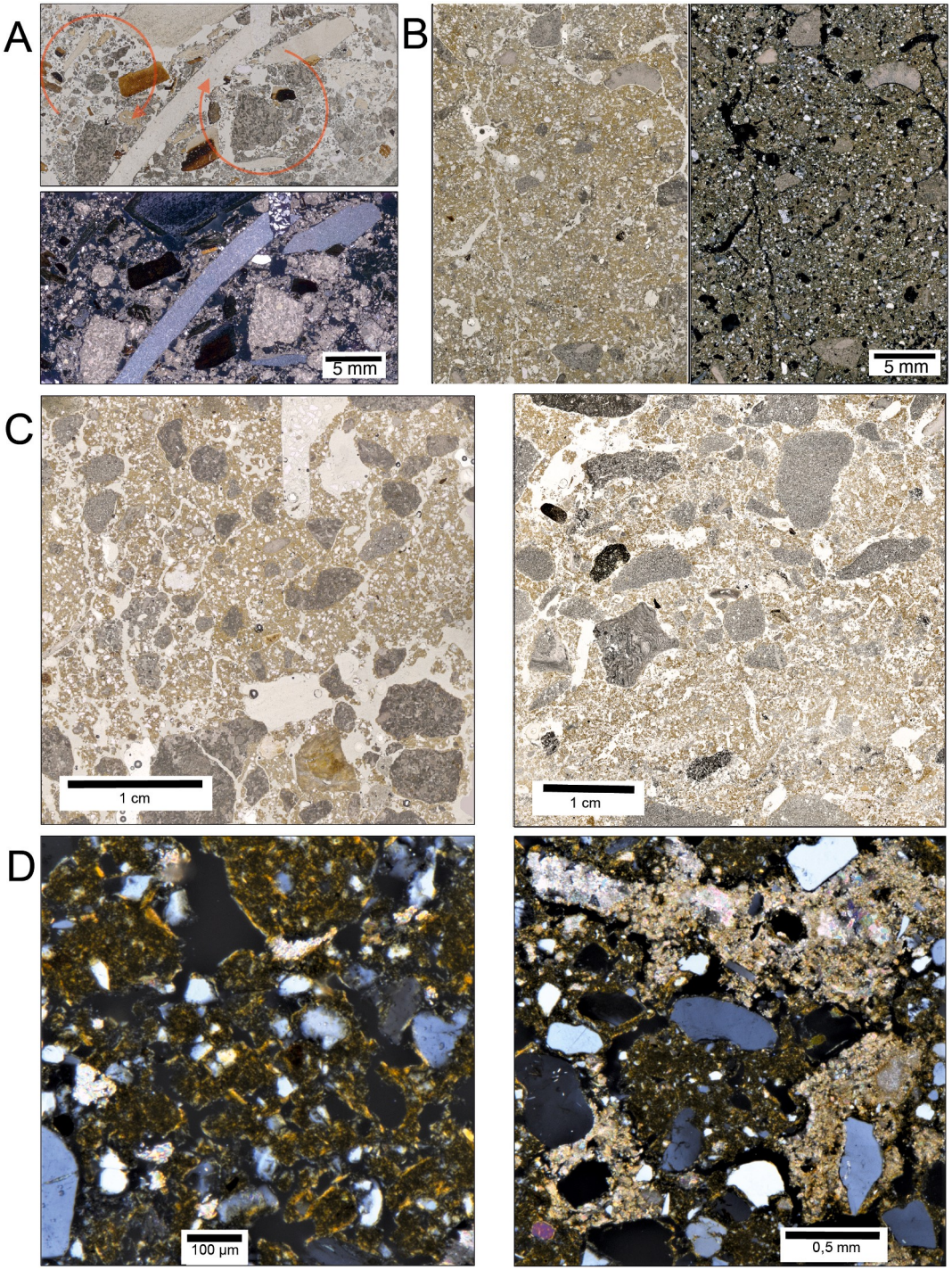

Fig. 12. A and B: Thin section scans of sediments from the top of Unit 2 (lower part of A in crossed-polarized light). Note the presence of rotational features (A, on the left, coarse elements are arranged radially around fine ones, and in the right, the opposite configuration is seen) and common quartz sand (B). C and D: Thin section scans showing sediments from Units 3 and 4, which are similarly composed of common, well-sorted, weathered, subangular to subrounded limestone lithoclasts (pebbles), common to frequent quartz sand, a few subrounded ferruginous flint fragments (C, subrounded darker grains), and rotational features (C, right). The matrix is relatively compact and clayey, showing porostriation and granostriation (D, left, crossed-polarized light), and few calcitic root hypocoatings (D, right, crossed-polarized light).

3.5. *Fabric analysis*

Fig. 13 shows Schmidt diagrams with the density contour intervals, conical best fit, and the Fisher mean vector for three archaeological assemblages. The analysis reveals a micro-spatial variability in the orientation polarities, likely reflecting 1) immaturity of the diamictic deposits (i.e., intrinsic properties of the sediments), 2) influence of local topographical irregularities and buried palaeo-morphologies on the orientation of archaeological remains, and 3) interaction between archaeological and natural objects (e.g., the "blocking" effect) during sedimentary accretion (Bertran et al., 1997; Millar, 2005). Such combined factors suggest that the microenvironment likely influenced the observed patterning in artefact and bone orientations, as in Facies 3a at square J5 (Fig. S12). There is also a possible scalar effect: the fabric

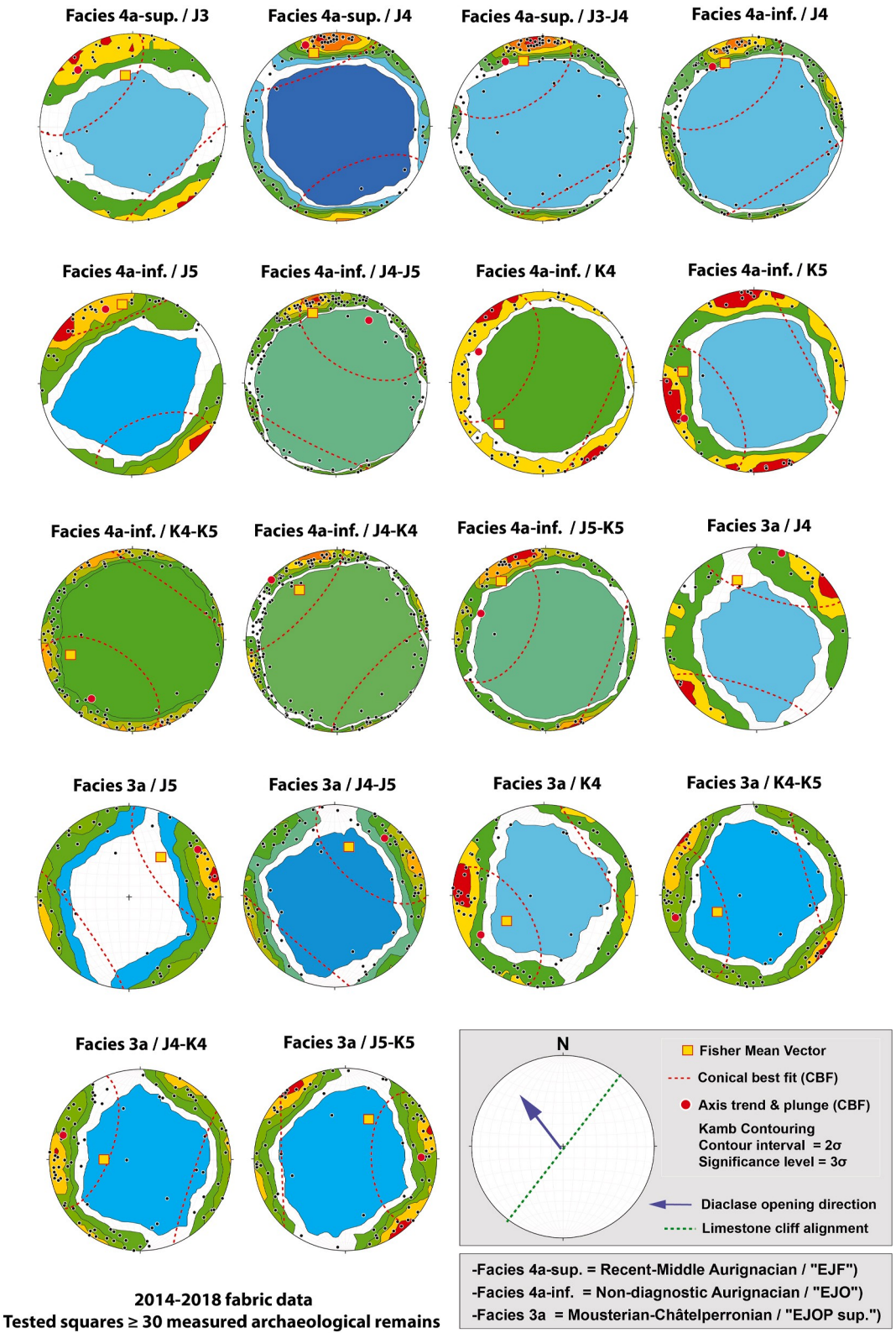

Fig. 13. Stereonet - Schmidt diagrams (lower hemisphere) and density analysis (Kamb method) of the archaeological assemblages (fabric data) from Facies 3a, base of Facies 4a (4a-inf.) and top of Facies 4a (4a-sup.) excavated between 2014 and 2018.

analysis was performed at a macroscopic scale, based on excavated square metres, while the processes reworking archaeological material might have operated at infra-metric scale unrelated to the excavation grid.

Depending on the statistical indicators used, and according to the squares considered and the grouped squares, the orientation polarities show trends toward the N/NW (Facies 4a-sup.; J4, J5, K4, and J4+K4, J5+K5, Facies 4a-inf.), the N/NE (J4+J5, Facies 4a-inf.; J4, J5, J4+J5, Facies 3a), the E (J5+K5, Facies 3a), or the W/SW (K4, K5, Facies 4a-inf. ; K4, K4+K5, J4+K4, Facies 3a). The length of the mean vector (r;

between 0.153 and 0.598), which represents the preferential orientation intensity, is higher as a directional mode is more pronounced (Tables S9, S10 and S11). The concentration parameter (k; between 0.31 and 1.50) and circular dispersion also reflect the greater or lesser heterogeneity of the orientations.

The circular statistical tests used, including those performed on the axial data (with doubled angles), reveal varying fits to the tested distributions (uniform or von Mises; SOM-Section 2.6; Tables S9, S10 and S11). Considering Rayleigh's uniformity test, the latter has a significant p-value (threshold <0.05) for Facies 4a-sup. in J4 and J3+J4 (same result for Rao's spacing test), for all tested squares or groups for Facies 4a-inf. (except K4; same result for Rao's spacing test), and for Facies 3a in K4 and J4+J5. For other squares, the p-value associated with the Rayleigh test is close to the significance threshold (J3 for Facies 4a-sup.; K4 for Facies 4a-inf.; J5 for Facies 3a) or becomes significant with Rao's spacing test (J4 or J5, K4 +K5, J4 +K4 or J5 +K5 for Facies 3a). As shown on Fig. 13, some multimodal distributions can be suggested but the current tests (such as Watson's test, Kuiper's test and Rao's spacing test) may lack statistical power to reveal them (Landler et al., 2018).

On the Benn diagram (Fig. 14), all the plotted squares (Facies 4a-inf.) show a planar fabric or an intermediate fabric between the planar and linear types (Facies 4a-sup., Facies 4a-inf. at square J5, and Facies 3a). Keeping in mind that in some cases fabric may be non-diagnostic and not significantly different from those found in unmodified sites, the observed fabrics may be indicative of combined (whether diachronous or synchronous) depositional processes (slow mass movement such as solifluction and overland flow/slopewash) without excluding some post-depositional bioturbation (e.g., soil fauna, roots).

3.6. ^{14}C dating

Radiocarbon ages were obtained for Units 3, 4 and 5 (Tables S3 and S13). They are displayed in Fig. 15 following their stratigraphic position and facies association (Figs. 4, 5 and 7). While the samples from Units 4 and 5 had good collagen yields, only two out of 20 samples from Unit 3a (samples C-9 and C-10) were just above the minimum threshold for dating. The distribution of ages, particularly in the upper part of the sequence (Units 4 and 5), are in good agreement while those from the lower portion display wider confidence intervals (Facies 3a and 3a/4a). The sample from the mushroom farm (C-12; Fig. S6 and Table S13) aligns well with those of basal Facies 4a. In the JKLM area, sample C-6 from the same unit returned a much younger age. However, it fits the stratigraphic order and is consistent with the OSL ages for the two underlying sediment samples (O-14 and O-15) at 2 sigma. The fact that this sample was collected close to a bioturbated zone might explain this young age (Fig. 7). Some archaeological remains may derive from a transitional facies seen during fieldwork. Locally affected by root bioturbation, the integrity of this facies cannot be assured in specific locations (e.g., contact Unit 4/Unit 5), with the possibility of organic contamination or younger remains incorporated from the subsurface.

3.7. OSL dating

Luminescence ages were obtained for 16 samples from Units 2–5. The OSL results are displayed in Figs. 4, 5 and 7 and in Table 1 (see also SOM-Section 2.8; Tables S16 and S17). The OSL ages are stratigraphically consistent and generally agree with the radiocarbon ages. Below, we summarize the OSL data by stratigraphic unit, from base to top:

- Unit 2: Collected in the main sagittal section, OSL sample O-6 (SG, Facies 2b) yielded an age of 50.6±3.9 ka, whereas sample O-4 (SG, collected from the top of Facies 2a) gave an age of 45.5± 2.6 ka. Downslope, two samples collected at the base of the main frontal

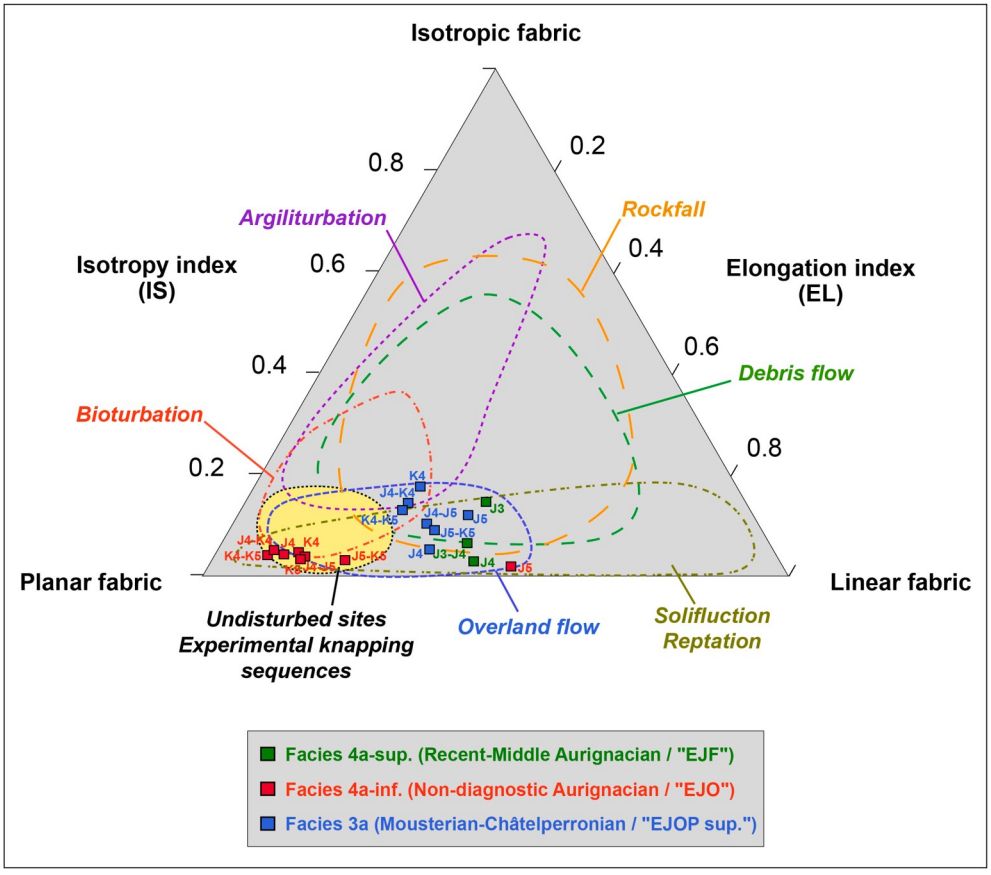

Fig. 14. Benn diagram of the archaeological assemblages from Facies 3a, base of Facies 4a (4a-inf.) and top of Facies 4a (4a-sup.) separated by squares or groups of squares. Fabric data from the 2014–2018 excavations. Tested squares ≥30 measured archaeological remains. Contours follow the guidelines reported by Lenoble and Bertran (2004) and Lenoble and Agsous (2013). Poles of fabric types: 1) isotropic (unsorted objects and multiple orientations), 2) planar (objects positioned on a plane, with multiple orientations), and 3) linear (objects show a preferred orientation and plane distribution). Note that the tested squares from Facies 4a-inf., except J5 square, are closer to the planar pole than the squares from Facies 4a-sup. or Facies 3a.

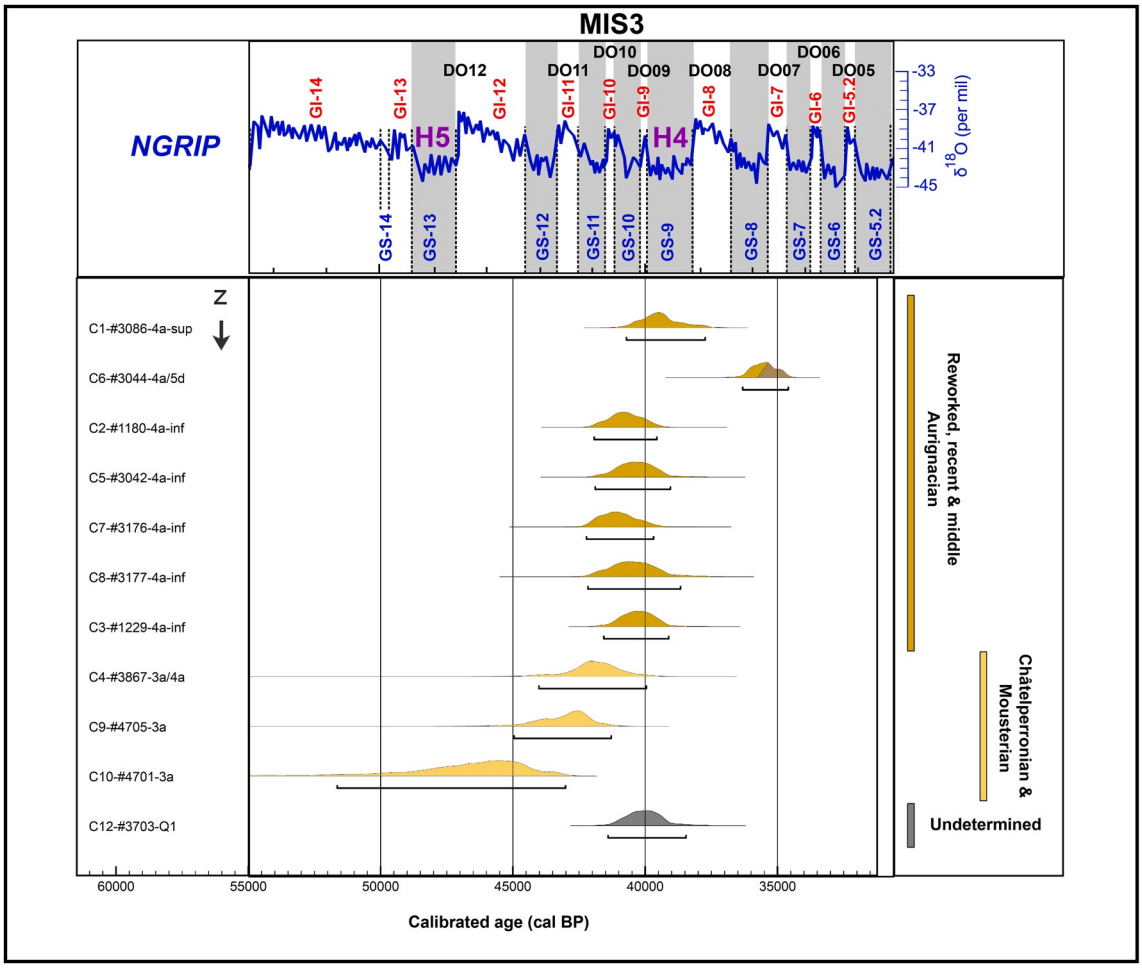

Fig. 15. Calibrated plots of the radiocarbon dates obtained on bone collagen from faunal remains in Units 3, 4 and Q1. Calibration at 2 sigma (95.4%) with the IntCal 20 curve (Reimer et al., 2020) using Oxcal program version 4.4 (Bronk Ramsey, 2021). Colours refer to the associated lithostratigraphic units (*cf.* Fig. S14). North Greenland Ice Core Project (NGRIP) curve modified after Waters et al. (2022). NGRIP numbers represent Greenland Stadials (GS) and Greenland Interstadials (GI). Heinrich events (H) coincide with cold phases of Dansgaard–Oeschger events (DO).

Table 1
OSL dating results on fine and coarse-grain samples. MG = Multi-grain; SG = Single-grain; De = Equivalent dose; ADM = Average Dose Model; FMM = Finite Mixture Model.

ID	Sample	Associated Facies	Method	Grain fraction (μm)	n	De (Gy) ADM	σ_d ADM (%)	Age (ADM) (ka)
–	SC14-02	Bedrock	*Not dated*	20–41	–	–	–	–
–	SC14-04	Bedrock	*Not dated*	20–41		–	–	–
O-1	SC15-05	Facies 3f	SG	180–250	223	59.9 ± 1.9	21 ± 4	45.5 ± 3.0
O-2	SC15-07	Facies 5b	MG	180–250	4	3.05 ± 0.65	39 ± 13	2.6 ± 0.6
O-3	SC15-06	Facies 4c	SG	180–250	214	67.8 ± 2.2	27 ± 3	40.5 ± 2.8
O-4	SC17-02	Facies 2a	SG	180–250	214	45.5 ± 1.4	32 ± 4	45.5 ± 2.6
O-5	SC17-03	Facies 3a	SG	180–250	205 (FMM)	41.8 ± 0.6 (82.5%)	- (FMM)	40.6 ± 2.0
O-6	SC17-01	Facies 2b	SG	180–250	213	84.4 ± 3.2 (17.5%)	30 3	50.6 3.9
O-7	SC14-10	Facies 2b	MG	20–41	26	38.8 ± 1.17	±	59.2 ± 3.9
O-8	SC14-08	Facies 2b/3f	MG	20–41	28	41.45 ± 0.89 43.26 ± 0.91	0 ± 0 0 ± 0	50.5 ± 3.1
O-9	SC14-06	Facies 3f	MG	20–41	24	66.34 ± 1.49	0 ± 0	52.5 ± 3.8
O-10	SC15-01	Facies 2b	SG	180–250	218	50.1 ± 1.6	20 ± 5	59.9 ± 4.3
O-11	SC15-04	Facies 5c	MG	180–250	5	0.62 ± 0.02	0 ± 0	0.8 ± 0.1
O-12	SC15-03	Facies 5b	MG	180–250	24	4.51 ± 0.37	35 ± 5	3.2 ± 0.3
O-13	SC15-02	Facies 3f	SG	180–250	184	52.9 ± 1.7	27 ± 5	53.8 ± 3.4
O-14	SC17-04	Facies 3a	SG	180–250	443	54.8 ± 0.9	26 ± 2	41.0 ± 2.0
O-15	SC19-01	Facies 3a/3b	SG	200–250	137	57.1 ± 1.4	23 ± 2	39.3 ± 2.1
O-16	SC19-02	Facies Q1a	SG	200–250	177	63.0 ± 2.1	31 ± 3	40.1 ± 2.4

section produced an age of 59.9 ± 4.3 ka (O-10, SG) and 59.2 ± 3.9 ka (O-7, MG). A sample from higher up in the unit returned an age of 50.5 ± 3.1 ka (O-8, MG). Samples from the frontal section correspond to the facies 2b or interfacies 2b–3f.

- Unit 3: An OSL sample from Facies 3a on the JKLM frontal section (O-15, SG, but no dosimeter) yielded an age of 39.3 ± 2.1 ka. A sample from the same facies and from the same area of the palaeotalus in the main sagittal section (O-5, SG) gave an age of 40.6 ± 2.0 ka (Table S17) using the Finite Mixture Model (FMM; Roberts et al., 2000). Among all the measured samples, this sample was the only one giving an inconsistent age when calculated using the Average Dose Model (ADM; Guérin et al., 2017) and when compared to other OSL and radiocarbon ages. Considering that the FMM dose cannot be matched with a reliable value (Guérin et al., 2017), we regard this age as preliminary and not fully reliable. Downslope in the frontal section, samples O-13 (SG) and O-9 (MG) from Facies 3f yielded ages of 53.8 3.4 ka and 52.5 3.8 ka, respectively. Regarding the multigrain ages, limited information can be deduced from the apparent extrinsic overdispersion of grains.
- Unit 4: An OSL sample from Facies 4a in the JKLM frontal section (O-14, SG) yielded an age of 41.0±2.0 ka. In the main sagittal section, a sample from farther downslope in Facies 4c (O-3, SG) gave an age of 40.5 ± 2.8 ka.
- Unit 5: The samples for this unit were collected downslope. In Facies 5b, samples in the main sagittal (O-2, MG) and Frontal (O-12, MG) sections produced ages of 2.6± 0.6 and 3.2 ± 0.3 years, respectively. A sample collected in the same section from higher up in Facies 5c (O-11, MG) is associated with an age of 800 ±100 years.
- Unit Q1: At the mushroom farm (Fig. S6), sample O-16 (SG, no dosimeter) from the fauna-containing sediment yielded an age of 40.1 ± 2.4 ka.

4. Discussion

4.1. Geomorphological considerations

Field observations shed some light on the geological evolution of the Turonian cliff adjacent to the La Roche-à-Pierrot deposit. Geomorphological observations indicate that the Turonian limestone at the site underwent ghost-rock karstification (Dubois et al., 2014, 2022), as well as substantial dissolution. Local karstic evolution is likely related to the incision of the Coran (Fig. 1), a process possibly repeated at other points along the Turonian cliff, including the mushroom farm behind the site (6 m above the current Coran alluvial plain), as suggested by incipient karstic features such as a small channelled restitution drain upstream from the site. The undulating parallel Liesegang bands identified in the the limestone historical quarry (Fig. S8) are possibly related to the precipitation of iron oxides and hydroxides from saturated water during fluctuations in the epi-phreatic water table. The features observed on the younger Coniacian limestone in the open-pit quarry are potentially also related to the same incipient karstic system. Taken together, the evidence of a well-established karstic system directly behind the cliff face next to the site supports the existence of a former karstic chimney or solution pipe that progressively collapsed and disappeared during the Late Pleistocene (Figs. 16 and 17).

4.2. Geogenic sources of sedimentation and their chronology

Our multiproxy analyses form the basis for a site formation model for the La Roche-à-Pierrot archaeo-sedimentary sequence (Figs. 16 and 17). In terms of the geogenic sources of the deposits, our data indicate a multidirectional redistribution and accumulation of autochthonous to parautochthonous/allochthonous detrital sediments with a dome-shaped morphology at the foot of the limestone cliff. These results are consistent with the spatial distribution of archaeological remains recovered and recorded during Lévêque's excavations, as revealed by

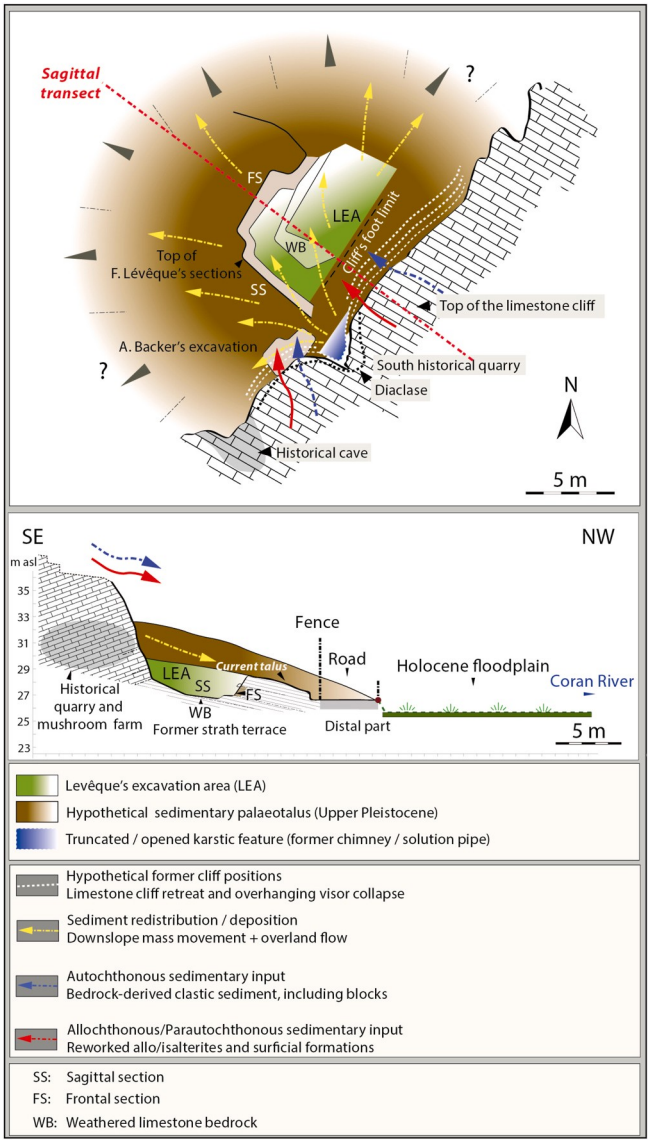

Fig. 16. Dynamic model of the geomorphological evolution of the La Roche- à-Pierrot deposit.

the density, Z-mean projections and hot spot analysis of the Z values of faunal and lithic remains (SOM-Section 2.9; Fig. S19), and by the longitudinal projections of faunal and lithic objects (Morin, 2012; Gravina et al., 2018).

The composition of the sediment reflects the local diversity of surficial formations, especially the alterites, as well as endokarst isalterites, present in the vicinity of the site (Figs. 2 and 9). The coarse lithological fraction is dominated by Turonian limestone with very minor input of Lower Coniacian quartz sand, the clayey fraction being kaolinite and smectite. At the base of the sequence, a disaggregated bedrock-derived sediment with lenticular microstructures and coated and capped platy limestone clasts (Unit 1) points to the existence of frost action with intense cryoclasty or frost shattering (Van Vliet-Lanoë et al., 1984; Van Vliet-Lanoë, 1987, 1998) of the Turonian bedrock, which had previously been carved into a strath terrace by the palaeo-Coran. At this time, human occupations occurred in what was potentially a semi-enclosed, disintegrating (endo)karstic space that received no significant exogenous sedimentary input (Fig. 17). The occasional presence of small-sized faunal remains in Unit 1 indicates the presence of minor openings allowing occasional infiltrations. While this deposit remains undated, a minimum age of *ca.* 60 ka (MIS4) is possible given the oldest date

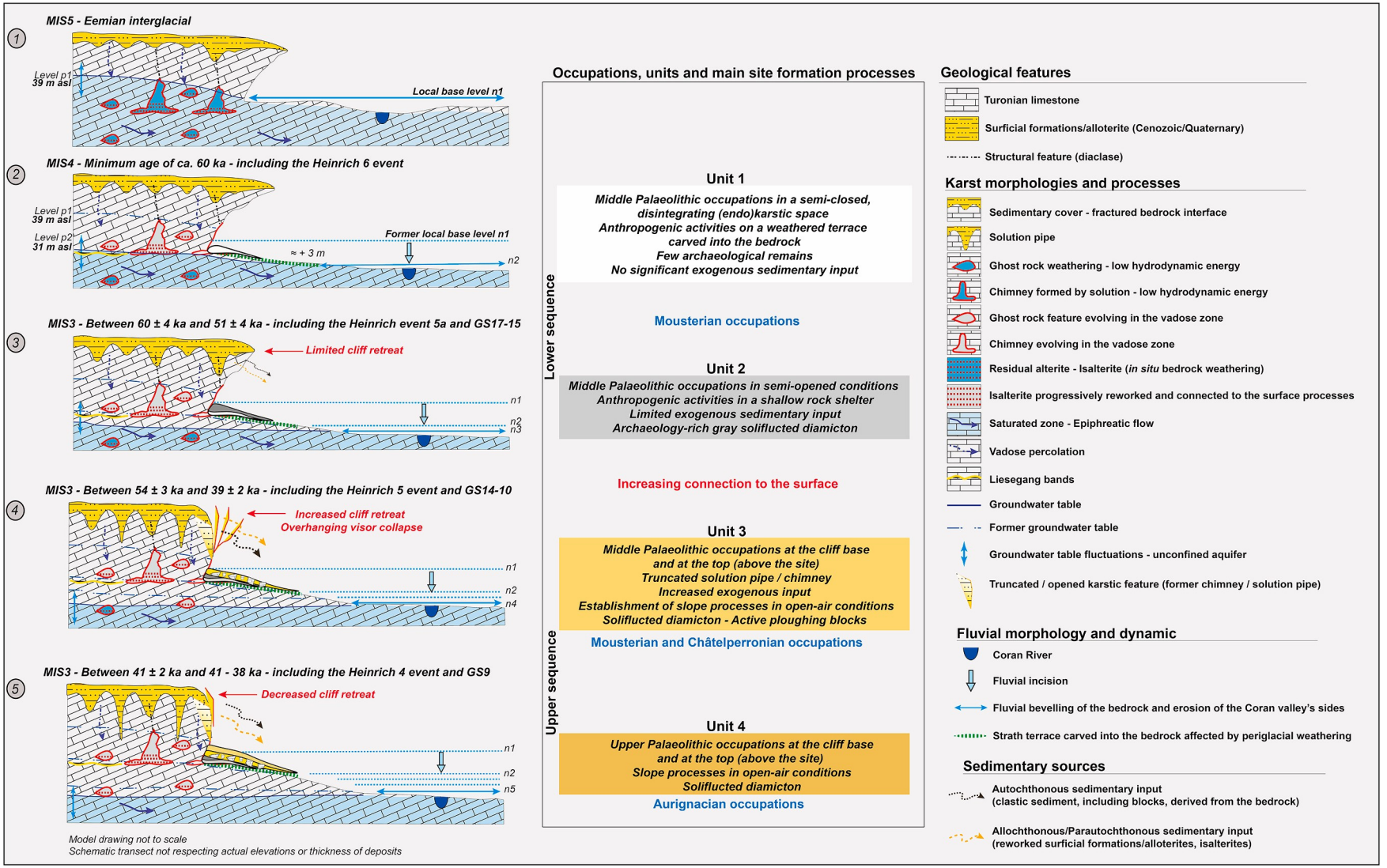

Fig. 17. Diachronic model for the geomorphological evolution of La Roche-à-Pierrot showing geological, karstic and fluvial features, sources of sedimentation as well as human occupations. Five main phases are shown based on field observations and geochronology (radiocarbon and OSL ages). Positions of the Heinrich events and Greenland Stadials (GS) are proposed.

obtained for Unit 2.

This basal sediment directly underlies the archaeology-rich gray deposit (Unit 2, Late Mousterian), which comprises sediments composed predominantly of local angular limestone cryoclasts with exogenous and detrital input, Lower Coniacian quartz sand and kaolinite clay. We interpret this deposit to represent a more open depositional context with increasing (but limited) exogenous input from fissures, connected to the surface, as a result of the progressive disintegration/dissolution of the limestone structure. The main opening of a karstic feature (truncated chimney/solution pipe; Fig. 17) was possibly associated with cliff retreat and the evolution of the diaclase immediately adjoining the JKLM area (Fig. 16). In agreement with the radiocarbon date available for Unit 2 (42.5–52.2 ka cal BP for Mousterian level EGPF) from a previous study (Higham et al., 2014), the three OSL ages obtained for the basal part of this unit (samples O-6, O-7 and O-10) suggest an age ranging between 59.9 ± 4.3 ka and 50.6 ± 3.9 ka (the single-grain ages, O-6 and O-10, are consistent with these estimates). Regarding sample O-4 (45.5 ± 2.6 ka, Facies 2a, sagittal section), we cannot exclude the possibility that quartz grains come from the erosion of the upstream deposits (from JKLM zone) and/or from the retreating karstified cliff, as compared to the progressive sedimentary accretion further downstream (frontal section). Taking into account the standard deviations of the OSL dates (especially O-6, 50.6 ± 3.9 ka), the end of this phase would be around 51 ± 4 ka.

The major roof collapse identified at the top of Unit 2 led to a retreat of the Turonian cliff and opening of the local karstic diaclase, establishing a sedimentary connection between the summit slopes (above the site) and the footslope, with the formation of a talus from cryoclastic debris and downslope mass wasting as a dominant geomorphological process (Figs. 16 and 17). There is an increasing proportion of clay in the sediment towards the top of Unit 2. This textural change is associated with mass movement, as indicated by: 1) the preferred orientations of the pebbles, cobbles, boulders and archaeological remains on the main sagittal and frontal sections; 2) the presence of ploughing blocks, strongly-dipping metre-sized boulders oriented parallel to the slope (Washburn, 1973; Ballantyne and Harris, 1994; French, 2017); 3) microscopic sedimentary shear (evidenced by granostriation) and rotational features (Harris, 1998); and 4) water saturation and pore pressure as evidenced by vesicles and chambers at microscale (Van Vliet-Lanoë and Fox, 2018).

The presence of boulders and a lens of massive sand (Facies 3d) at the interface between Units 2 and 3, and the presence of reworked Unit 2 sediment at the front faces of some of the boulders towards the base of Unit 3 (Facies 3e) places the first major roof collapse event at the transition between these two units and implies some degree of truncation and erosion of the top of Unit 2 (Fig. 4). The upper part of the sedimentary sequence (Units 3, 4 and 5) comprises a stratified slope deposit: a succession of diamictic layers with higher amounts of exogenous clay and quartz sand, iron-stained flint fragments from the geological outcrops above the site and weathered, sorted, and limestone clasts in variable proportions (Figs. S11 and S14). These features indicate progressively more exogenous local sedimentary input at the site and the implementation of open-air slope dynamics. The presence of limestone boulders in different areas within Units 3 and 4 suggests the structural collapse of the former overhang (Fig. 17). Considering the macroscopic sedimentary structure of these diamictic layers, which dip strongly away from the JKLM area and show subtle erosional contacts and changes in slope gradients (for example in square J5; Fig. S11), we suggest the action of periglacial processes. Solifluction features likely included small-sized lobes and thin sheets, fed by exogenous sediments originally deposited in the JKLM area which moved downslope to form a talus (Fig. 16).

The local geomorphological context, together with the overall similarity between Units 3 and 4, representing at least two main successive (diachronic) solifluction phases, suggest that they are not genetically related to debris flow processes (Coussot and Meunier, 1996; Mücher et al., 2018). This is further suggested by the crude stratification of these units, their bedding and the presence of blocking elements, buried lobate morphologies (Fig. S12) and absence of channel structures. Reworking of sediments and archaeological remains by slow downslope mass movement in Unit 3 is also suggested by the spatial distribution of remains from Lévêque's excavations (level EJOP), in which possible solifluction features are visible (Backer, 1993; Fig. S13). These observations are also in agreement with recent vertical and horizontal distributions and projections of piece-plotted artefacts from this unit (Morin et al., 2005; Gravina et al., 2018) and our own fabric analysis data (Fig. 13).

The presence of solifluction features in Unit 3 is consistent with several microscopic sedimentary features, including: 1) the angular shape of lithoclasts (pebble and cobble fractions) in the JKLM area, 2) the overall subrounded shapes and well-sorted coarse fraction observed downslope, 3) the porostriation and granostriation of the fine fraction, and 4) a proportionally increasing representation of quartz sand as we move up the sequence in Unit 2. These features indicate slow, incremental mass movement consistent with solifluction (Harris, 1998). At the interface between Units 3 and 4, the apex of the palaeotalus possibly shifted a few metres upslope and increased in thickness, feasibly as a result of sedimentary accretion. This is evidenced by a sharp lithological change in the JKLM area; the Facies 4a sediment contains higher amounts of quartz sand, smaller limestone clasts (smaller pebbles and fewer cobbles) and more pronounced microscopic porostriation and granostriation of the clay fraction than the underlying Facies 3a sediment. This change was observed in the JKLM area and downslope in the sagittal section.

Even though the radiocarbon and OSL ages obtained in this part of the sequence are in good agreement and consistent with previous radiocarbon ages, they do not resolve the timing of the diamictic talus formation described above. Unit 3 could have been formed between 53.8 ± 3.4 ka and 39.3 ± 1 ka considering the maximum age for OSL sample O-13 and the minimum age for OSL sample O-15. The OSL data obtained for the different Unit 3 facies are stratigraphically coherent within uncertainties and support a correlation between Facies 3b, 3c and 3d throughout the different sections. The two radiocarbon ages obtained for Facies 3a (samples C-9 and C-10; Table S13) should be considered as minimum ages due to their low collagen yields. The proposed time frame for Unit 4 is between 41.0 ± 2.0 ka and 40.7–37.7 ka cal BP (OSL samples O-14, top of Unit 3, and C-1 range, respectively; Table S13). The youngest radiocarbon age, C-6 (34.6–36.3 ka cal BP), although compatible with the estimated time range for Unit 4, might be affected by bone preservation issues, post-depositional processes (inducing age rejuvenation), or reworked material from Unit 5d, a mixed sediment postdating the human occupations.

The overall good fit between the radiocarbon date from Unit Q1 (38.5–41.4 ka cal BP) in the mushroom farm and those from Unit 4a in the JKLM area, along with the presence of macroscopic bone and microscopic bone and quartz sand in Unit Q1, point to a former connection between the JKLM area and the karstic cavity immediately behind it. This chronological correlation is consistent with the OSL date obtained for the Unit Q1 deposit (40.1 ± 2.4 ka, sample O-16). Both contexts were possibly part of the same depositional dynamics, fed by pulses of exogenous material that was episodically introduced into the disintegrated rock shelter through progressively larger joints in the limestone bedrock.

Finally, Unit 5, which has a richer organic content and shows more pronounced bioturbation and pedogenic features, yielded very recent (historical) ages, ranging between 3.2 ± 0.3 ka and 1343-1176 cal BP (2 sigma) for Facies 5b (OSL sample O-12 and radiocarbon sample C-11, respectively) and 800 ± 100 years for Facies 5c (OSL sample O-11).

4.3. The sedimentary environment

The general geometry of the sedimentary layers, the presence of ploughing blocks and the fabric data, together with microscopic evidence of frost shattering in Unit 1, point to periglacial processes acting

on site formation. Slow mass movement in Units 2–4, and more particularly in Units 3–4, evidently occurred. Likely formed in an open-air setting, these units are more detrital, frost-affected sediments that were probably deposited through a combination of gravitational accumulation of debris (rockfall), solifluction and overland flow (slopewash) under periglacial conditions (Matsuoka, 2001; French, 2017), forming a diamictic talus. Units 3–4 are interpreted as head deposits (Facies 3a and 4a; Figs. S11 and S14), which are generally poorly or unsorted, unconsolidated, clastic or matrix-supported periglacial slope deposits (Ballantyne and Harris 1994). Head deposits are commonly associated with solifluction incorporating gravitational scree or gravels and runoff sediments, although there is some variation depending on the local geomorphological context (Harris, 1987, 1998; Ballantyne and Harris, 1994; Bertran and Coutard, 2004).

Solifluction is one of the most widespread processes of downslope mass wasting in both arctic and alpine environments, acting on slopes as low as 1–3° (Washburn, 1967, 1973; Harris, 1981; Matsuoka et al., 2005; French, 2017). This process is often associated with needle ice creep, frost creep, gelifluction, and plug-like flow, inducing low annual movement rates in the range of millimetres to centimetres (Matsuoka, 2001). At La Roche-à-Pierrot, all these forms of solifluction might have been active during the Upper Pleistocene, except plug-like flow. Field observations together with sedimentary features described here, and the presence of frequent frost-shattered geofacts and lithic artefacts found during excavations (e.g., Facies 3a in the JKLM area; Figs. S11 and S12) support this hypothesis. Distinguishing between the different processes and forms involved in solifluction based on our integrated stratigraphic investigations—including fabric and macro/microfacies analysis—is difficult because the observed deposits are immature, and the sedimentary deposits are polygenetic, i.e., they are diachronous, and therefore include hiatuses and different reworking phases spanning several millennia. This means that the primary morphology of original forms (e.g., low/high solifluction lobe, solifluction sheet), signature of frost action type (diurnal versus deeper seasonal movement) or specific features (e.g., shear planes, in relation to miniature slide/flow; runoff action over the palaeo-soil surface) are not easily identified in the fossil record compared to present-day observations (Matsuoka, 2001: Matsuoka et al., 2005; French, 2017).

Our results lead to a few additional observations. The presence of ploughing blocks, as observed in Unit 3, suggests permafrost conditions and active solifluction under a vegetated surface, and more particularly gelifluction (Ballantyne, 2001). The massive structure of the sedimentary deposits or their very crude stratification could result from either progressive accretion linked to sheet solifluction, or the stacking of unsorted solifluction lobes and terraces. Facies showing a clast-supported, poorly sorted diamicton, such as seen in Facies 3a, possibly represent the action of lobes or sheets redistributing coarse cryoclasts (e.g., roof spall from the former overhang) on the slope sur- face, while facies showing a matrix-supported, unsorted diamicton (e.g., Facies 4a) may represent surficial mixing of fine and coarse detritus on the slope. The diamictic facies could involve, in addition to other pro- cesses (especially overland flow), solifluction under a vegetated, her- baceous cover such as in turf-banked solifluction lobes. Such lobes generally have a turf-covered riser and a tread partly or entirely turf-covered (Matsuoka et al., 2005). Buried humic horizons were not identified in the studied lithostratigraphy. Units 3–4 contain only re- sidual microscopic organic silt grains or sparse organic-rich clay aggregates.

Although in open-air periglacial settings, the source of the soil moisture necessary to trigger mass movement is generally snowmelt, our finding of an endokarstic environment adjacent to the site (behind the cliff wall in the mushroom farm) provides a possible source of groundwater that might have migrated laterally to the palaeotalus. Water from this karstic source and/or snowmelt would have been ubiquitous at the site due to the underlying bedrock (below Unit 1) and/or the permafrost table, which possibly functioned as a perched water table and contributed to high levels of moisture to the talus sediments. In this model, the action of gelifluction, which is a particularly efficient thawing process on slope deposits underneath late-lying or perennial snowbanks, would have been key (French, 2017). In such a context, even small-scale slide/flow type movement might have occurred on a debris slope supersaturated by continuous meltwater from a late-lying snowpatch during seasonal thawing (Matsuoka et al., 2005).

In terms of texture, solifluction slopes in arctic and alpine regions mostly consist of fine-textured and frost-susceptible sandy or silty sediment (Washburn, 1967, 1973; Benedict, 1970; Harris, 1981, 1987). Our analysis shows that the sediment from Units 3–4 is well within the limits of frost-susceptible soils (>5% silt-clay; Kaplar, 1974). The clay content of solifluced sediment is generally less than 20%, as is the case at La Roche-à-Pierrot, but higher contents of up to 30% have been reported (Washburn, 1967). Given an adequate supply of water, increased silt content has been shown to increase the susceptibility of soil to solifluction, particularly gelifluction, by increasing frost susceptibility, frost heaving and thaw settlement, and decreasing shearing resistance within the thawing soil (Smith, 2004). Silt content is a crucial variable because gravel and coarse sand are not frost-susceptible and too well drained for saturated flow to occur, whereas plastic clays are too impermeable to support ice lensing (Washburn, 1967).

Sandy and silty solifluction sediment, with low proportions of clay, a situation observed at La Roche-à-Pierrot deposits, generally has low liquid limits, low plasticity indices, and largely frictional strengths (Harris, 1981, 1987). Our microfacies analysis also revealed the loose, non-cohesive structure of the sediment from Units 2–4, which is a key shear strength parameter (Harris, 1987). A high silt/sand content in the fine fraction, inducing a low capacity for water retention, a low cohesion, but also the lack of true swelling clays, the presence of carbonates acting as dispersants, as well as the low organic matter content, are all properties that could make the sediments from Units 2–4 susceptible to solifluction (Todisco and Bhiry, 2008).

Although microscopic shear features such as clay striation also occur in non-cryogenic mass movements (Morgenstern and Tchalenko, 1967), the macroscopic structures and stratigraphic sequencing of the Units 3–4 deposits point to periglacial conditions. Thus, the associated palaeoclimatic setting likely involved permafrost or deep seasonal frost, without excluding diurnal frost action (Fox and Protz, 1981; Harris, 1983, 1998; Van Vliet-Lanoë et al., 1984; Van Vliet-Lanoë, 1987, 1998; Bertran, 1993; Van Steijn et al., 1995; Van Steijn, 2011; Åkerman, 1996; Matsuoka, 2001; Matsuoka et al., 2005; Verpaelst et al., 2017; Mücher et al., 2018). The absence of microscopic evidence of *in situ* frost action in Units 3 and 4, specifically lenticular microstructures and silty-clayey cappings, may be explained by the strongly calcitic composition of the sediment, which prevents clay deposition. In addition, the destructive action of mass wasting deposits at the surface, possibly hampered the preservation of sedimentary frost features (e.g., Pawelec and Ludwikowska-Kędzia, 2016).

Our data shed light on a polygenetic sedimentary environment involving different processes operating at varying rates. For instance, evidence of bone bioerosion of an indeterminate nature and root bioturbation throughout the entire sequence may indicate warmer phases or seasonal warming and low sedimentary rates, which might explain the lack of collagen in some of the bone remains, particularly those from the top of Facies 3a that were exposed on the surface for some time. Also, differential sorting and bedding of the pebble fraction in different Unit 3–4 facies and the fabric data from Facies 3a suggest seasonal runoff reworking bone fragments and lithic artefacts and depositing small limestone clasts, quartz sand and clay from above the cliff on the surface of solifluced sediment (including lobes). In turn, downslope mass movement might have reworked and buried former developed deposits, triggering slope aggradation and reshaping.

Although the macro- and microstructural features observed in Units 2–4 imply cold depositional conditions under periglacial conditions, Units 3–4 were also subject to soil-forming processes under milder

climates throughout their formation, as evidenced by microscopic features such as decalcification, pedality and bioturbation. These processes are best expressed in Unit 4, which seems to show an increased influence of weathering and soil-forming agents in layers closest to the present-day surface. As a last note, the Unit 5 facies, which contain some organic matter, have been subject to recent (historical) anthropogenic disturbance, as observed in locally reworked or truncated areas of the site.

4.4. Anthropogenic input

Macroscopic and microscopic (micromorphological) characteristics of investigated sediments indicate that during the formation of the archaeology-rich basal gray deposit (Unit 2), the JKLM area, which is the highest point of the palaeotalus, was probably a primary area of Mousterian human activity or a preferred zone of discard. This hypothesis is supported by the presence of densely-packed, unsorted, randomly-oriented lithic and bone remains representing a palimpsest of anthropogenic events. In contrast, the archaeological remains from Unit 2 associated with the main sagittal and frontal sections (downslope) are bedded parallel to the slope, which in combination with the presence of microscopic sedimentary rotational features, suggests that this archaeological assemblage was affected by short-distance (a few decimetres to a few metres), low energy syn- and post-depositional slope movement under periglacial conditions. Overall, the microscopic bone assemblage in Unit 2 includes a high proportion of angular burnt fragments, which together with rare instances of microscopic animal-derived char (not from charcoal) indicate intense combustion activity at the site involving animal remains. However, unburnt faunal remains are also frequent, suggesting that the burnt specimens represent reworked combustion residues. With the evidence at hand, possible fuel sources, and the primary location and function of anthropogenic combustion activity at the site remain unknown. Bone likely served as a fuel source (Morin, 2010).

In the quartz-rich diamicton units (Units 3 and 4), microscopic archaeological remains are very scarce and subangular, and microscopic bone remains are weathered, suggesting surface exposure prior to burial by natural sedimentation. The different lines of evidence are consistent with the scenario proposed by Gravina et al. (2018), in which over time, the remains of *in situ* human occupations were seasonally buried by sediment from above the site containing reworked anthropogenic remains, subsequently mixed by slope dynamics, likely through solifluction and runoff in a periglacial setting. Facies 4a may represent a possible change in the position of the slope apex and in sediment transport modality. This change may be part of the "normal" evolution of the slope deposit and/or be a response to climate-driven fluctuations in precipitation or snowfall. The radiocarbon dates obtained for bones embedded in this facies cluster around 40 ka, possibly coinciding with Heinrich Event 4 and Greenland Stadial 9 (Fig. 15). The faunal spectrum in Facies 4a is dominated by cold-adapted species as reflected by a clear focus on reindeer exploitation (Morin, 2012). Small mammals also show the presence of cold-adapted rodents, with Facies 4a providing remains of lemming species such as *Lemmus/Myopus* sp. (Lebreton et al., 2021).

Archaeostratigraphic projections of Units 3–4 archaeological remains and distribution of bone refits (Morin et al., 2005; Morin, 2012; Gravina et al., 2018) show that objects tend to concentrate at the top of Facies 3b and 3e (Mousterian assemblage), the top of Facies 3a (mixed Mousterian and Châtelperronian) and the top of Facies 4a (Aurignacian). At a microscopic scale, there are textural and microstructural differences between Units 3–4 and also internally, among subunits 3a–3b, indicating that they represent distinct, diachronic depositional events. Concentrations of microscopic lithic artefacts and bone remains at the top parts of Units 3 and 4, in agreement with the archaeostrati- graphic data, suggest that less or no human occupation took place at the site during the deposition of the lower parts of these units, and that post-depositional processes did not rework the archaeological remains downward. In conclusion, 1) human occupation during the formation of Units 3–4 was not continuous in time; 2) syn-/post-depositional reworking of lithic and faunal remains by slow mass movement such as solifluction and overland flow affected only the top parts of the soil. This evidence also implies that the Châtelperronian occupations from La Roche-à-Pierrot cannot be the result of mixing of Mousterian and Aurignacian layers as was proposed by some authors (Higham et al., 2010; Mellars, 2010).

4.5. Narrowing down the chronology and exploring the palaeoclimatic setting of the site

Considering our data, further geoarchaeological work should focus on narrowing down the chronology and exploring the climatic setting of the different facies in a Late Pleistocene framework.

Our OSL dating programme was designed to provide a chronological framework for the geoarchaeological and stratigraphic analyses. Specifically, it aimed to constrain both *terminus post quem* (TPQ) and *terminus ante quem* (TAQ) for the artefact-bearing units (facies) by dating the enclosing sediments. The obtained quartz OSL ages allow the temporal distribution of archaeological remains within the studied sections to be assessed, and furthermore provide TPQ and TAQ for the inferred main occupation phases. As the deposits may have formed intermittently on the palaeotalus during MIS3, with possible surface erosive processes and rejuvenation of the topographic profile, it is important to consider the significance of the dates.

It should be borne in mind that both OSL and ^{14}C ages provide a TPQ with respect to periods of sediment deposition, and are therefore only valid if the dated mineral (e.g., quartz grain bleaching) or organic (e.g., fauna) material is contemporaneous with sedimentation. In the opposite case, the ages could be overestimated compared to the real ages of the dated layers or occupation phases. For the ^{14}C dating, any reworked/re-exposed organic material (e.g., from a truncated occupation level) could be older than the enclosing sediments. For the OSL dating, another possibility is that the final bleaching of the quartz grains occurred on the palaeotalus surface following erosive processes (such as slopewash) reworking of previous deposits or proto-occupation levels, and exposing the sediment to light, or under circumstances inducing stratigraphical truncations (cf., possible hiatuses identified in the sections). Under these conditions, the OSL ages must be seen as minimal, with sediments (i.e., quartz grains) younger than the archaeological remains they contain (Lahaye and Hatté, 2023).

These elements highlight the complexity of precisely dating geomorphological processes and difficulties in obtaining true depositional ages for layers on a palaeotalus integrating different evolutive phases. For example, the age for the retreat of the limestone cliff (i.e., the rockfall) is not necessarily the same as when the blocks were completely integrated (buried) in the sedimentary matrix (diamictic facies), nor when they are reworked by mass movement (solifluction) along the slope (e.g., in the form of ploughing blocks), or even partially exposed by surface erosion (slopewash), before being reburied. It is also worth highlighting possible spatial diachronies in sedimentation between the proximal and distal parts of the palaeotalus, which would result in older deposits downslope.

Regarding the chronology, OSL dating provided chronostratigraphically coherent numeric age ranges (Table 1), with relatively small confidence intervals and minimal measurement dispersals following current standards (Duller, 2008). The heterogeneous composition of solifluction features, possibly including lobes and thin sheets, variable low sedimentation rates and the action of overland flow, do not seem to have affected the coherence of the OSL ages. The solifluction deposits at La Roche-à-Pierrot do not contain incompletely or unbleached quartz grains, as previously proposed for quartz and feldspar grains at the top and base of other soliflucted deposits (Völkel and Mahr, 2001; Hülle et al., 2009; Terhorst et al., 2013). In addition, the low collagen yield in bone samples for ^{14}C dating from the lower layers should be remedied by collecting and dating different bone specimens. Our site formation

model entails the coexistence of fresh and weathered bone remains within the same layers following reworking by post-depositional processes such as solifluction.

Regarding the climatic context, at a regional scale, the MIS3 period in which the La Roche-à-Pierrot sequence developed included oscillating periglacial conditions driven by the effects of Heinrich events, which in western Europe entailed a drop of temperature by a few degrees during several hundred to a few thousand years (Hemming, 2004; Fig. 15). The initial collapse of the cavity inducing the formation of Unit 2 might be associated with the Heinrich 5a event (*ca.* 53–55 ka cal BP; Rashid et al., 2003; Hesse and Khodabakhsh, 2017), with the subsequent increase of overhang retreat and exogenous sediment input (Unit 3) linked to Heinrich 5 event (*ca.* 46–48 ka cal BP) and subsequent Greenland Stadials (GS14-10; Rasmussen et al., 2014; Waters et al., 2022; Fig. 17). This evolution might have occurred as shallow caves are likely to record significant thermal changes during cold spells such as Heinrich events (Mammola et al., 2019). Facies 4a might be representative of the Heinrich 4 cooling event (*ca.* 39–40 ka cal BP; Sepulchre et al., 2007; López-García et al., 2013) and GS9. Nevertheless, more accurate positioning of Heinrich events or Greenland stadials within the site's sequence remains subject to 1) precise chronometric (absolute) dating, 2) a clear identification of the primary (stratified) deposits, and 3) associated original palaeo-forms (e.g., low/high solifluction lobes, sheets), as well as 4) their genetic relation (in terms of hiatuses, reworking episodes).

At a local scale, climatic proxies such as compound-specific hydrogen isotope ratios in leaf wax-derived n-alkanes (δDalkanes), which are used for palaeovegetation and palaeohydrological reconstructions in archaeological sequences (e.g., Collins et al., 2017), might help differentiate between permafrost or seasonal frost conditions and determine if the solifluction features at La Roche-à-Pierrot were turf-banked lobes, as in a wet environment, or stone-banked lobes, as in a periglacial desert (Nieuwendam et al., 2020). Further, microscopic bone fragments throughout the sequence exhibit subaerial weathering suggestive of low sedimentary rates and seasonal thaw. Systematic taphonomic analysis of these fragments to characterize their burial conditions by facies might also help clarify the local climatic settings throughout the site's history.

5. Conclusions

In addition to providing new stratigraphic subdivisions and a detailed description of the sedimentary deposits, our multiscalar, multiproxy, geoarchaeological study of the Middle and early Upper Palaeolithic occupations from La Roche-à-Pierrot allows us to propose a site formation model involving the evolution of a karstic cliff face from asemi-closed system to an open-air slope mainly under periglacial con- ditions. These new observations put the archaeological stratigraphy described by Miskovsky and Lévêque (1993), which was based on the study of a single section close to the cliff wall, in a broader geo- archaeological context (Couillet et al., 2022). The new stratigraphic framework provides a bridge between macroscopic and micromorpho- logical observations and helps explain previous spatial inconsistencies in the archaeological sequence. The new geoarchaeological data make it possible to establish correspondences between the lithostratigraphic units and facies and the archaeosequence previously described (Mis- kovsky and Lévêque, 1993; Lévêque, 1997). The basal Mousterian oc- cupations (Unit 2, gray deposit) took place in a semi-closed, sheltered space in which sedimentary rates were low, involving mainly cryoclastic roof spall and episodic percolation of fine-grained sediment. This depositional environment generated a Mousterian archaeological palimpsest in primary position in the proximal area (JKLM zone) and translocated downslope. Subsequent Mousterian, Châtelperronian and Aurignacian remains, embedded within the brown diamictons (Units 3 and 4), were deposited in an open-air context, on the sloping surface at the apex of a palaeotalus, and possibly above the site (top of the cliff). The resulting diachronous surfaces and immature deposits were subject to episodic depositional reworking by solifluction and slopewash, with low sedimentary rates.

A considerable number of chronostratigraphically coherent radiocarbon (n = 12) and OSL (n = 16) ages were secured through our new excavations. The Mousterian, Châtelperronian and Aurignacian occupations occurred during MIS3, and possibly started as early as the end of MIS4 (the oldest age being 59.9 ± 4.3 ka). Both dating methods are independently consistent, in overall agreement and provide a robust chronological framework for the archaeological sequence.

Our results have several important implications for the interpretation of the Middle-to-Upper Palaeolithic transition. First, the base of the JKLM area appears to contain a well-preserved, *in situ* Mousterian archaeological context with limited spatial reworking of cultural remains and evidence for combustion activity. Faunal remains in this zone show moderate weathering. Further investigation of the bioerosion features of the faunal remains recovered during the new excavations will provide more detailed information about the nature and depositional environment in this zone. Second, the Mousterian and Châtelperronian remains found at the top parts of the facies in Unit 3 represent mixed, sporadic anthropogenic events that occurred in different locations, including the top of the cliff (above the site). The Aurignacian remains in Unit 4 also represent sporadic, discrete remains of human occupations clearly independent and unmixed from the specimens associated with the underlying Mousterian or Châtelperronian remains (Morin et al., 2005).

The present work highlights the great potential of a multiscalar, multiproxy site formation research to reduce stratigraphic ambiguity in Pleistocene sites, especially in similar contexts. By providing more robust interpretations of the lithostratigraphic units and/or archaeological sequences (records), this approach helps in better characterizing the taphonomy of cultural remains and contextualizing traces of human behaviour.

Author contributions

D.T. and C.M. are co-first authors of this study. Conceived and designed the experiments: D.T., C.M., C.L., I.C. Performed the experiments: C.M., D.T., C.L., A.C., I.C. Analysed the data: D.T., C.M., C.L., G. G., I.C. Wrote the paper: D.T., C.M., C.L., I.C. Contributed to the acquisition of the data: All authors.

Declaration of competing interest

The authors declare that they have no known competing financial interests or personal relationships that could have appeared to influence the work reported in this paper.

Data availability

Data used are presented in the paper and SOM.

Acknowledgements

The Collective Research Project of La Roche-à-Pierrot is funded by the Direction Régionale des Affaires Culturelles (DRAC) de la Nouvelle-Aquitaine and by the Département de Charente-Maritime (CG 17). The field research also benefited from the financial support of the research project of the New Aquitaine Region: Isotopes du calcium et anthropobiologie au Paléolithique moyen (n° 2019-1R40208), and from the logistical and material support from Archéosphère. We would like to thank the Service Régional d'Archéologie (SRA Nouvelle-Aquitaine), the Charente-Maritime departmental council, and more specifically its archaeological service and its Presidents, Mr. Dominique Bussereau and Mme Sylvie Marcilly, for their support and encouragement. We are grateful in particular to Nathalie Fourment, Olivier Ferullo, Gwenaëlle Marchet-Legendre, Jérôme Primault, Éric Normand, Isabelle Dounies,

Jean-François Héry, Sophie Besnier, Karine Robin, Sébastien Giraud, Ludovic Soler and Emmanuelle Morandière for their help and assistance since 2013. The Paléosite team helped us logistically to organize the field campaigns in the best possible conditions. We are grateful to Vincent Armitano-Grivel and Valérie Roussel for their generosity, trust and support. We would like to thank the mayor of Saint-Césaire and its team. We would also like to thank Caterina Rodriguez and Amiel Arguinzones for their work in the production of thin sections, and Sara Rueda and Javier Davara for their help scanning micromorphological thin sections. Lastly, we thank Mario Gutiérrez and the GeoDig platform for formatting and hosting the high-resolution scans of La Roche-à-Pierrot.

Appendix A. Supplementary data

Supplementary data to this article can be found online.

References

Åkerman, H.J., 1996. Slow mass movements and climatic relationships, 1972-1994, Kapp Linné, west Spitsbergen. In: Anderson, M.G., Brooks, S.M. (Eds.), Advances in Hillslope Processes, vol. 2. Wiley, Chichester, pp. 1219–1256.
Allmendinger, R.W., Cardozo, N., Fisher, D.M., 2011. Structural Geology Algorithms: Vectors and Tensors. Cambridge University Press, p. 304.
Bachellerie, F., 2011. Quelle unité pour le Châtelperronien ? Apport de l'analyse taphonomique et techno-économique des industries lithiques de trois gisements aquitains de plein air: le Basté, Bidart (Pyrénées-Atlantiques) et Canaule II (Dordogne). Unpublished PhD thesis, Université Bordeaux I, p. 441.
Backer, A.M., 1993. Spatial distributions at La Roche à Pierrot, Saint-Césaire: changing uses of a Rockshelter. In: Lévêque, F., Backer, A.M., Guilbaud, M. (Eds.), Context of a Late Neandertal. Implications of Multidisciplinary Research for the Transition to Upper Paleolithic Adaptations at Saint-Césaire, Charente-Maritime, France, Monographs in World Archaeology N°16. Prehistory Press, Madison, pp. 105–127.
Bailey, R.M., Smith, B.W., Rhodes, E.J., 1997. Partial bleaching and the decay form characteristics of quartz OSL. Radiat. Meas. 27 (2), 123–136.
Ballantyne, C.K., 2001. Measurement and theory of ploughing boulder movement. Permafr. Periglac. Process. 12 (3), 267–288.
Ballantyne, C.K., Harris, C., 1994. The Periglaciation of Great Britain. Cambridge University Press, Cambridge, p. 330.
Bar-Yosef, O., Bordes, J.G., 2010. Who were the makers of the Châtelperronian culture? J. Hum. Evol. 59 (5), 586–593.
Batschelet, E., 1981. Circular Statistics in Biology. Academic Press, London, p. 371.
Benedict, J.B., 1970. Downslope soil movement in a Colorado alpine region: rates, processes, and climatic significance. Arct. Alp. Res. 2 (3), 165–226.
Benn, D.I., 1994. Fabric shape and the interpretation of sedimentary fabric data. J. Sediment. Res. A64 (4), 910–915.
Bertran, P., 1993. Deformation-induced microstructures in soils affected by mass movements. Earth Surf. Process. Landforms 18 (7), 645–660.
Bertran, P., Coutard, J.P., 2004. Solifluxion. In: Bertran, P. (Ed.), Dépôts de pente continentaux : dynamique et faciès, vol. 1. Quaternaire, Hors-série, pp. 84–109.
Bertran, P., Hétu, B., Texier, J.P., Steijn, H., 1997. Fabric characteristics of subaerial slope deposits. Sedimentology 44, 1–16.
Bertran, P., Texier, J.P., 1995. Fabric analysis: application to paleolithic sites. J. Archaeol. Sci. 22 (4), 521–535.
Bon, F., 2002. A Brief Overview of Aurignacian Cultures in the Context of the Industries of the Transition from the Middle to the Upper Paleolithic, vol. 45. American School of Prehistoric Research/Instituto Português de Arqueologia, Lisboa, Portugal, pp. 133–144. Trabalhos de Arqueologia.
Bortolot, V.J., 2000. A new modular high capacity OSL reader system. Radiat. Meas. 32 (5), 751–757.
Bos, A.J.J., Wallinga, J., 2012. How to visualize quartz OSL signal components. Radiat. Meas. 47 (9), 752–758.
Bøtter-Jensen, L., Andersen, C.E., Duller, G.A.T., Murray, A.S., 2003. Developments in radiation, stimulation and observation facilities in luminescence measurements. Radiat. Meas. 37 (4–5), 535–541.
Bronk Ramsey, C., 2021. OxCal 4.4. Available at: http://c14.arch.ox.ac.uk/oxcal.
Brönnimann, D., Portmann, C., Pichler, S.L., Booth, T.J., Röder, B., Vach, W., Schibler, J., Rentzel, P., 2018. Contextualising the dead-Combining geoarchaeology and osteoanthropology in a new multi-focus approach in bone histotaphonomy. J. Archaeol. Sci. 98, 45–58.
Brown, T.A., Nelson, D.E., Vogel, J.S., Southon, J.R., 1988. Improved collagen extraction by modified Longin method. Radiocarbon 30 (2), 171–177.
Bourgueil, B., Moreau, P., Vouvé, J., 1968. Saintes, carte géologique détaillée de la France et notice explicative. Bureau de Recherches Géologiques et Minières, Orléans, p. 19.
Carignan, J., Hild, P., Mevelle, G., Morel, J., Yeghicheyan, D., 2001. Routine analyses of trace element in geological samples using flow injection and low pressure on-line liquid chromatography coupled to ICP-MS: a study of geochemical reference materials BR, DR-N, UB-N, AN-G and GH. Geostand. Newsl. 25 (2–3), 187–198.
Collins, J.A., Carr, A.S., Schefuß, E., Boom, A., Sealy, J., 2017. Investigation of organic matter and biomarkers from diepkloof rock shelter, South Africa: insights into middle stone age site usage and palaeoclimate. J. Archaeol. Sci. 85, 51–65.
Colombet, P., 2012. Analyse morphologique et métrique des restes de nouveau-nés inédits du Paléolithique moyen de Saint-Césaire (Charente-Maritime). Unpublished Master 2 thesis, Université de Bordeaux 1, p. 70.
Colombet, P., Bayle, P., Crevecoeur, I., Ferrié, J.G., Maureille, B., 2012. New mousterian neonates from the South-West of France (Saint-Césaire, Charente-Maritime). In: 2nd Annual Meeting of the European Society for the Study of Human Evolution, Bordeaux, France, 21-22 September 2011. European Society for the study of Human Evolution, Leipzig, p. 57.
Conard, N.J., Bolus, M., 2003. Radiocarbon dating the appearance of modern humans and timing of cultural innovations in Europe: new results and new challenges. J. Hum. Evol. 44 (3), 331–371.
Conard, N.J., Bolus, M., 2008. Radiocarbon dating the late middle paleolithic and the aurignacian of the Swabian Jura. J. Hum. Evol. 55 (5), 886–897.
Couillet, A., Rougier, H., Todisco, D., Marot, J., Gillet, O., Crevecoeur, I., 2022. New visual analytics tool and spatial statistics to explore archeological data: the case of the paleolithic sequence of La Roche-à-Pierrot, Saint-Césaire, France. J. Comput. Appl. Archaeol. 5 (1), 19–34.
Coussot, P., Meunier, M., 1996. Recognition, classification and mechanical description of debris flows. Earth Sci. Rev. 40 (3), 209–227.
Dubois, C., Bini, A., Quinif, Y., 2022. Karst morphologies and ghost rock karstification. Géomorphol. Relief, Process. Environ. 28 (1), 13–31.
Dubois, C., Quinif, Y., Baele, J.M., Barriquand, L., Bini, A., Bruxelles, L., Dandurand, G., Havron, C., Kaufmann, O., Lans, B., Maire, R., Martin, J., Rodet, J., Rowberry, M.D., Tognini, P., Vergari, A., 2014. The process of ghost-rock karstification and its role in the formation of cave systems. Earth Sci. Rev. 131, 116-14.
Duller, G.A.T., 2008. Single-grain optical dating of Quaternary sediments: why aliquot size matters in luminescence dating. Boreas 37 (4), 589–612.
Fisher, N.I., 1993. Statistical Analysis of Circular Data. Cambridge University Press, Cambridge, p. 296.
Fox, C.A., Protz, R., 1981. Definition of fabric distributions to characterize the rearrangement of soil particles in the Turbic Cryosols. Can. J. Soil Sci. 61 (1), 29–38.
French, H.M., 2017. The Periglacial Environment, fourth ed. Wiley-Blackwell, p. 544.
Galbraith, R.F., Green, P.F., 1990. Estimating the component ages in a finite mixture. International Journal of Radiation Applications and Instrumentation. Part D. Nuclear Tracks and Radiation Measurements 17 (3), 197–206.
Galland, A., Queffelec, A., Caux, S., Bordes, J.G., 2019. Quantifying lithic surface alterations using confocal microscopy and its relevance for exploring the Châtelperronian at La Roche-à-Pierrot (Saint-Césaire, France). J. Archaeol. Sci. 104, 45–55.
Gravina, B., Bachellerie, F., Caux, S., Discamps, E., Faivre, J.P., Galland, A., Michel, A., Teyssandier, N., Bordes, J.G., 2018. No reliable evidence for a Neanderthal-Châtelperronian association at La Roche-à-Pierrot, Saint-Césaire. Sci. Rep. 8 (1), 15134.
Guérin, G., Christophe, C., Philippe, A., Murray, A.S., Thomsen, K.J., Tribolo, C., Urbanová, P., Jain, M., Guibert, P., Mercier, N., Kreutzer, S., Lahaye, C., 2017. Absorbed dose, equivalent dose, measured dose rates, and implications for OSL age estimates: Introducing the Average Dose Model. Quaternary Geochronology 41, 163–173.
Guérin, G., Mercier, N., Adamiec, G., 2011. Dose-rate conversion factors: update. Ancient Tl 29 (1), 5–8.
Guerin, G., Mercier, N., Nathan, R., Adamiec, G., Lefrais, Y., 2012. On the use of the infinite matrix assumption and associated concepts: a critical review. Radiat. Meas. 47 (9), 778–785.
Guibert, P., Schvoerer, M., 1991. TL dating: low background gamma spectrometry as a tool for the determination of the annual dose. Int. J. Radiat. Appl. Instrum. Nucl. Tracks Radiat. Meas. 18 (1), 231–238.
Hammer, Ø., Harper, D.A., Ryan, P.D., 2001. PAST: paleontological statistics software package for education and data analysis. Palaeontol. Electron. 4 (1), 9.
Harris, C., 1981. Periglacial mass-wasting: a review of research. BGRG Res. Monogr. 4, 204. Norwich, U.K., Geo Abstracts.
Harris, C., 1983. Vesicles in thin sections of periglacial soils from north and south Norway. In: Proceedings of the 4th International Conference on Permafrost. Fairbanks, Alaska, AK, pp. 445–449.
Harris, C., 1987. Solifluction and related periglacial deposits in England and Wales. In: Boardman, J. (Ed.), Periglacial Processes and Landforms in Britain and Ireland. Cambridge University Press, Cambridge, pp. 209–224.
Harris, C., 1998. The micromorphology of paraglacial and periglacial slope deposits: a case study from Morfa Bychan, west Wales, UK. J. Quat. Sci. 13 (1), 73–84.
Hemming, S.R., 2004. Heinrich events: massive late Pleistocene detritus layers of the North Atlantic and their global climate imprint. Rev. Geophys. 42 (1), 1–43. RG1005.
Hesse, R., Khodabakhsh, S., 2017. Reprint of anatomy of Labrador sea Heinrich layers. Mar. Geol. 393, 67–92.
Higham, T., Douka, K., Wood, R., Ramsey, C.B., Brock, F., Basell, L., Camps, M., Arrizabalaga, A., Baena, J., Barroso-Ruíz, C., Bergman, C., 2014. The timing and spatiotemporal patterning of Neanderthal disappearance. Nature 512 (7514), 306–309.
Higham, T., Jacobi, R.M., Bronk Ramsey, C., 2006. AMS radiocarbon dating of ancient bone using ultrafiltration. Radiocarbon 48 (2), 179–195.
Higham, T., Jacobi, R., Julien, M., David, F., Basell, L., Wood, R., Davies, W., Ramsey, C. B., 2010. Chronology of the Grotte du Renne (France) and implications for the context of ornaments and human remains within the Châtelperronian. Proc. Natl. Acad. Sci. U.S.A. 107 (47), 20234–20239.

Hublin, J.J., Talamo, S., Julien, M., David, F., Connet, N., Bodu, P., Vandermeersch, B., Richards, M.P., 2012. Radiocarbon dates from the Grotte du Renne and Saint-Césaire support a Neandertal origin for the Châtelperronian. Proc. Natl. Acad. Sci. U.S.A. 109 (46), 18743–18748.

Hublin, J.J., Sirakov, N., Aldeias, V., Bailey, S., Bard, É., Delvigne, V., Endarova, E., Fagault, Y., Fewlass, H., Hajdinjak, M., Kromer, B., Krumov, I., Marreiros, J., Martisius, N.L., Paskulin, L., Sinet-Mathiot, V., Meyer, M., Pääbo, S., Popov, V., Rezek, Z., Sirakova, S., Skinner, M.M., Smith, G.M., Spasov, R., Talamo, S., Tuna, T., Wacker, L., Welker, F., Wilcke, A., Zahariev, N., McPherron, S.P., Tsanova, T., 2020. Initial Upper Palaeolithic Homo sapiens from Bacho Kiro Cave, Bulgaria. Nature 581 (7808), 299–302.

Hülle, D., Hilgers, A., Kühn, P., Radtke, U., 2009. The potential of optically stimulated luminescence for dating periglacial slope deposits—a case study from the Taunus area, Germany. Geomorphology 109 (1–2), 66–78.

Huntley, D.J., Godfrey-Smith, D.I., Thewalt, M.L., 1985. Optical dating of sediments. Nature 313 (5998), 105–107.

Jain, M., Bøtter-Jensen, L., Singhvi, A.K., 2003. Dose evaluation using multiple-aliquot quartz OSL: test of methods and a new protocol for improved accuracy and precision. Radiat. Meas. 37 (1), 67–80.

Kaplar, C.W., 1974. Freezing test for evaluating relative frost susceptibility of various soils. U.S. Army cold regions research and engineering laboratory, Hanover, New Hampshire, p. 40. Technical Report 250.

Kreutzer, S., Martin, L., Guérin, G., Tribolo, C., Selva, P., Mercier, N., 2018. Environmental dose rate determination using a passive dosimeter: techniques and workflow for α-Al2O3: C chips. Geochronometria 45 (1), 56–67.

Lahaye, C., Hatté, C., 2023. Peuplements pléistocènes dans la Serra da Capivara et questions chronologiques : que date-t-on? In: David, E., Forestier, H., Soriano, S. (Eds.), De la Préhistoire à l'anthropologie philosophique : Recueil de textes offert à Éric Boëda, Cahier d'Anthropologie des Techniques (cahier 6). L'Harmattan, Paris, pp. 629–651.

Lambrecht, G., Rodríguez de Vera, C., Jambrina-Enríquez, M., Crevecoeur, I., Gonzalez-Urquijo, J., Lazuen, T., Monnier, G., Pajović, G., Tostevin, G., Mallol, C., 2021. Characterisation of charred organic matter in micromorphological thin sections by means of Raman spectroscopy. Archaeol. Anthropol. Sci. 13 (1), 13.

Landler, L., Ruxton, G.D., Malkemper, E.P., 2018. Circular data in biology: advice for effectively implementing statistical procedures. Behav. Ecol. Sociobiol. 72 (128), 1–10.

Larqué, P., 2002. Diffractométrie, minéralogie de la fraction argileuse. In: Miskovsky, J. C. (Éd.), Géologie de la préhistoire: Méthodes, techniques, applications, Géopré. Presses universitaires de Perpignan, Paris, pp. 601–613.

Lavaud-Girard, F., 1993. Macrofauna from Castelperronian levels at Saint-Césaire, Charente-Maritime. In: Lévêque, F., Backer, A.M., Guilbaud, M. (Eds.), Context of a Late Neandertal. Implications of Multidisciplinary Research for the Transition to Upper Paleolithic Adaptations at Saint-Césaire, Charente-Maritime, France, Monographs in World Archaeology N°16. Prehistory Press, Madison, pp. 73–77.

Lebreton, L., Morin, E., Gravina, B., Michel, A., Bachellerie, F., Beauval, C., Flas, D., Laroulandie, V., Marot, J., Rougier, H., Tartar, E., Todisco, D., Crevecoeur, I., 2021. The potential of micromammals for the stratigraphy and the timing of human occupations at la Roche-à-Pierrot (Saint-Césaire, France). Quaternary 4 (4), 33.

Lenoble, A., 2005. Ruissellement et formation des sites préhistoriques: référentiel actualiste et exemples d'application au fossile. BAR Publishing (British Archaeological Reports International Series), Oxford, England, p. 212.

Lenoble, A., Agsous, S., 2013. Etude géoarchéologique de la couche 2. Implications sur la préservation des nappes de vestiges. In: Nespoulet, R., Chiotti, L., Henry-Gambier, D. (Eds.), Le Gravettien final de l'Abri Pataud (Dordogne, France). Fouilles 2005-2009. Bristish Archaeological Report, Oxford, pp. 33–42.

Lenoble, A., Bertran, P., 2004. Fabric of Palaeolithic levels: methods and implications for site formation processes. J. Archaeol. Sci. 31 (4), 457–469.

Lévêque, F., 1993. The Castelperronian industry of Saint-Césaire: the upper level. In: Lévêque, F., Backer, A.M., Guilbaud, M. (Eds.), Context of a Late Neandertal. Implications of Multidisciplinary Research for the Transition to Upper Paleolithic Adaptations at Saint-Césaire, Charente-Maritime, France, Monographs in World Archaeology N°16. Prehistory Press, Madison, pp. 23–26.

Lévêque, F., 1997. Le Passage du Paléolithique moyen au Paléolithique supérieur: données stratigraphiques de quelques gisements sous-grotte du sud-ouest. Quaternaire 8 (2–3), 279–287.

Lévêque, F., Vandermeersch, B., 1980. Les découvertes de restes humains dans un horizon castelperronien de Saint-Césaire (Charente-Maritime). Bull. Soc. Prehist. Fr. 77 (2), 187–189.

López-García, J.M., Blain, H.A., Bennasar, M., Sanz, M., Daura, J., 2013. Heinrich event 4 characterized by terrestrial proxies in southwestern Europe. Clim. Past 9 (3), 1053–1064.

Mammola, S., Piano, E., Cardoso, P., Vernon, P., Domínguez-Villar, D., Culver, D.C., Pipan, T., Isaia, M., 2019. Climate change going deep: the effects of global climatic alterations on cave ecosystems. Anthropocene Rev. 6 (1–2), 98–116.

Matsuoka, N., 2001. Solifluction rates, processes and landforms: a global review. Earth Sci. Rev. 55 (1), 107–134.

Matsuoka, N., Ikeda, A., Date, T., 2005. Morphometric analysis of solifluction lobes and rock glaciers in the Swiss Alps. Permafr. Periglac. Process. 16 (1), 99–113.

McPherron, S.J., 2005. Artifact orientations and site formation processes from total station proveniences. J. Archaeol. Sci. 32 (7), 1003–1014.

McPherron, S.P., 2018. Additional statistical and graphical methods for analyzing site formation processes using artifact orientations. PLoS One 13 (1), e0190195.

Mellars, P., 2010. Neanderthal symbolism and ornament manufacture: the bursting of a bubble? Proc. Natl. Acad. Sci. U.S.A. 107 (47), 20147–20148.

Menzies, J., 2000. Micromorphological analyses of microfabrics and microstructures indicative of deformation processes in glacial sediments. Geol. Soci., Lond., Spec. Pub. 176 (1), 245–257.

Menzies, J., Meer, J.J.M., 2018. Micromorphology and microsedimentology of glacial sediments. In: Menzies, J., van der Meer, J.J.M. (Eds.), Past Glacial Environments, second ed. Elsevier, pp. 753–806.

Menzies, J., Paulen, R.C., Rice, J.M., McClenaghan, M.B., Oviatt, N.M., Dhillon, N., 2019. Deformation "boundary front" movements in subglacial tills-A microsedimentological perspective from till sequences near Pine Point, NWT, Canada. Deposit. Record 5 (2), 230–246.

Mercier, N., Valladas, H., Joron, J.L., Reyss, J.L., Lévêque, E., Vandermeersch, B., 1991. Thermoluminescence dating of the late Neanderthal remains from Saint-Césaire. Nature 351, 737–739.

Mercier, N., Valladas, H., Joron, J.L., Reyss, J.L., 1993. Thermoluminescence dating of the prehistoric site of La Roche à Pierrot, Saint-Césaire. In: Lévêque, F., Backer, A.M., Guilbaud, M. (Eds.), Context of a Late Neandertal. Implications of Multidisciplinary Research for the Transition to Upper Paleolithic Adaptations at Saint-Césaire, Charente-Maritime, France, Monographs in World Archaeology N°16, Prehistory Press, Madison, pp. 15–21.

Millar, S.W.S., 2005. Fabric variability associated with periglacial mass-wasting at Eagle Summit, Alaska. Geomorphology 72, 222–237.

Miskovsky, J.C., Lévêque, F., 1993. The sediments and stratigraphy of Saint-Césaire: contributions to the paleoclimatology of the site. In: Lévêque, F., Backer, A.M., Guilbaud, M. (Eds.), Context of a Late Neandertal. Implications of Multidisciplinary Research for the Transition to Upper Paleolithic Adaptations at Saint-Césaire, Charente-Maritime, France, Monographs in World Archaeology N°16. Prehistory Press, Madison, pp. 9–14.

Morgenstern, N.R., Tchalenko, J.S., 1967. Microstructural observations on shear zones from slips in natural clays. In: Proceedings of the Geotechnical Conference, Oslo, pp. 147–152.

Morin, E., 2010. Taphonomic implications of the use of bone as fuel. Palethnologie 2, 209–217.

Morin, E., 2012. Reassessing Paleolithic Subsistence: the Neandertal and Modern Human Foragers of Saint-Césaire. Cambridge University Press, New York, p. 350.

Morin, E., Tsanova, T., Sirakov, N., Rendu, W., Mallye, J.B., Lévêque, F., 2005. Bone refits in stratified deposits: testing the chronological grain at Saint-Césaire. J. Archaeol. Sci. 32 (7), 1083–1098.

Mücher, H., van Steijn, H., Kwaad, F., 2018. Colluvial and mass wasting deposits. In: Stoops, G., Marcelino, V., Mees, F. (Eds.), Interpretation of Micromorphological Features of Soils and Regoliths, second ed. Elsevier, pp. 21–36.

Murray, A.S., Arnold, L.J., Buylaert, J.P., Guérin, G., Qin, J., Singhvi, A.K., Smedley, R., Thomsen, K.J., 2021. Optically stimulated luminescence dating using quartz. Nat. Rev. Methods Primers 1 (1), 1–31.

Murray, A.S., Wintle, A.G., 2003. The single aliquot regenerative dose protocol: potential for improvements in reliability. Radiat. Meas. 37 (4), 377–381.

Nieuwendam, A., Vieira, G., Schaefer, C., Woronko, B., Johansson, M., 2020. Reconstructing cold climate paleoenvironments from micromorphological analysis of relict slope deposits (Serra da Estrela, Central Portugal). Permafr. Periglac. Process. 31 (4), 567–586.

Patou-Mathis, M., 1993. Taphonomic and paleoethnographic study of the fauna associated with the Neandertal of Saint-Césaire. In: Lévêque, F., Backer, A.M., Guilbaud, M. (Eds.), Context of a Late Neandertal. Implications of Multidisciplinary Research for the Transition to Upper Paleolithic Adaptations at Saint-Césaire, Charente-Maritime, France, Monographs in World Archaeology N°16. Prehistory Press, Madison, pp. 81–102.

Pawelec, H., Ludwikowska-Kędzia, M., 2016. Macro- and micromorphologic interpretation of relict periglacial slope deposits from the Holy Cross mountains, Poland. Permafr. Periglac. Process. 27 (2), 229–247.

Peresani, M., Bertola, S., Delpiano, D., Benazzi, S., Romandini, M., 2019. The Uluzzian in the north of Italy: insights around the new evidence at Riparo Broion. Archaeol. Anthropol. Sci. 11 (7), 3503–3536.

Prescott, J.R., Hutton, J.T., 1988. Cosmic ray and gamma ray dosimetry for TL and ESR. Int. J. Radiat. Appl. Instrum. Nucl. Tracks Radiat. Meas. 14 (1), 223–227.

Rashid, H., Hesse, R., Piper, D.J.W., 2003. Evidence for an additional Heinrich event between H5 and H6 in the Labrador sea. Paleoceanography 18 (4), 1077.

Rasmussen, S.O., Bigler, M., Blockley, S.P., Blunier, T., Buchardt, S.L., Clausen, H.B., Cvijanovic, I., Dahl-Jensen, D., Johnsen, S.J., Fischer, H., Gkinis, V., 2014. A stratigraphic framework for abrupt climatic changes during the Last Glacial period based on three synchronized Greenland ice-core records: refining and extending the INTIMATE event stratigraphy. Quat. Sci. Rev. 106, 14–28.

Reimer, P.J., Austin, W.E.N., Bard, E., Bayliss, A., Blackwell, P.G., Bronk Ramsey, C., Butzin, M., Cheng, H., Edwards, R.L., Friedrich, M., Grootes, P.M., Guilderson, T.P., Hajdas, I., Heaton, T.J., Hogg, A.G., Hughen, K.A., Kromer, B., Manning, S.W., Muscheler, R., Palmer, J.G., Pearson, C., van der Plicht, J., Reimer, R.W., Richards, D.A., Scott, E.M., Southon, J.R., Turney, C.S.M., Wacker, L., Adolphi, F., Büntgen, U., Capano, M., Fahrni, S.M., Fogtmann-Schulz, A., Friedrich, R., Köhler, P., Kudsk, S., Miyake, F., Olsen, J., Reinig, F., Sakamoto, M., Sookdeo, A., Talamo, S., 2020. The IntCal20 northern hemisphere radiocarbon age calibration curve (0–55 cal kBP). Radiocarbon 62 (4), 725–757.

Richter, D., Dombrowski, H., Neumaier, S., Guibert, P., Zink, A.C., 2010. Environmental gamma dosimetry with OSL of α-Al_2O_3:C for in situ sediment measurements. Radiat. Protect. Dosim. 141 (1), 27–35.

Roberts, R.G., Galbraith, R.F., Yoshida, H., Laslett, G.M., Olley, J.M., 2000. Distinguishing dose populations in sediment mixtures: a test of single-grain optical dating procedures using mixtures of laboratory-dosed quartz. Radiation Measurements 32 (5–6), 459–465.

Schick, K.D., 1987. Modeling the formation of early stone age artifact concentrations. J. Hum. Evol. 16 (7–8), 789–807.
Sellier, D., 2010. L'analyse intégrée du relief et la sélection déductive des géomorphosites : application à la Charente-Maritime (France). Géomorphol. Relief, Process. Environ. 16 (2), 199–214.
Sepulchre, P., Ramstein, G., Kageyama, M., Vanhaeren, M., Krinner, G., Sánchez -Goñi, M.F., d'Errico, F., 2007. H4 abrupt event and late Neanderthal presence in Iberia. Earth Planet Sci. Lett. 258 (1–2), 283–292.
Slimak, L., Zanolli, C., Higham, T., Frouin, M., Schwenninger, J.L., Arnold, L.J., Demuro, M., Douka, K., Mercier, N., Guérin, G., Valladas, H., Yvorra, P., Guiraud, Y., Seguin-Orlando, Orlando, L., Lewis, E., Muth, X., Camusse, H., Vandelvelde, S., Buckley, M., Mallol, C., Stringer, C., Metz, L., 2022. Modern human incursion into Neanderthal territories 54,000 years ago at Mandrin, France. Sci. Adv. 8 (6) eabj9496.
Smith, J.S., 2004. Scaled geotechnical centrifuge modelling of gelifluction. Unpublished PhD thesis, School of Earth, Ocean and Planetary Sciences, University of Wales, Cardiff, p. 443.
Soressi, M., 2010. La Roche-à-Pierrot à Saint-Césaire (Charente-Maritime). Nouvelles données sur l'industrie lithique du Châtelperronien. In: Buisson-Catil, J., Primault, J. (Eds.), Préhistoire entre Vienne et Charente. Hommes et sociétés du Paléolithique. Association des Publications Chauvinoises, Mémoire 38, Chauvigny, pp. 191–202.
Soressi, M., 2011. Révision taphonomique et techno-typologique des deux ensembles attribués au Châtelperronien de la Roche-à-Pierrot à Saint-Césaire. L'Anthropologie 115 (5), 569–584.
Stringer, C.B., Hublin, J.J., Vandermeersch, B., 1984. The origin of anatomically modern humans in Western Europe. In: Smith, F., Spencer, F. (Eds.), The Origin of Modern Humans: A World Survey of the Fossil Evidence. Alan R. Liss, New York, pp. 51–135.
Talamo, S., Aldeias, V., Goldberg, P., Chiotti, L., Dibble, H.L., Guérin, G., Hublin, J.J., Madelaine, S., Maria, R., Sandgathe, D., Steele, T.E., 2020. The new 14 C chronology for the Palaeolithic site of La Ferrassie, France: the disappearance of Neanderthals and the arrival of Homo sapiens in France. J. Quat. Sci. 35 (7), 961–973.
Talamo, S., Richards, M., 2011. A comparison of bone pretreatment methods for AMS dating of samples >30,000 BP. Radiocarbon 53 (3), 443–449.
Terhorst, B., Kleber, A., Bibus, E., 2013. Relative dating with cover beds. In: Kleber, A., Terhorst, B. (Eds.), Developments in Sedimentology. Elsevier, pp. 229–251.
Teyssandier, N., 2008. Revolution or evolution: the emergence of the Upper Paleolithic in Europe. World Archaeol. 40 (4), 493–519.
Thiébaut, C. 2005. Le Moustérien à denticulés: Variabilité ou diversité techno-économique? Unpublished PhD thesis, Université de Provence, AiX-Marseille 1, p. 231 + p. 635.
Thiébaut, C., Meignen, L., Lévêque, F., 2009. Les dernières occupations moustériennes de Saint-Césaire (Charente-Maritime, France): diversité des techniques utilisées et comportements économiques pratiqués. Bull. Soc. Prehist. Fr. 106 (4), 691–714.
Todisco, D., Bhiry, N., 2008. Palaeoeskimo site burial by solifluction: periglacial geoarchaeology of the Tayara site (KbFk-7), Qikirtaq Island, nunavik (Canada). Geoarchaeology: Int. J. 23, 177–211.
Trinkaus, E., Shipman, P., 2005. Neandertals: Images of ourselves. Evol. Anthropol. 1 (6), 194–201.
Vandermeersch, B., Hublin, J.J., 2007. Les derniers Néandertaliens. In: Vandermeersch, B., Maureille, B. (Eds.), Les Néandertaliens, biologie et cultures, Paris, Éditions du Comité des travauX historiques et scientifiques, Documents préhistoriques 23, pp. 109–115.
Van Steijn, H., 2011. Stratified slope deposits: periglacial and other processes involved. Geological Society, London, Special Publications 354 (1), 213–226.
Van Steijn, H., Bertran, P., Francou, B., Texier, J.P., Hétu, B., 1995. Models for the genetic and environmental interpretation of stratified slope deposits: review. Permafr. Periglac. Process. 6 (2), 125–146.
Van Vliet-Lanoë, B., 1987. Dynamique périglaciaire actuelle et passée: apport de l'étude micromorphologique et de l'expérimentation. Quaternaire 24 (3), 113–132.
Van Vliet-Lanoë, B., 1998. Frost and soils: implications for paleosols, paleoclimates and stratigraphy. Catena 34 (1–2), 157–183.
Van Vliet-Lanoë, B., Coutard, J.P., Pissart, A., 1984. Structures caused by repeated freezing and thawing in various loamy sediments: a comparison of active, fossil and experimental data. Earth Surf. Process. Landforms 9 (6), 553–565.
Van Vliet-Lanoë, B., Fox, C.A., 2018. Frost action. In: Stoops, G., Marcelino, V., Mees, F. (Eds.), Interpretation of Micromorphological Features of Soils and Regoliths, second ed. Elsevier, pp. 575–603.
Verpaelst, M., Fortier, D., Kanevskiy, M., Paquette, M., Shur, Y., 2017. Syngenetic dynamic of permafrost of a polar desert solifluction lobe, Ward Hunt Island, Nunavut. Arctic Sci. 3 (2), 301–319.
Völkel, J., Mahr, A., 2001. Die IRSL-Datierung von periglazialen Hangsedimenten-Ergebnisse aus dem Bayerischen Wald. Z. Geomorphol. 45 (3), 295–305.
Washburn, A.L., 1967. Instrumental observations of mass-wasting in the Mesters Vig district, N.E. Greenland. Meddelelser om Grønland 166 (4), 1–318.
Washburn, A.L., 1973. Periglacial Processes and Environments. Edward Arnold, London, p. 320.
Waters, C.N., Williams, M., Zalasiewicz, J., Turner, S.D., Barnosky, A.D., Head, M.J., Wing, S.L., Wagreich, M., Steffen, W., Summerhayes, C.P., Cundy, A.B., Zinke, J., Fiałkiewicz-Kozieł, B., Leinfelder, R., Haff, P.K., McNeill, J.R., Rose, Neil L., Hajdas, I., McCarthy, F.M.G., Cearreta, A., Gałuszka, A., Syvitski, J., Han, Y., An, Z., Fairchild, I.J., Ivar do Sul, J.A., Jeandel, C., 2022. Epochs, events and episodes: marking the geological impact of humans. Earth Sci. Rev. 234, 104171.
Wintle, A.G., 1997. Luminescence dating: laboratory procedures and protocols. Radiat. Meas. 27 (5), 769–817.
Wintle, A.G., Murray, A.S., 2000. Quartz OSL: effects of thermal treatment and their relevance to laboratory dating procedures. Radiat. Meas. 32 (5), 387–400.

A multiscalar and multiproxy geoarchaeological approach to site formation processes at the Middle and Upper Palaeolithic site of La Roche-à-Pierrot, Saint-Césaire, France.

Supplementary Online Material (SOM) - Quaternary Science Reviews

Dominique Todisco[a, *], Carolina Mallol[b, c, d, **], Christelle Lahaye[e], Guillaume Guérin[f], François Bachellerie[g, t], Eugène Morin[h], Brad Gravina[i, t], Amélie Challier[e, j], Cédric Beauval[k], Jean-Guillaume Bordes[t], Céline Colange[a], Laure Dayet[l], Damien Flas[m, n], François Lacrampe-Cuyaubère[k], Loïc Lebreton[o, p, q], Josserand Marot[r], Bruno Maureille[t], Alexandre Michel[s, t], Xavier Muth[u, v], Carole Nehme[a], Solange Rigaud[t], Elise Tartar[n], Nicolas Teyssandier[n], Marc Thomas[n], Hélène Rougier[w], Isabelle Crevecoeur[t]

a *IDEES, UMR 6266, CNRS, Université de Rouen, Bâtiment 7, 17 rue Lavoisier, 76821 Mont Saint Aignan Cedex, France*
b *Instituto Universitario de Bio-Orgánica Antonio González, Universidad de La Laguna, Avda. Astrofísico Fco. Sánchez, 2. 38206 San Cristóbal de La Laguna, Tenerife, Spain*
c *Departamento de Geografía e Historia, UDI Prehistoria, Arqueología e Historia Antigua, Facultad de Humanidades, Universidad de La Laguna, 38206 San Cristóbal de La Laguna, Tenerife, Spain*
d *Department of Anthropology, University of California, One Shields Ave, Davis, CA 95616, USA*
e *Archéosciences Bordeaux, UMR 6034, CNRS, Université Bordeaux Montaigne, Maison de l'Archéologie, Esplanade des Antilles, 33607 Pessac, France*
f *Géosciences Rennes, UMR 6118, CNRS, Bâtiment 15, Campus Beaulieu, Université de Rennes 1, 35042 Rennes, France*
g *Archéologie Alsace, 11 rue Champollion, 67600 Sélestat, France*
h *Department of Anthropology, Trent University, DNA Block C, 2140 East Bank Drive, Peterborough, ON, K9J 7B8, Canada*
i *Musée national de Préhistoire, 1 rue du Musée, 24620 Les Eyzies-de-Tayac, France*
j *Department of Physics, Technical University of Denmark, DTU Risø Campus, 4500 Roskilde, Denmark*
k *SARL Archéosphère, 10 rue de la Rhode, 11500 Quillan, France*
l *EDYTEM, UMR 5204, CNRS, Université Savoie Mont Blanc, Bâtiment Pôle Montagne, 5 boulevard de la Mer Caspienne, 73376 Le Bourget du Lac Cedex, France*
m *Service de Préhistoire, Université de Liège, 7 Place du 20 Août, 4000 Liège, Belgium*
n *TRACES, UMR 5608, CNRS, Université de Toulouse Jean Jaurès, Maison de la Recherche, 5 allée Antonio Machado, 31058 Toulouse Cedex 9, France*
o *Institut Català de Paleoecologia Humana i Evolució Social (IPHES-CERCA), Zona Educacional 4, Campus Sescelades URV, Edifici W3, 43007 Tarragona, Spain*
p *Universitat Rovira i Virgili, Departament d'Història i Història de l'Art, Avinguda de Catalunya 35, 43002 Tarragona, Spain*
q *HNHP, UMR 7194, CNRS, Département Homme et Environnement du Muséum National d'Histoire Naturelle, CNRS-UPVD, Musée de l'Homme, 75116 Paris, France*
r *Service départemental de l'Archéologie, Maison du Département, 85 Boulevard de la République, 17076 La Rochelle Cedex 09, France*
s *Service départemental de l'Archéologie, Conseil Départemental de la Dordogne, 2 rue Paul Louis Courier, CS11200, 24019 Périgueux Cedex, France*
t *PACEA, UMR 5199, CNRS, Université de Bordeaux, Bâtiment B2, Allée Geoffroy Saint Hilaire, 33615 Pessac, France*
u *SARL Get in Situ, Place Rodolphe Théophile Bosshard 1, CH1097 Riex, Switzerland*
v *School of Engineering and Management Vaud, HES-SO University of Applied Sciences and Arts Western Switzerland, CH1401 Yverdon-les-Bains, Switzerland*
w *Department of Anthropology, California State University Northridge, 18111 Nordhoff St., Northridge, CA 91330-8244, USA*

* Corresponding author.
** Corresponding author.

E-mail addresses: dominique.todisco@univ-rouen.fr (D. Todisco), cmallol@ull.edu.es (C. Mallol).

1. A brief history of excavations

La Roche-à-Pierrot was discovered fortuitously by B. Dubigny in 1976, as the site was truncated by the construction of a road leading to an abandoned mushroom farm. The historical mushroom farm, currently an empty cavity behind the site, was located in a disused enclosed quarry cut into the limestone cliff. Realizing the potential importance of the site, F. Lévêque undertook rescue excavations at the site between 1977 and 1979. Following the discovery of the Saint-Césaire 1 partial Neanderthal skeleton in 1979, the excavation and recording protocol became more meticulous, introducing 50 x 50 cm sub-squares, tridimensional piece-plotting of certain artefact types, 5 cm spits and systematic field notes, drawings and photographs (Backer, 1994; Lévêque, 2002). The systematic excavation of the site, pursued annually over a 52 m² area, continued until 1987 under the supervision of F. Lévêque (Lévêque, 1993). Approximately half of this area was entirely excavated, with the sediments removed to the bedrock (Figure S1 and Figure 3, main text). In 1993, F. Lévêque resumed excavations at the site with the help of A. Backer, the aim being to stabilize the archaeological sections, work that Backer completed in 1997 (Backer, 1994, 1997).

New excavations were initiated in 2013 under the direction of F. Bachellerie and E. Morin (2013-2014), with the aim of producing a better understanding of the site's stratigraphic sequence as well as identifying site formation processes from a multiscalar and multiproxy geoarchaeological perspective (Bachellerie et al. 2014). Continued under the direction of I. Crevecoeur since 2015, ongoing excavations focus on collecting new field data and reassessing information from the original excavations, including archival information, using both new modelling techniques and analytical methods (Crevecoeur, 2017; Couillet al., 2022).

The new excavations have made it possible to better interpret the archaeological stratigraphy established by Miskovsky and Lévêque (1993) based on a reference section located in the area of the site closest to the cliff, which is probably not representative of the entire site (Couillet et al., 2022). One of the main problems with the reference section (Figure 3, main text), described primarily on the basis of archaeological, sedimentological and colour attributes observed over a small area, is that it was considered valid for the whole site without taking into account any hiatuses, unconformities or lateral changes in sedimentary facies.

2. Supplementary data

2.1. Provenience of the samples

Samples were collected at the site, the mushroom farm behind and the open-pit limestone quarry exposures in order to perform geochemistry, micromorphology, OSL and ^{14}C dating (Tables S1-3). Provenience of the intra-, peri- and off-site samples used for laboratory analyses is indicated in Figures S2-S7.

2.2. Geomorphological observations

In the small historical quarry/mushroom farm adjoining the site, karst features observed in the Upper Turonian limestone include a chimney, a solution dome, a level of ghost-rock weathering (around 31 m asl), grayish alterites (isalterites), alveolus, dissolution forms, and Liesegang bands (Figures S8 and S9). Off-site features at the open-pit quarry (Figure S10) include reddish clays with flint and mottling (top of the Cretaceous plateau), a karstified Middle Coniacian limestone overlooking Lower Coniacian quartz and glauconite sand bed, grayish clayey alterites (isalterites) associated with Middle Coniacian limestone, and a possible level of ghost-rock karstification in the Upper Turonian limestone (Figure S7).

Field observations of the site's sedimentary sequence reveal the likely action of slope mass movement in site formation. Figure S11 shows the crude stratification of diamictic macrofacies 3a and 4a observed in squares K4 and J5. In level EJOP (Levêque's excavation, Figure 3, main text), and in macrofacies 3a (new excavation),

possible solifluction features in the form of small-sized lobes (Figure S12) suggest slow downslope reworking of archaeological remains, limestone clasts and fine-grained sediments (derived from alterites/surficial formations) in a periglacial environment (Figure S13).

2.3. The lithostratigraphic matrix

At La Roche-à-Pierrot, the exposed sequence has a dome-shaped morphology, with the apex at the JKLM area and a pronounced NW dip (22–24°). This sequence comprises five main lithostratigraphic units, subdivided into different facies, numbered (units) and lettered (subunits) from base to top and from the JKLM (proximal part) to the frontal section (distal part). The facies subdivision reflects stratigraphic order and lateral variability in texture, structure, and colour. An additional sedimentary unit, Q-1, corresponds to the remains of a sedimentary deposit within the mushroom farm behind the site (square J100, axis of the diaclase; Figure S6). This deposit has not been stratigraphically correlated with the site's sequence.

We present graphic illustrations of the stratigraphy showing the facies identified throughout the different sections (Figures 4-7, main text) and stratigraphic correlations between the observed macrofacies and the former archaeostratigraphic units established by Lévêque (Figure 8, main text). Lithostratigraphic matrix with field descriptions of the units and subunits and their representation across the sections is presented in Figure S14.

2.4. Geochemistry

In order to perform X-Ray Diffraction (XRD) analyses bulk samples were milled. Sieved and bulk fractions were prepared for XRD analysis using a back loading preparation method or a zero-background sample holder, depending on the amount of sample. Non-oriented powder from a 53-micron sieve was analysed using a PANalytical Empyrean/Aeris diffractometer with PIXcel detector and fixed slits with Fe filtered Co-Kα radiation. In order to establish the presence of smectite and/or chlorite, the fractions were exposed to an ethylene glycol atmosphere and rescanned. In order to establish the presence of serpentine (lizardite) and/or kaolinite, the samples were heated to 500°C and rescanned. Amorphous phases, if present, were not taken into consideration during quantification.

The Rietveld refinement method was used as a full-profile approach allowing quantitative phase-analysis to be performed (Rietveld, 1969; Bish, 1993; Young, 1993). The least-squares refinements were carried out until the best fit between the powder diffraction data and the calculation pattern data based on the refined models. This pattern-fitting method of structure refinement is based on a large number of simulated parameters and makes efficient use of the maximum amount of information contained in the diffraction (powder) pattern and converts it into an effective analysis procedure. An important requirement of the quantitative analysis of phase proportions (or mineral groups) is that the diffraction patterns consist of well-defined Bragg reflections.

The XRD analysis identified six main crystalline phases (quartz, kaolinite, muscovite, calcite, goethite, and smectite) and four secondary phases (apatite, biotite, plagioclase, and microcline) in the sediment (Tables S4 and S5). Smectite is generally formed in poorly drained or confined, alkaline substrates, whereas kaolinite is often formed in well-drained acidic soils, especially in Mediterranean, subtropical and tropical climates. In the smectite group, the presence of montmorillonite was specified for certain extra-site samples. Presence of interlayered illite-montmorillonite-type clays is conceivable since illite can be formed by weathering of smectite, but their proportions are below detection limit. Goethite was the only metal oxide-hydroxide detected in the tested samples. Goethite is formed under oxidizing conditions. No hematite (iron oxide), gibbsite (aluminium hydroxide) or manganese oxides were identified.

Among primary minerals, quartz dominates ahead of muscovite (mica), and calcite is ubiquitous and predominates in the intra-site and karstic samples. Its

presence is related to the weathering and disaggregation of the limestone substrate and to diagenetic and pedogenic processes. Raw data (used for PCA analysis) concerning major-minor elements (dose percentages) quantified by ICP-OES, loss on ignition (LOI) values, and trace elements (µg/g; ppm) quantified by ICP-MS, are presented in Tables S6 and S7.

2.5. Micromorphology

Micromorphological thin sections were manufactured by Spectrum Petrographics (7.5 cm x 5 cm x 30 µm) and Thomas Beckmann (9 cm x 6 cm x 30 µm). The thin sections were analysed using Nikon Eclipse, Nikon AZ100 Multizoom and Nikon SMZ18 petrographic microscopes using transmitted, plane (PP) and crossed polarized (XP) light and blue light. Standard descriptive guidelines (Stoops, 2003) and specialized micromorphological literature (Menzies, 2000; Stoops et al., 2010; Nicosia and Stoops, 2017) were used as references for the identification of microstructural features.

The micromorphological data presented in the main text are based on samples collected from: 1) the sagittal and frontal profiles of Lévêque's excavations and JKLM area (Figure 3, main text), 2) a geological formation exposed in the open-pit limestone quarry and 3), a sedimentary infill exposed inside the mushroom farm, behind the back wall of the site (Table S2 and Figures S2-S6). In the main text, we outline the main micromorphological features observed throughout the sequence and illustrate these with selected microphotographs. Summarized micromorphological descriptions, sample provenience and schematic representations of the main microfeatures can be found in Figure S15. Hyperlinks to high-resolution scans of selected thin sections are provided in Table S8.

2.6. Fabric analysis

Orientations between 0 and 360° were processed with Oriana software (Kovach, 2011). To characterize the fabric of tested squares, different statistical parameters were calculated, and several types of analyses were performed. The mean orientation vector was characterized by its direction (mean vector, µ) and its length (r). Related to the latter, the concentration parameter (k), specific to the Von Mises distribution, was calculated because it measures the fit of a tested distribution to a perfect circle (uniformity). In addition, the circular variance and the circular standard deviation were also determined. To test diametrically bimodal distributions, the method of angle doubling (axial data analysis) was applied (Batschelet, 1981). Rayleigh's uniformity test (Fisher, 1993; Zar, 2010) was applied to calculate the probability of the null hypothesis that the data (orientations) are distributed in a uniform manner (random distribution). This parametric test only makes sense if the distribution of orientations is unimodal. In addition, the Rayleigh test is sensitive to the sample size. The larger the count, the smaller the p-value returned by the test tends to be. The uniformity of the orientation distributions or their adjustment to normality (Von Mises distribution) has also been tested using Watson's U^2 and Kuiper's tests (Batschelet, 1981; Fisher, 1993; Lenoble, 2005; Zar, 2010; Landler et al., 2018).

Rao's spacing test has also been used as it takes its null hypothesis that the data are uniformly distributed. Rao's test can be more powerful than Rayleigh's or Kuiper's tests to characterize the distributions that are not unimodal or diametrically bimodal, and can sometimes help to detect multimodal distributions (Batschelet, 1981). However, it should be emphasized that commonly used tests (such as Rao's spacing test, Watson's U^2 test, and Kuiper's test) may lack statistical power in many multimodal cases, i.e., with data concentrated in several directions (Landler et al., 2018). In addition, if transformation of the raw data (e.g., by doubling the angles) can overcome some of the issues, it is only in the case of perfect f-fold symmetry.

Finally, the nonparametric Moore's paired test was performed to compare two fabric series of paired data. This test examines whether paired observations differ between the two series, using Moore's modified Rayleigh

test. The null hypothesis is that there is no difference between the two tested series (fabrics).

For Facies 4a-sup. (Table S9), at square J4 and the J3-J4 group, the p-value of the different tests is always significant (threshold < 0.05), including on the axial data (with doubled angles), thus rejecting the null hypothesis that the analysed fabric corresponds to the tested distributions (uniform or von Mises). For square J3, only Watson's U^2 and Kuiper's tests reject the uniformity of the distribution, as does Rao's spacing test carried out on the axial data.

For Facies 4a-inf. (Table S10), the uniformity of the distributions is rejected for all tested squares or groups except for K4, for which only the Kuiper's test shows a significant p-value. When the angles are doubled, Rao's spacing test is significant for most series except for K4, rejecting the hypothesis of a uniform orientation. On the axial data, the Rayleigh's uniformity test has a significant p-value only at square J5. This square shows a significant p-value for all tests applied, on the initial angles or doubled ones, rejecting the adjustment to a von Mises-type distribution.

For Facies 3a (Table S11), the Rayleigh test shows a significant p value at square K4 and the J4-J5 group, thus rejecting the hypothesis of a uniform orientation. The Rao's spacing test, which can be more powerful than the Rayleigh test, is significant for most series except for K4 square. The adjustment of the series to uniformity, by Watson's U^2 and Kuiper's tests, is also most often rejected, except for J4 and J5, respectively. Furthermore, fitting the series to a von Mises distribution is rejected by Watson's U^2 test, except for square J4. When the axial data are analysed, Rayleigh's test has a significant p-value for square J5 and J4-J5 and J5-K5 groups. Watson's U^2 and Kuiper's tests reject uniformity of distributions for J5, K4-K5, J4-J5 and J5-K5 while Rao's spacing test is significant for J4, J5, J4-J5 and J5-K5.

The nonparametric Moore's paired test reveals significant difference or similitude between the fabrics (Table S12).

2.7. Radiocarbon dating

List of the samples used for ^{14}C dating, associated dates and biochemical parameters are presented in Table S13. Fragments of long mammal bones were selected to maximize the chances of collagen preservation. C-11 was a bulk sediment sample for which the alkali-insoluble organic matter (humin) fraction was extracted for ^{14}C dating.

2.8. Optically stimulated luminescence dating

The SAR protocol was adopted (Murray and Wintle, 2000, 2003; Wintle and Murray, 2006; details are given in Table S14). Note that this same protocol has been adopted for the Dose Recovery Tests experiments, with a given dose equal to the average equivalent dose measured during the preheat plateau tests, administrated after an internal bleach in the reader (two successive illuminations with OSL Blued LEDs during 100s separated by a 10 000 s pause).

Preheat plateau tests were conducted for 13 of the 16 samples and did not show significant variations in equivalent dose (D_e) values. These led us to choose the most adapted (i.e., the one where variations between aliquots are smallest) preheat temperature conditions for each case: either 200°C for 10s or 220°C for 10s. An example is given in Figure S16.

Dose recovery experiments (DRT) were conducted for 7 out of the 10 single-grain (SG)-dated samples. In all cases, the measured to given dose ratio was found to be consistent with unity, at 2 σ, under the chosen measurement conditions. For the SG-measured samples, the overdispersion (OD, as determined by the Central Age Model: CAM, Galbraith et al., 1999) measured for these DRT corresponds to the intrinsic overdispersion of each sample as defined by Thomsen et al. (2005). The values are reported in Table S15. For the three samples for which the DRT was not measured, the intrinsic overdispersion (σ_m) was taken as the mean value of the measurements conducted on the two closest samples (O-14 and O-15).

Equivalent doses (D_e), the number of selected grains (n) that passed all SAR protocol tests, as well as intrinsic (σ_m, from DRT measurements, Table S15) and extrinsic (σ_d, from Average Dose Model, ADM: Guérin et al., 2017) overdispersions, when relevant, are reported in Table S16 for multi-grain (MG)-dated samples and Table S17 for single-grain (SG)-dated samples.

A satisfactory number of aliquots or grains, after applying the quality criteria of the SAR protocol (recycling, recuperation and IR depletion ratios), was obtained for all samples (24 to 28 aliquots for MG-OSL, 137 to 443 grains for SG-OSL) except for three of them. In fact, for samples O-11, O-12 and O-2, a very low apparent equivalent dose (in the light of the Middle-Upper Palaeolithic nature of the deposits) appeared during the preheat plateau measurements. The measurements were not conducted further, and the D_e values and ages for these three samples are based on aliquots measured during preheat plateau test experiments. Consequently, the ages obtained in this way should be considered approximate ages.

All equivalent doses measured a range between *ca*. 39 and 68 Gy, except the three samples (O-2, O-11 and O-12), which have values in the order of a few Gy, or even a fraction of a Gy. The Abanico plots of the SG-dated samples are presented in Figure S17 (A and B). The distributions, in agreement with the extrinsic (σ_d) values (reported in Table S17), do not lead to any suspicion of incomplete bleaching. Only one sample, O-5, may present a bimodal distribution (with the lowest distribution presenting many more grains than the highest), which may be explained as the result of the mixing of two different quartz grain populations with different taphonomic histories and different times of last exposure to sunlight. The Average Dose Model (ADM, see Guérin et al., 2017) was applied to all samples, and the corresponding D_e are presented in Tables S16 and S17, even for sample O-5. We decided to also apply the Finite Mixture Model (FMM, Galbraith and Green, 1990) to this sample; we obtained a two-component distribution, with sigma b=0.09: the first component (more abundant) corresponds to 82.5% of the grains and leads to a D_e of 41.8 +/- 0.6 Gy; the second component corresponds to 17.5% of the grains and leads to a D_e of 84.4 +/- 3.2. We then retained the more abundant fraction, which corresponds to the lowest D_e value (in turn, the more recent bleaching event) to estimate the age of the last exposure of these quartz grains to sunlight. We chose to consider this value in the discussion, even if ages determined with FMM have to be considered with caution (Guérin et al., 2017). We consider this estimation of the age as the best estimation at this point, but this age as to be considered as less relevant than the ages obtained for other samples of the site. Following this logic that FMM-ages are not fully reliable because of dose rate issues, we did not try to optimize the sigma-b value used as input to run the FMM, because such a parameter tuning would not resolve the main problem of calculating an OSL age with the FMM.

A combination of measurements was used to determine the different contributions to the dose rate. The radioelement concentrations of the samples are presented in Table S18. They do not present significant disequilibrium in the U-series, except for sample O-6 (Figure S18). No systematic effect is detected (Guibert et al., 2009), so we chose to consider the U(^{226}Ra) value as being the most representative of the U-series contribution to the dose rate since approximately 90% of the alpha and beta dose rates are contributed by the radioelements of this part of the U chain (Aitken, 1998).

The environmental dose rates, either measured (with Al_2O_3:C dosimeters) or calculated (in the three cases for which dosimeters were not inserted), are reported in Table S18, as well as the total dose rate considered for each sample. In the case of sample O-16, taken from a sedimentary infill within the mushroom farm, the environmental contribution to the dose-rate is questionable. In fact, it was not possible to insert a dosimeter in correspondence to the sampling point, and the shape and depth of the sedimentary infill is unknown. We prepared and measured two sub-samples extracted from this sample: i) a sub-sample containing a representative fraction of all components initially present in the sample; its KUTh contents were used to calculate

the gamma contribution to the dose rate; ii) a sub-sample containing a representative fraction of all components <2 mm in size initially present in the sample; its KUTh contents was used to calculate the beta contribution to the dose rate. Even having taken this precaution, our gamma dose rate estimate may be overestimated (and the age underestimated) since this is equivalent to considering that the sample was surrounded by tens of centimetres of the sampled sediment in all directions, whereas bedrock was clearly visible around the sampled sediment.

2.9. Spatial analysis

The spatial analysis of the distribution of faunal and lithic remains from the Lévêque's excavations was carried out using ArcMap (Esri) software with the Spatial Analyst module. The analysis of the density of the archaeological remains was carried out according to the Kernel density estimation. The latter is based on a population sample and makes it possible to estimate the density at any point in the study area. We retained the choice of the planar distance between the entities because this method is well suited to an analysis at the local scale. The results were mapped into 10 classes, with subgrouping according to the Jenks natural breaks method. The study of the point statistics on the corrected Z corresponds to the calculation of the average of the values of the field according to a circular neighbourhood and the unit of the map (metre). The result is represented on a map in 5 classes, with a discretization according to the method of natural thresholds of Jenks. Hot spot analysis is a tool that identifies statistically significant spatial clusters of high values (hot spots) and low values (cold spots) using the Getis-Ord Gi* over Z statistical tool. For the calculation, a constant distance channel (default option) was chosen as well as a calculation mode according to the Euclidean distance. As for the previous analyses, the results were mapped using 5 classes according to the method of natural thresholds. We also performed an optimized hot spot analysis. This tool identifies statistically significant hot spots and cold spots corrected for multiple testing and spatial dependence using the False Discovery Rate (FDR) correction method. Features with a Gi-Bin value between +/- 3 are statistically significant with a 99% confidence level. Those whose value varies between +/- 2 have a confidence level of 95%. Entities between +/- 1 have a confidence level of 90%. Those whose Gi-Bin value is equal to 0 are not statistically significant.

Figure S19 displays the density map, Z-mean and hot spot analysis revealing the spatial distribution of faunal and lithic remains from Lévêque's excavations. These results must be compared to the dome-shaped morphology of the sequence, field observations (Figures S11 and S12; Figure 4, main text), fabric analysis (Figure 13, main text), in the light of possible site formation processes (Figure S13), in order to appreciate the geomorphological genetic model (Figures 16 and 17, main text).

3. Supplementary figures

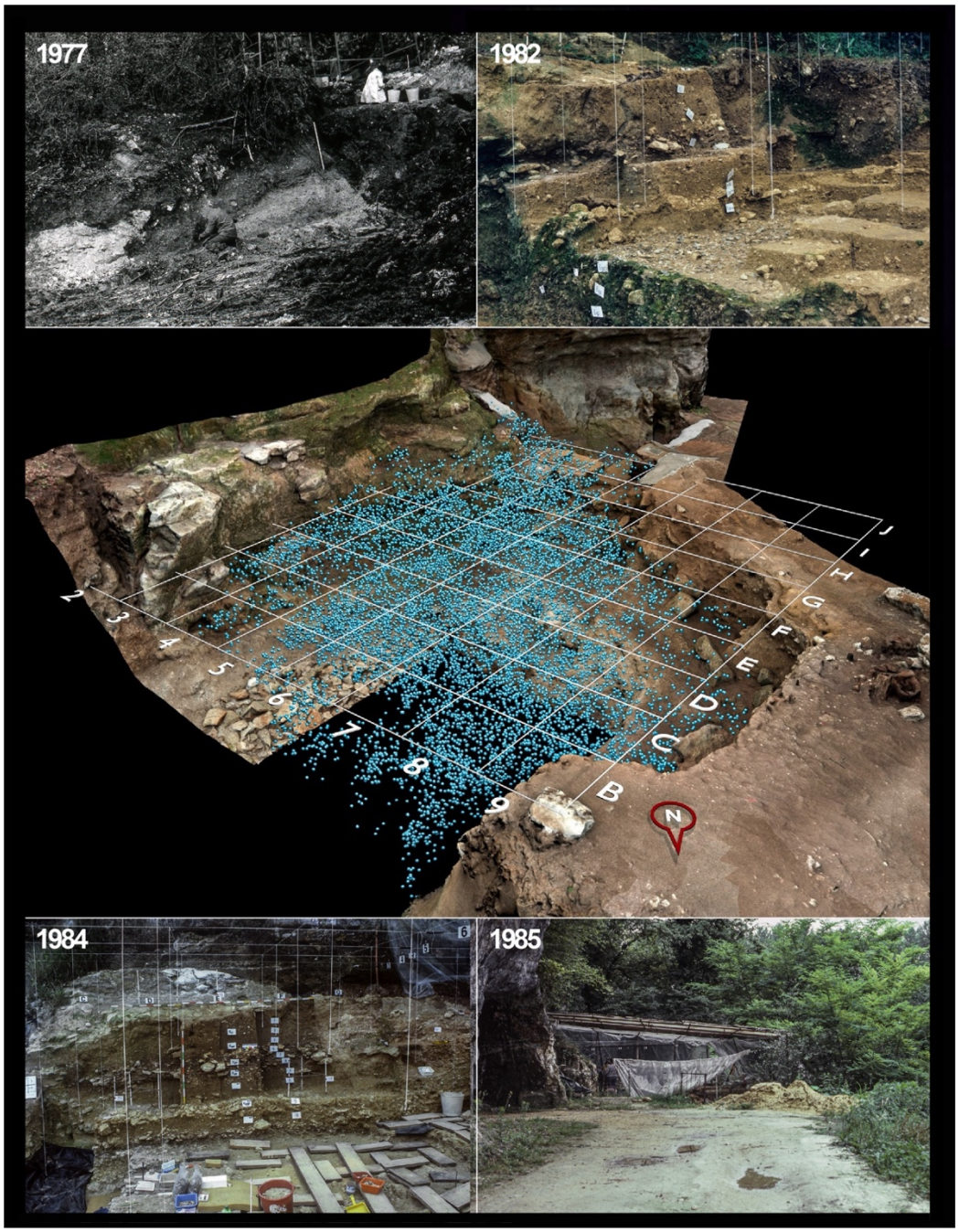

SOM Figure S1. Archival data illustrating the evolution of Levêque's excavation between 1977 and 1985 along with a three-dimensional model showing the projection of all the artefacts recorded during Lévêque's excavations (blue dots).

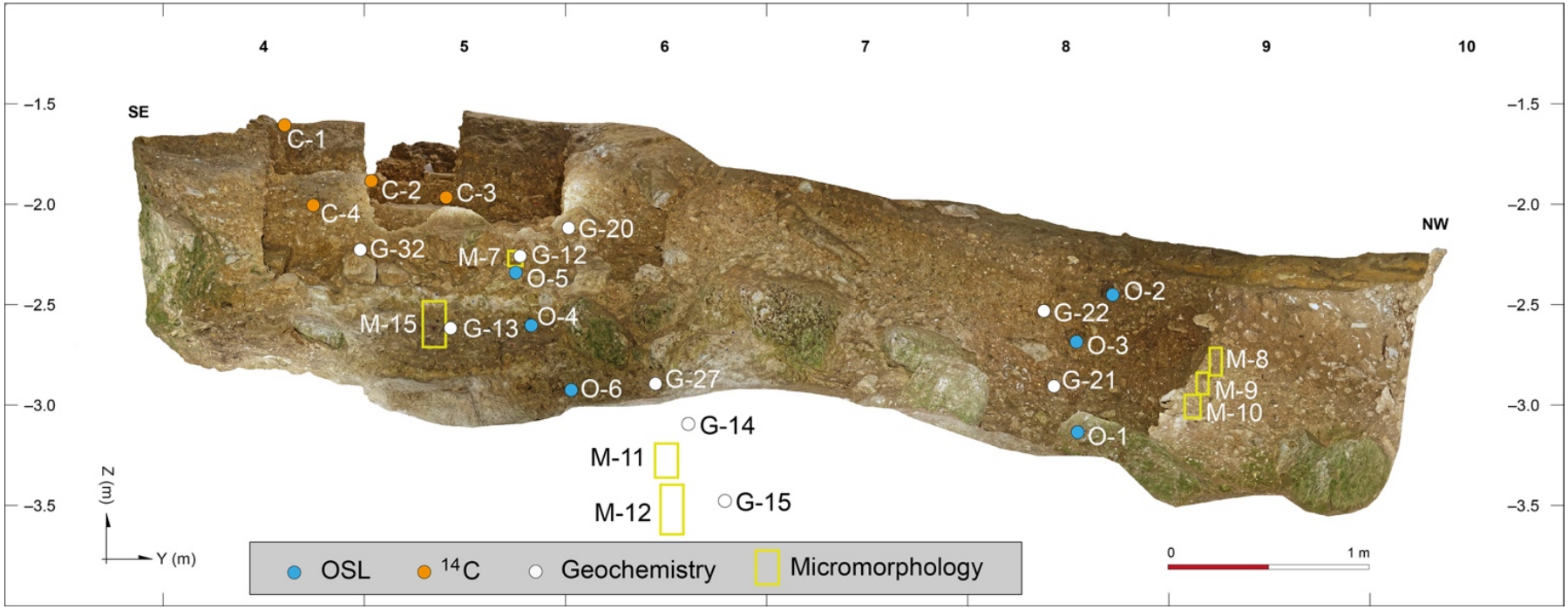

SOM Figure S2. Orthophotograph of the main sagittal section (*cf.* Figure 3, main text) showing the position of the micromorphology (M), geochemistry (G), OSL (O) and radiocarbon (C) samples.

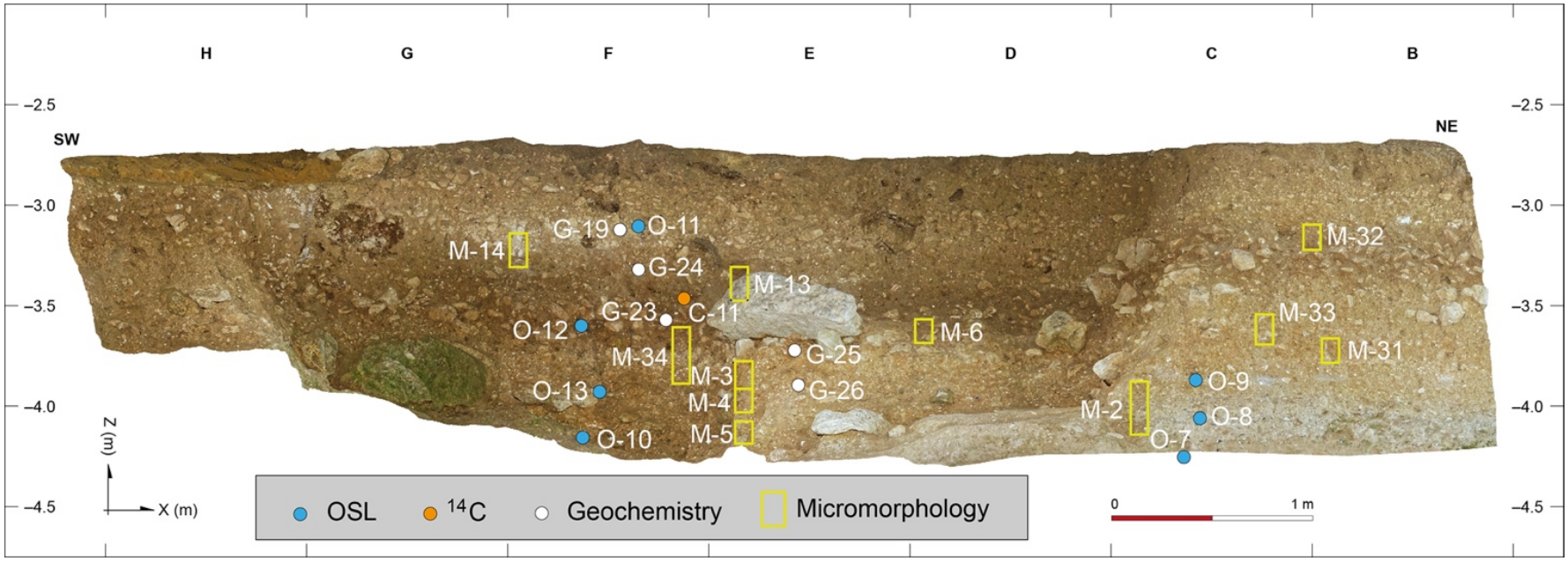

SOM Figure S3. Orthophotograph of the main frontal section (*cf.* Figure 3, main text) showing the position of the micromorphology (M), geochemistry (G), OSL (O) and radiocarbon (C) samples.

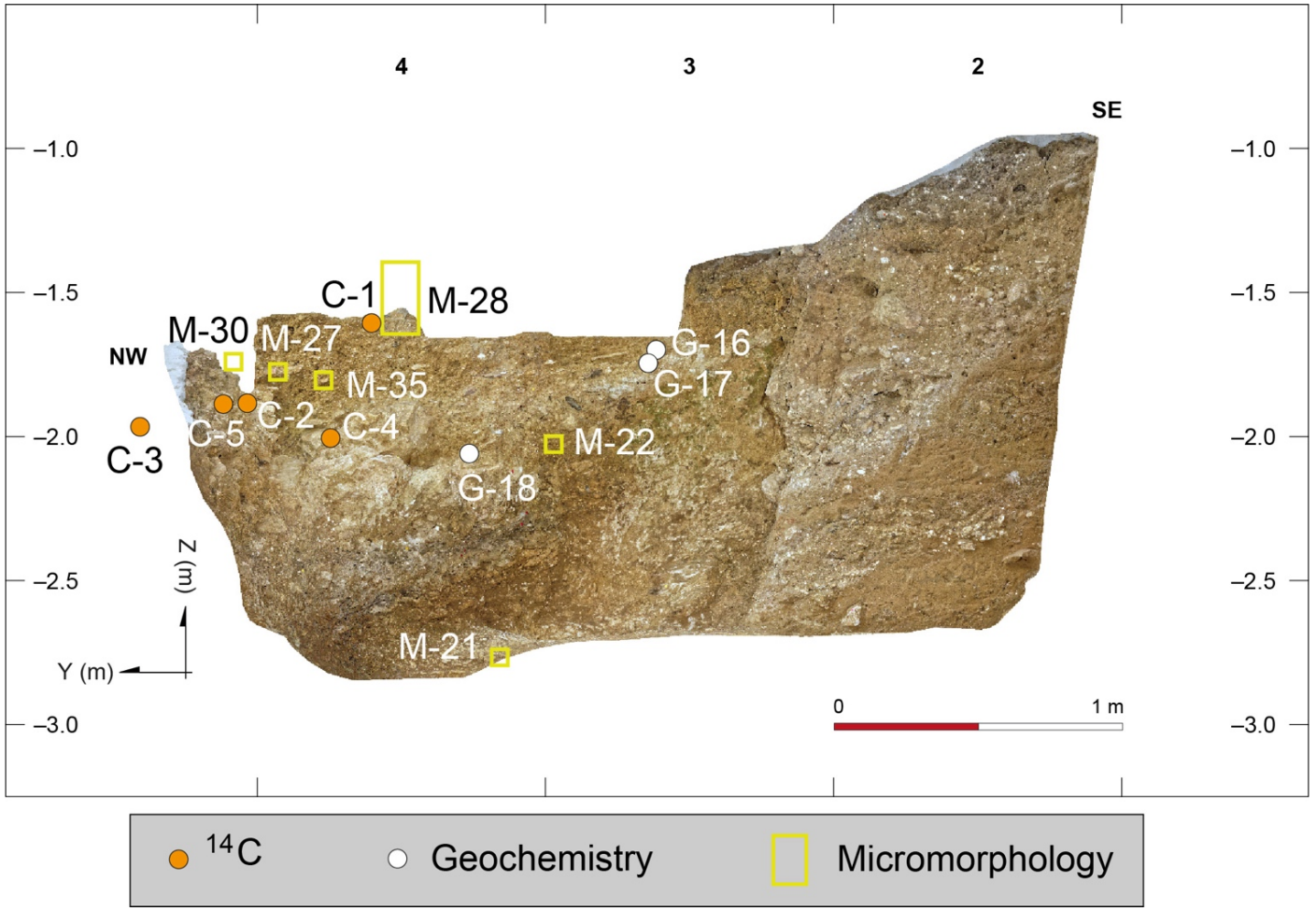

SOM Figure S4. Orthophotograph of the JKLM sagittal section (*cf.* Figure 3, main text) showing the position of the micromorphology (M), geochemistry (G), OSL (O) and radiocarbon (C) samples.

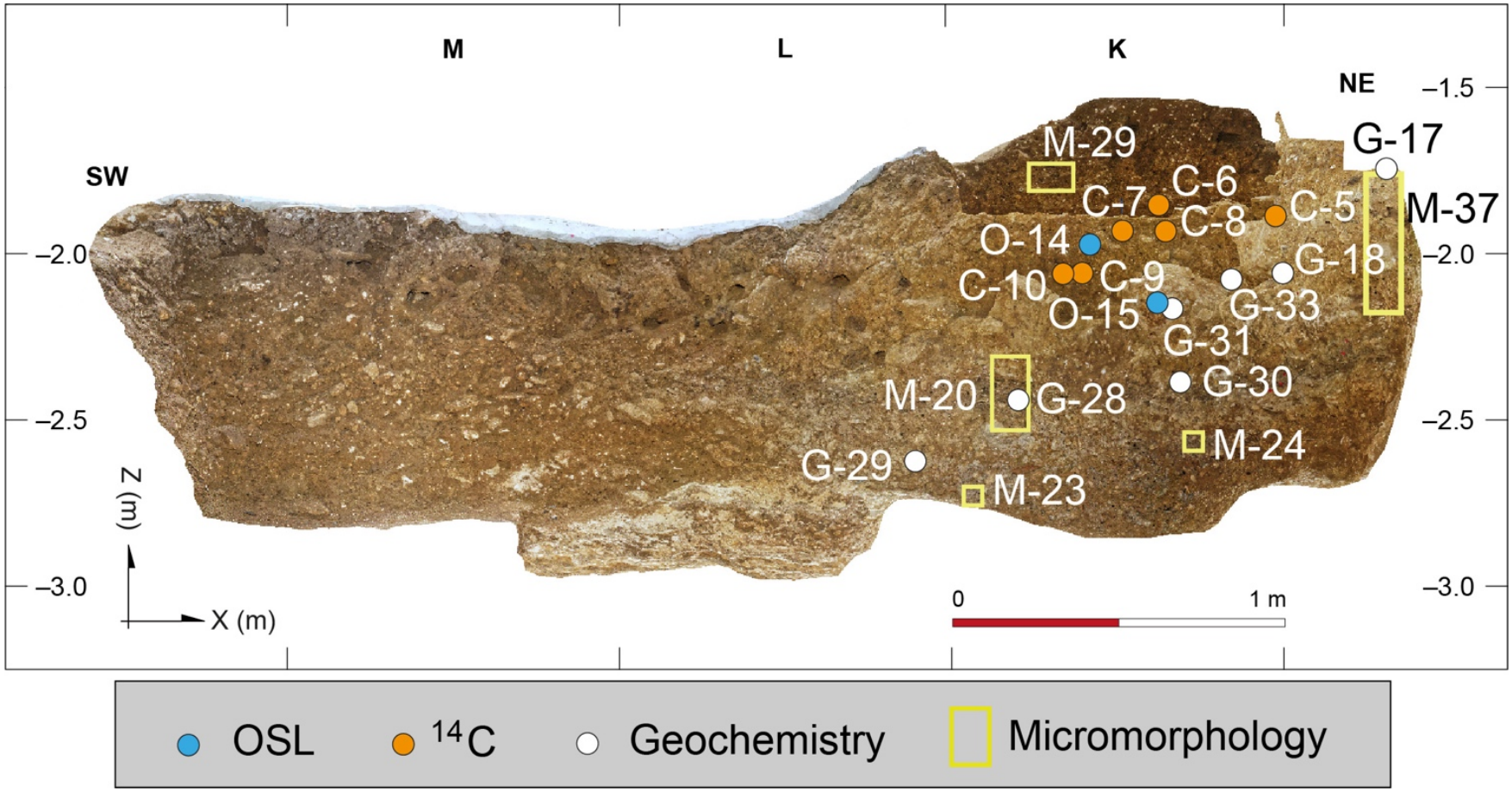

SOM Figure S5. Orthophotograph of the JKLM frontal section (*cf.* Figure 3, main text) showing the position of the micromorphology (M), geochemistry (G), OSL (O) and radiocarbon (C) samples.

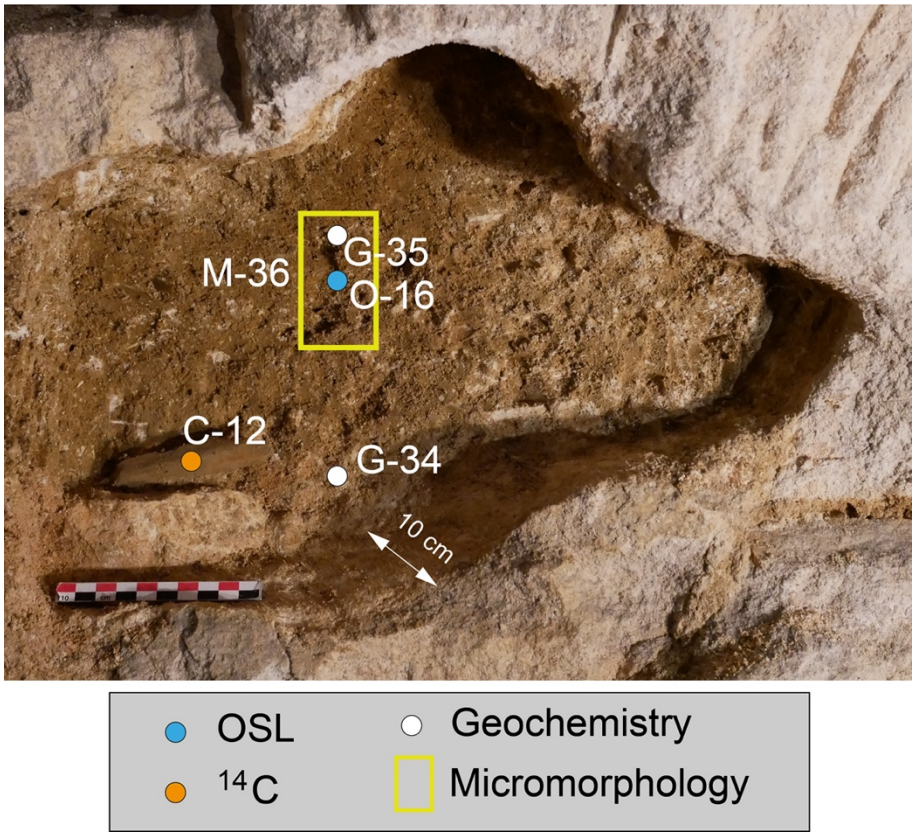

SOM Figure S6. Photograph of the sedimentary deposit in square J100 on the northern wall of the mushroom farm behind the site (*cf*. Figure 3, main text) showing the position of the micromorphology (M), geochemistry (G), OSL (O) and radiocarbon (C) samples.

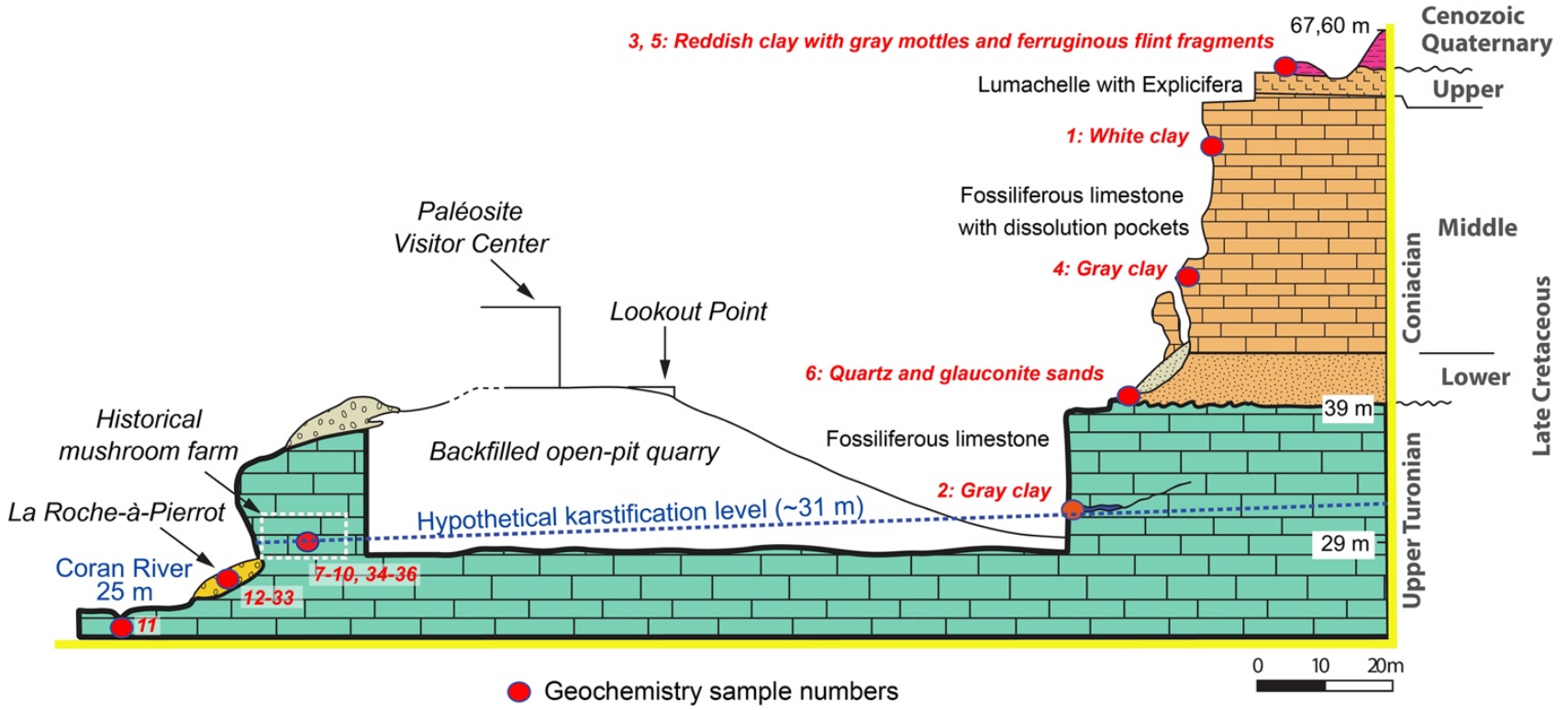

SOM Figure S7. View of the open-pit limestone quarry indicating the provenience of the geochemistry samples (G; red dots; see Table S1). The position of the hypothetical karstification level is indicated (ghost-rock weathering). Local karstic evolution is likely related to the incision of the Coran River, a process possibly repeated at other points along the Turonian cliff, including the mushroom farm behind the site (6 m above the current Coran floodplain). This is suggested by incipient karstic features observed in the mushroom farm chambers and in the open-pit quarry.

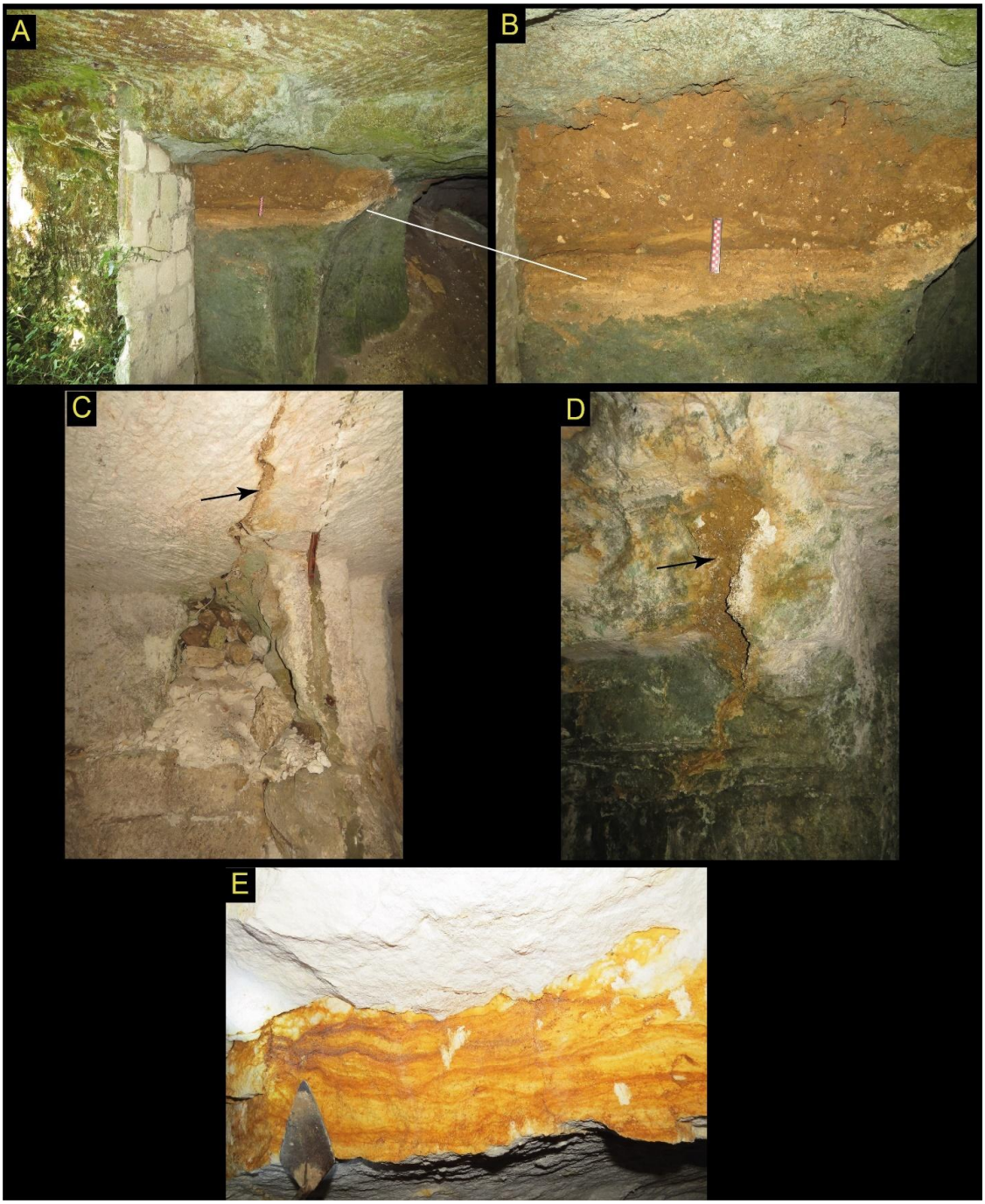

SOM Figure S8. Examples of karst features observed in the mushroom farm/historical quarry behind the site: A, B) Man-truncated, infilled (plurimetric) alveolus (large pocket) at the quarry entrance, connected to the surface and receiving allochthonous material; C) Dissolution fissure aligned with the axis of the diaclase adjoining the JKLM zone; D) Small vertical dissolution feature; E) Liesegang bands. The alterites from dissolution features (C and D) were sampled for XRD and element analyses.

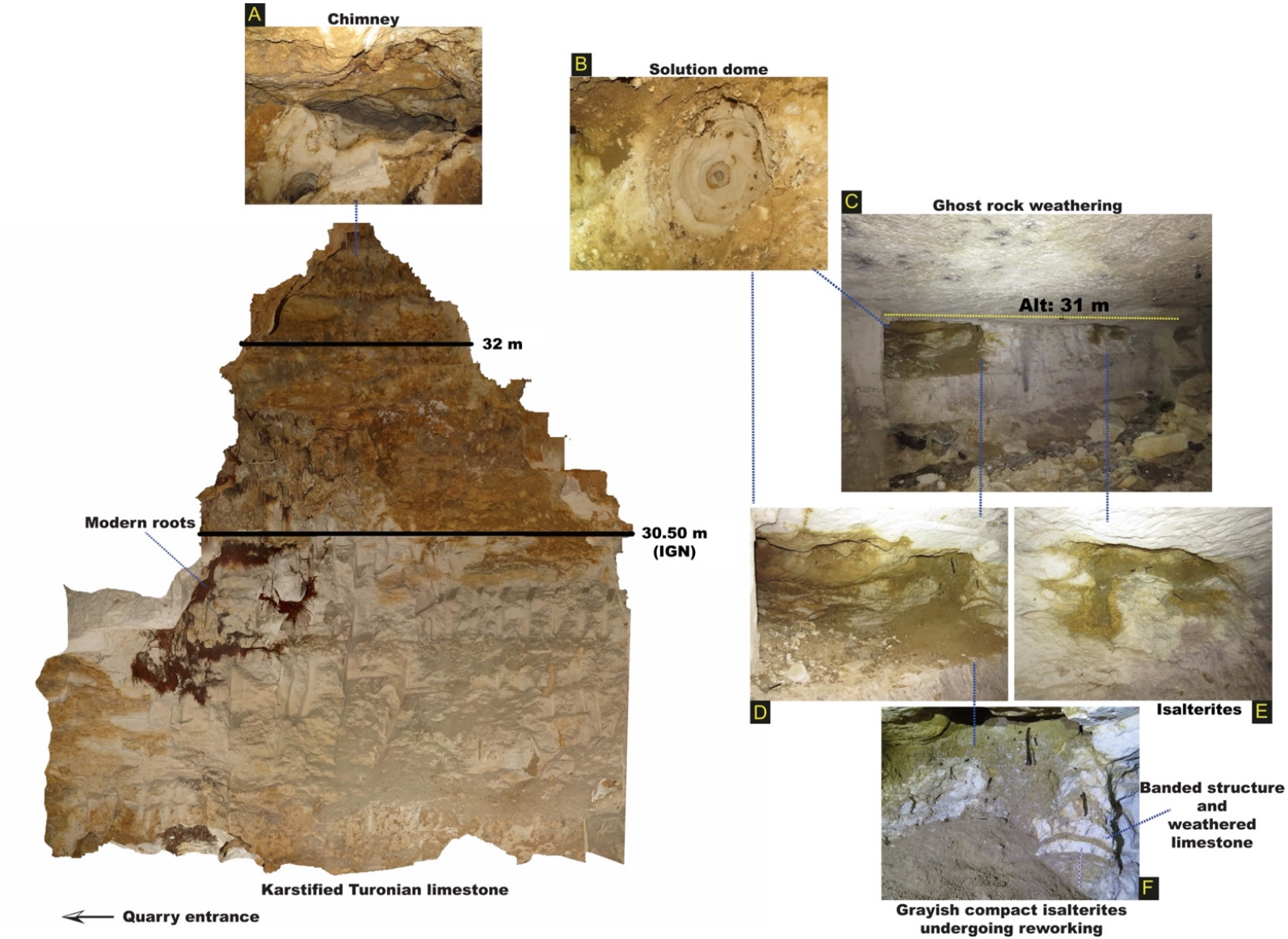

SOM Figure S9. Other examples of karst features observed in the Upper Turonian limestone in the small historical quarry/mushroom farm directly adjoining the site: A) Chimney; B) Solution dome; C) Level of ghost-rock weathering (around 31 m above sea level); D to F) Grayish alterites (isalterites). The latter were sampled for XRD and element analyses. IGN = National Institute of Geographic and Forest Information.

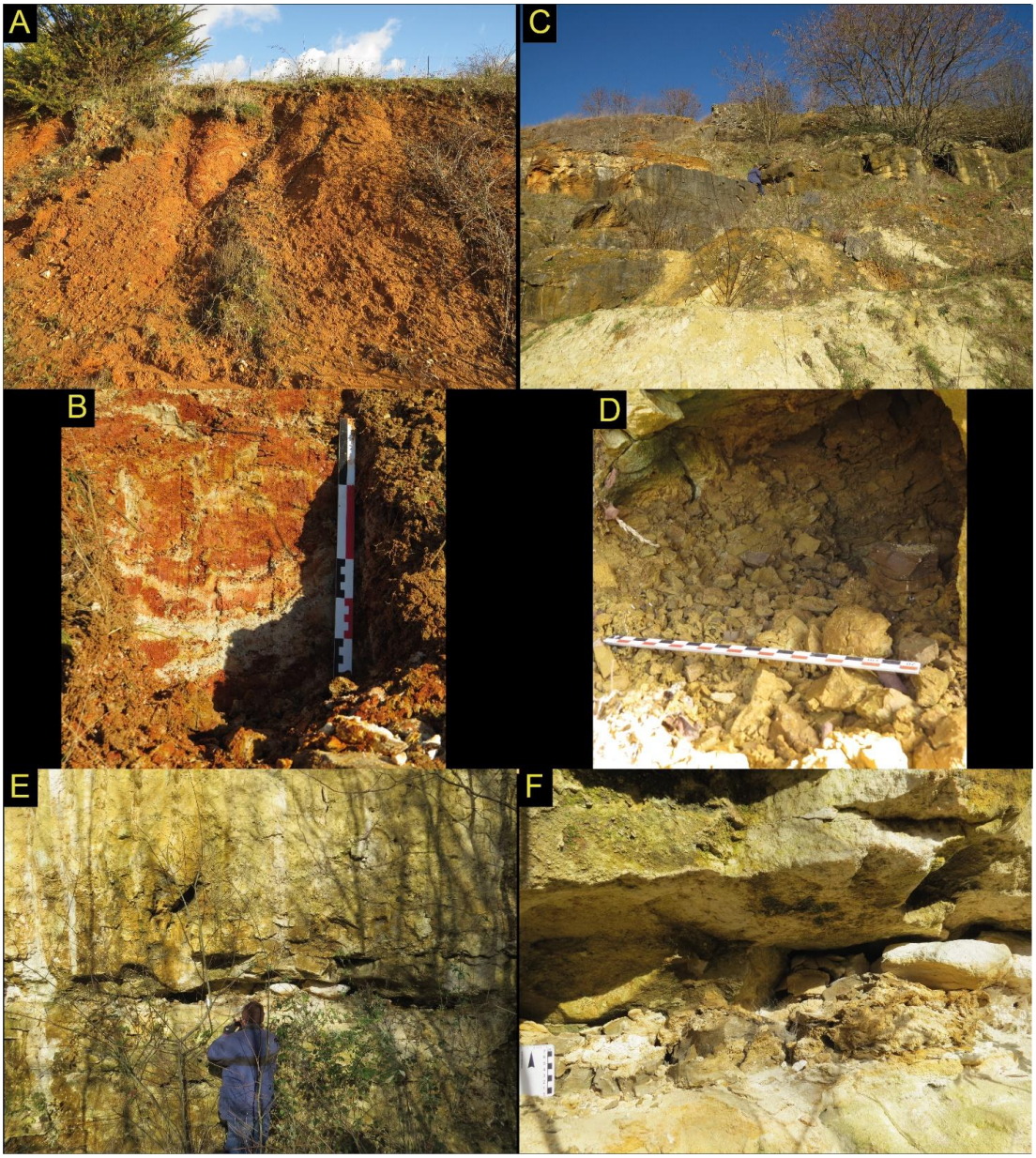

SOM Figure S10. Off-site features at the open-pit quarry: A and B) Reddish clays with flint and mottling at the top of the quarry (top of the Cretaceous plateau); C) Karstified Middle Coniacian limestone above Lower Coniacian quartz and glauconite sand bed; D) Grayish clayey alterites (isalterites) associated with Middle Coniacian limestone; E) Level of ghost-rock karstification in the Upper Turonian limestone; F) Close-up view of grayish clayey alterites. These formations were sampled for XRD and elemental analyses (see Table S1; Figure S7).

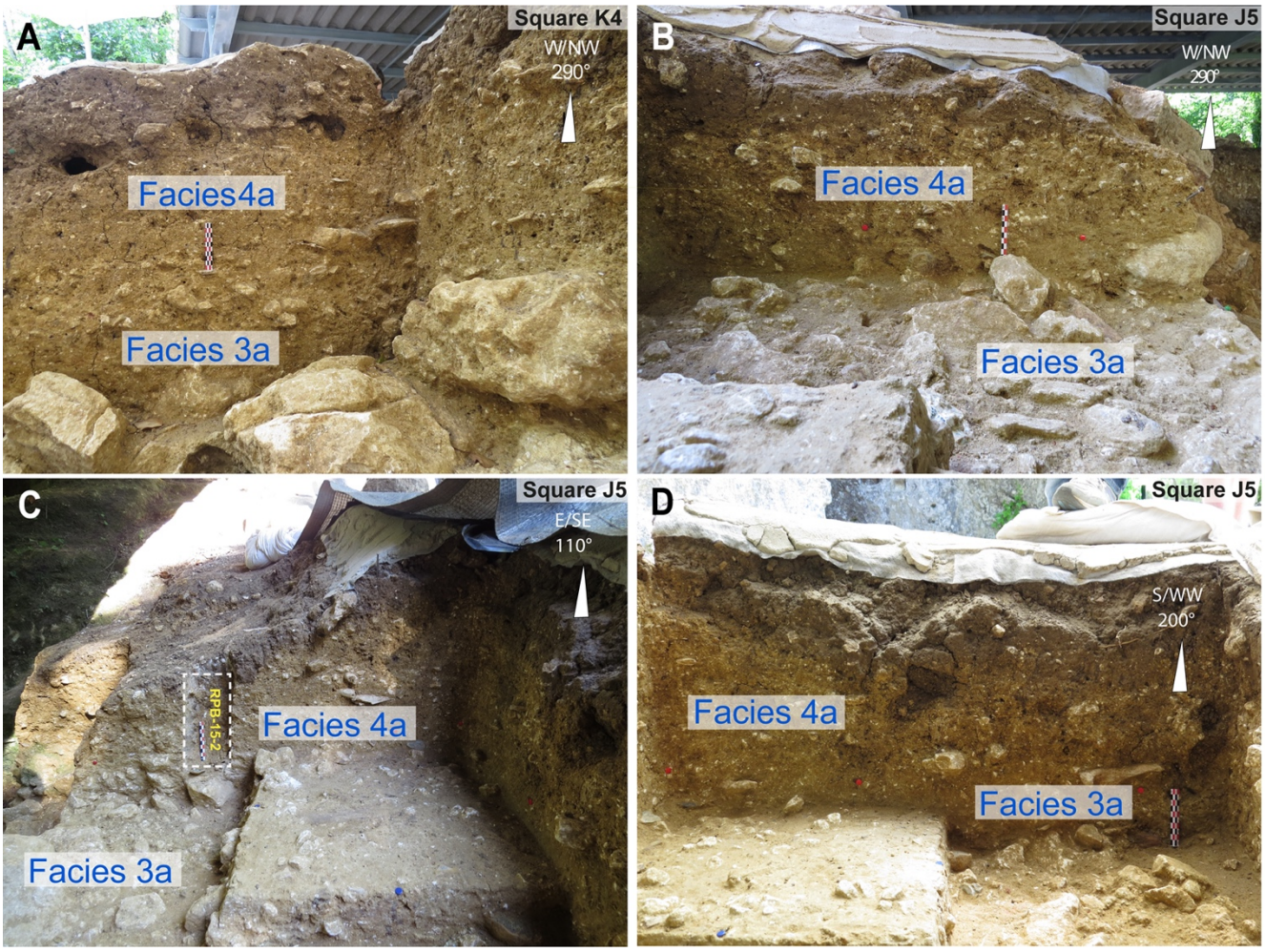

SOM Figure S11. Diamictic macrofacies 3a and 4a observed in squares K4 and J5 during excavation. Note the crude stratification of the deposits. RPB-15-2 = micromorphology sample.

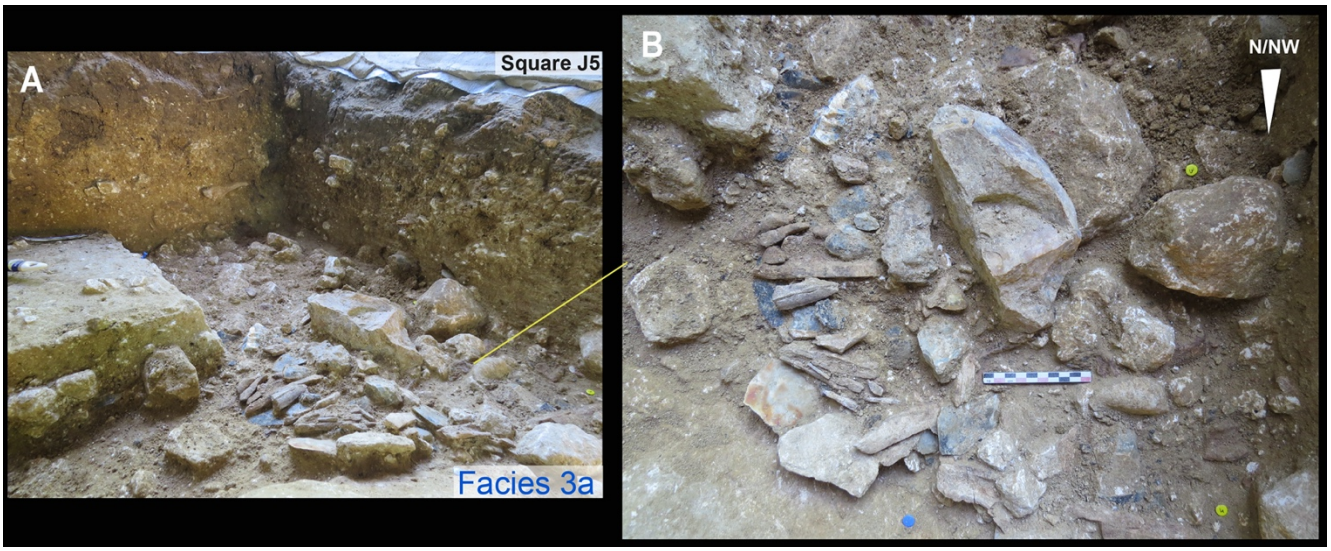

SOM Figure S12. Field view of diamictic Facies 3a in square J5 during excavation. Note the lobate morphology with imbricated archaeological remains.

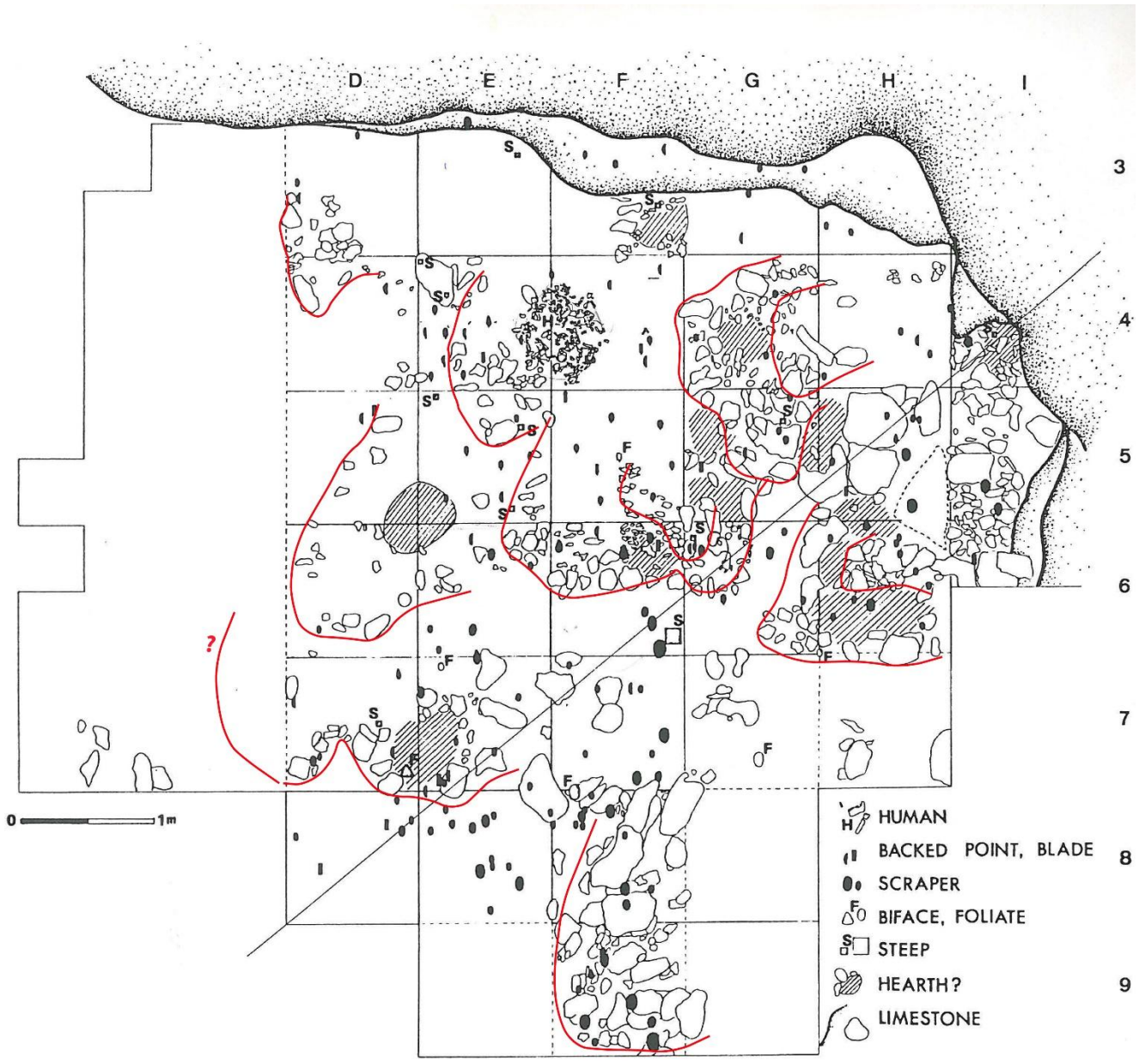

SOM Figure S13. Genetic reinterpretation of level EJOP from Levêque's excavation as initially described by Backer (1993). Possible solifluction features in the form of small-sized lobes are indicated (in red) suggesting slow downslope reworking of archaeological remains, limestone clasts and fine-grained sediments (derived from alterites/surficial formations) in a periglacial environment.

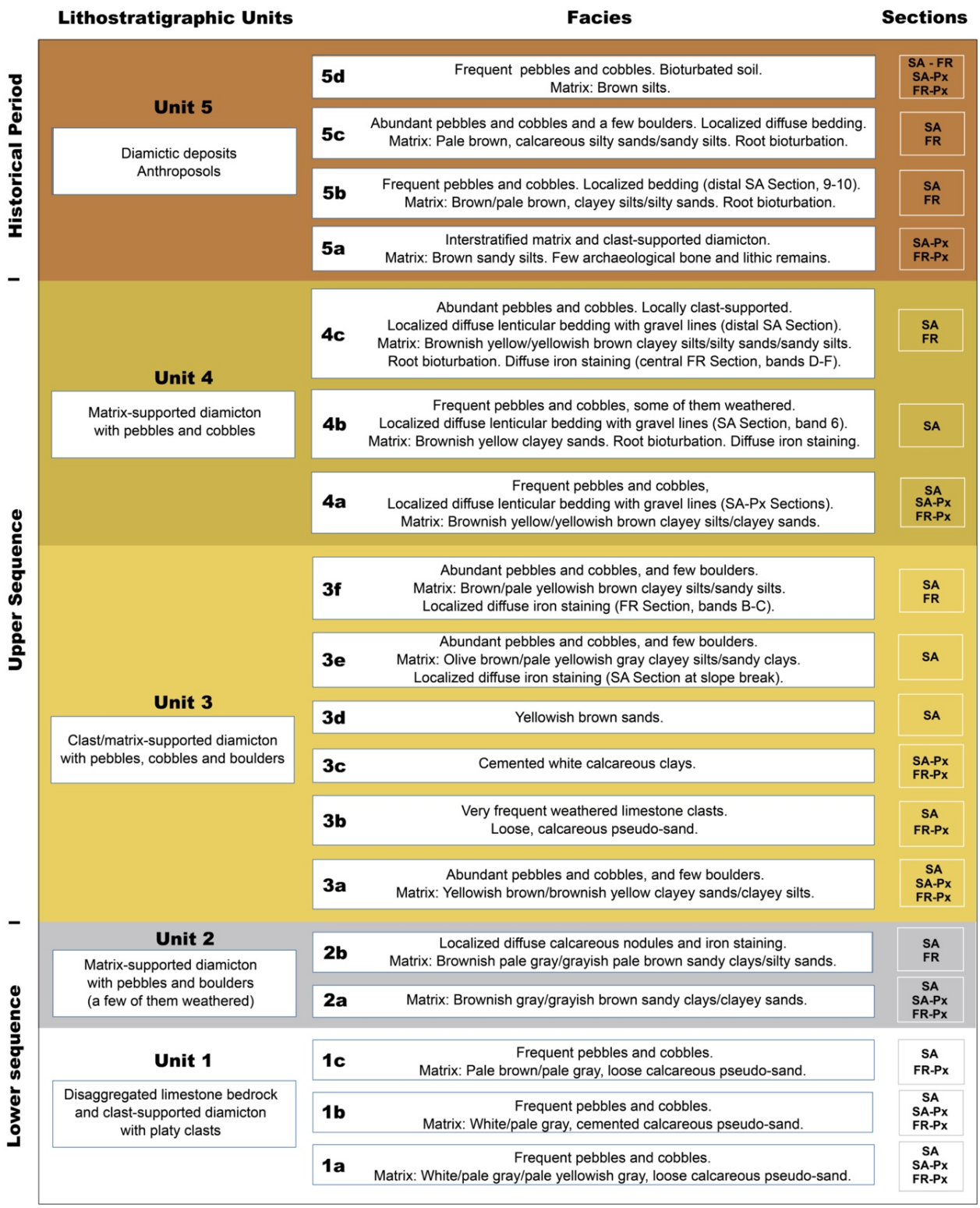

SOM Figure S14. Lithostratigraphic matrix with field descriptions of the units and subunits (facies) and their representation across the sections. SA = Sagittal, FR = Frontal, Px = Proximal.

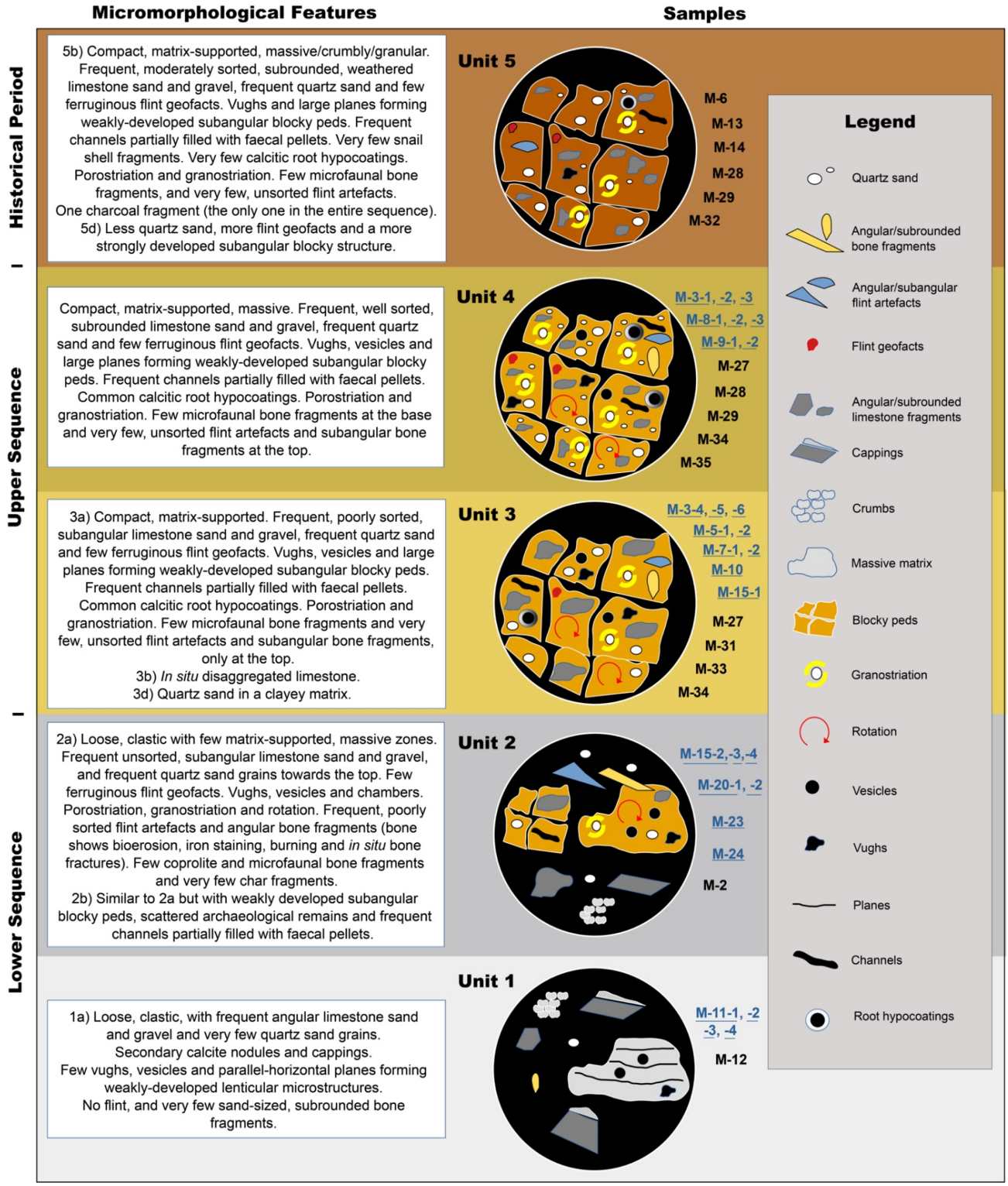

SOM Figure S15. Summarized micromorphological descriptions, sample provenience and schematic representations of the main features. High-resolution scans of selected thin sections (with blue underlined sample labels) are provided by clicking on the hyperlinks in Table S8.

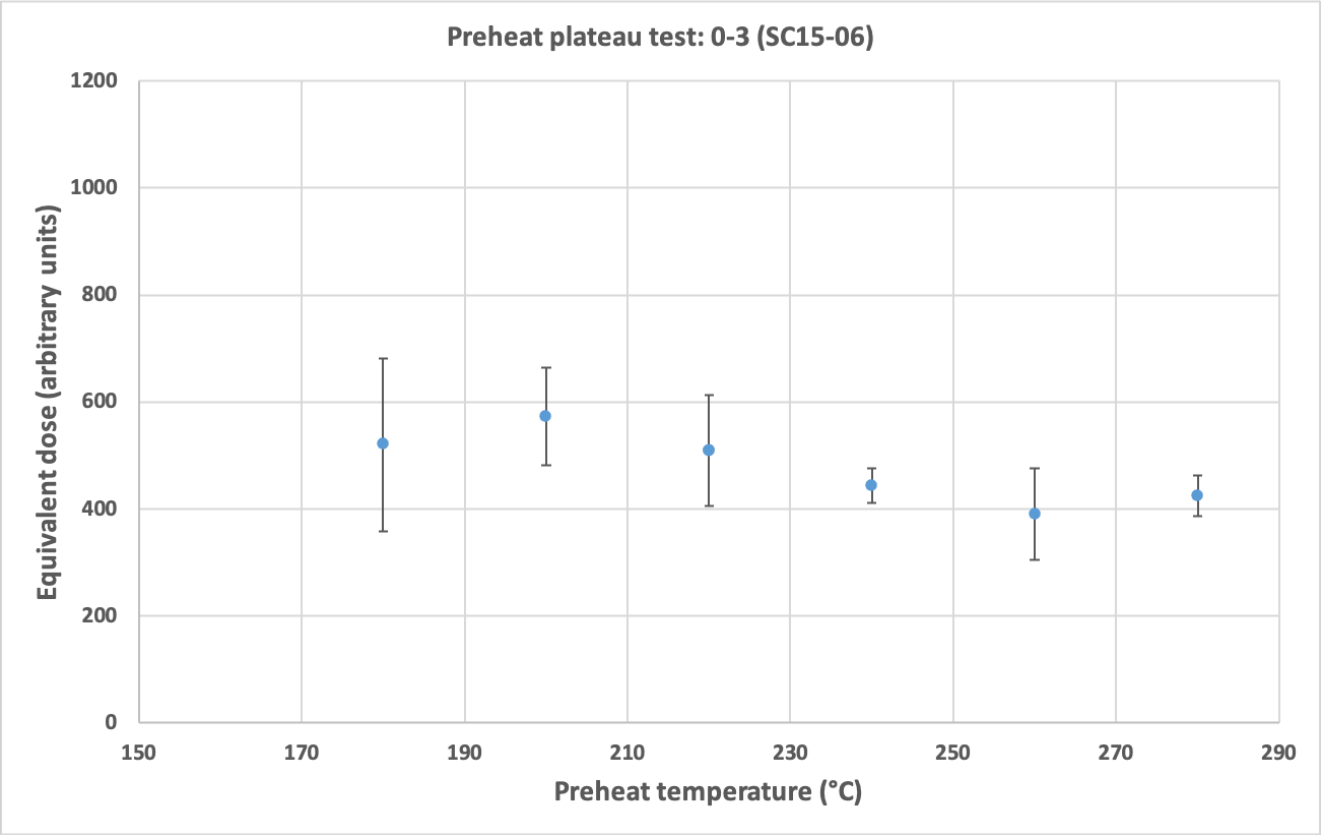

SOM Figure S16. Results of the preheat plateau test conducted on sample O-3 (SC15-06). Vertical error bars = standard deviation (SD).

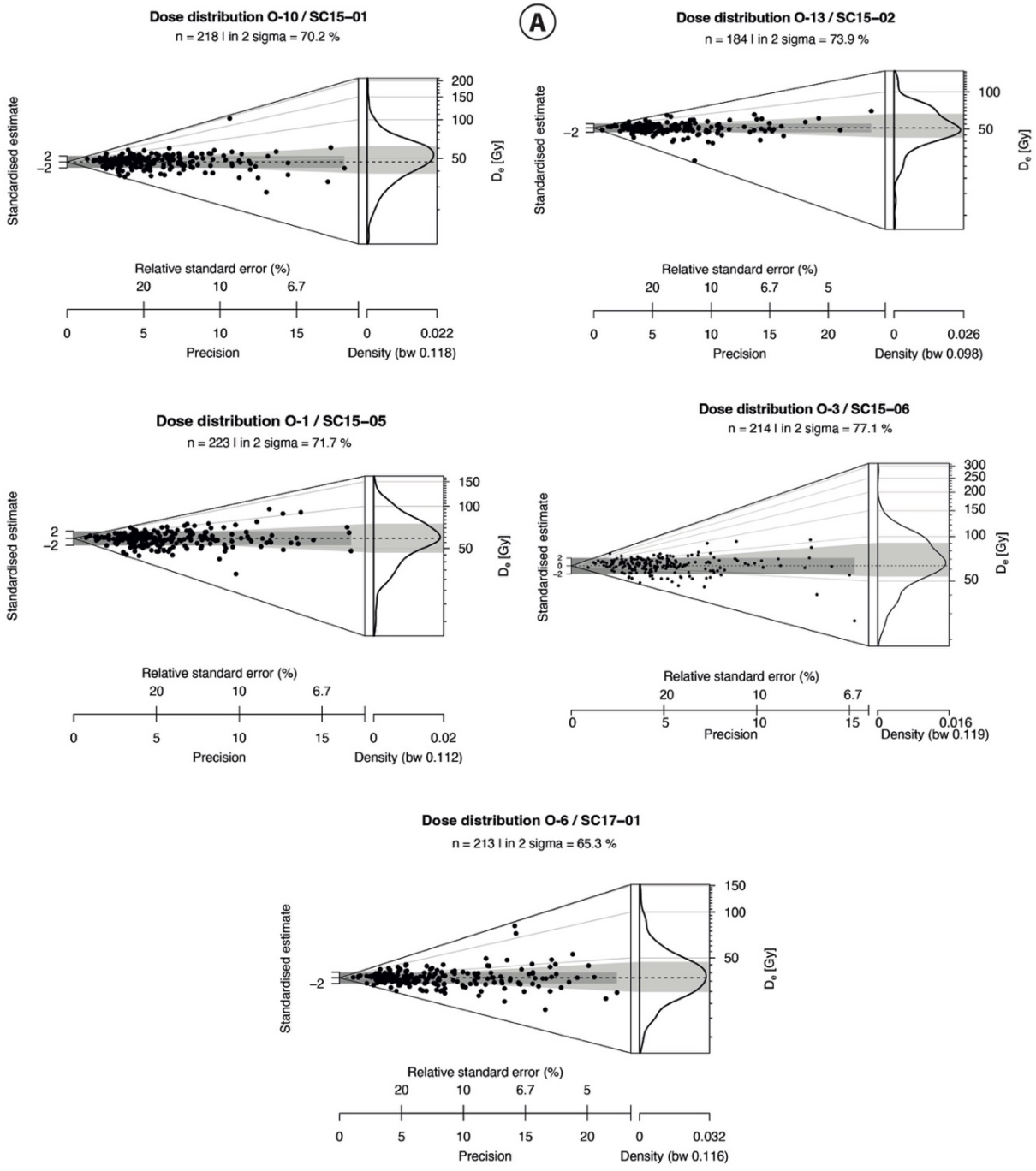

SOM Figure S17 (A). D_e distributions for the SG-OSL dated samples (Abanico Plots - R Development Core Team, 2015, package 'Luminescence' version 0.4.6; Kreutzer et al., 2012; Dietze et al., 2016). The dark-shaded band corresponds to ± two standard errors of the mean; the polygon in lighter gray indicates the area between the first and third quartiles of individual D_e values.

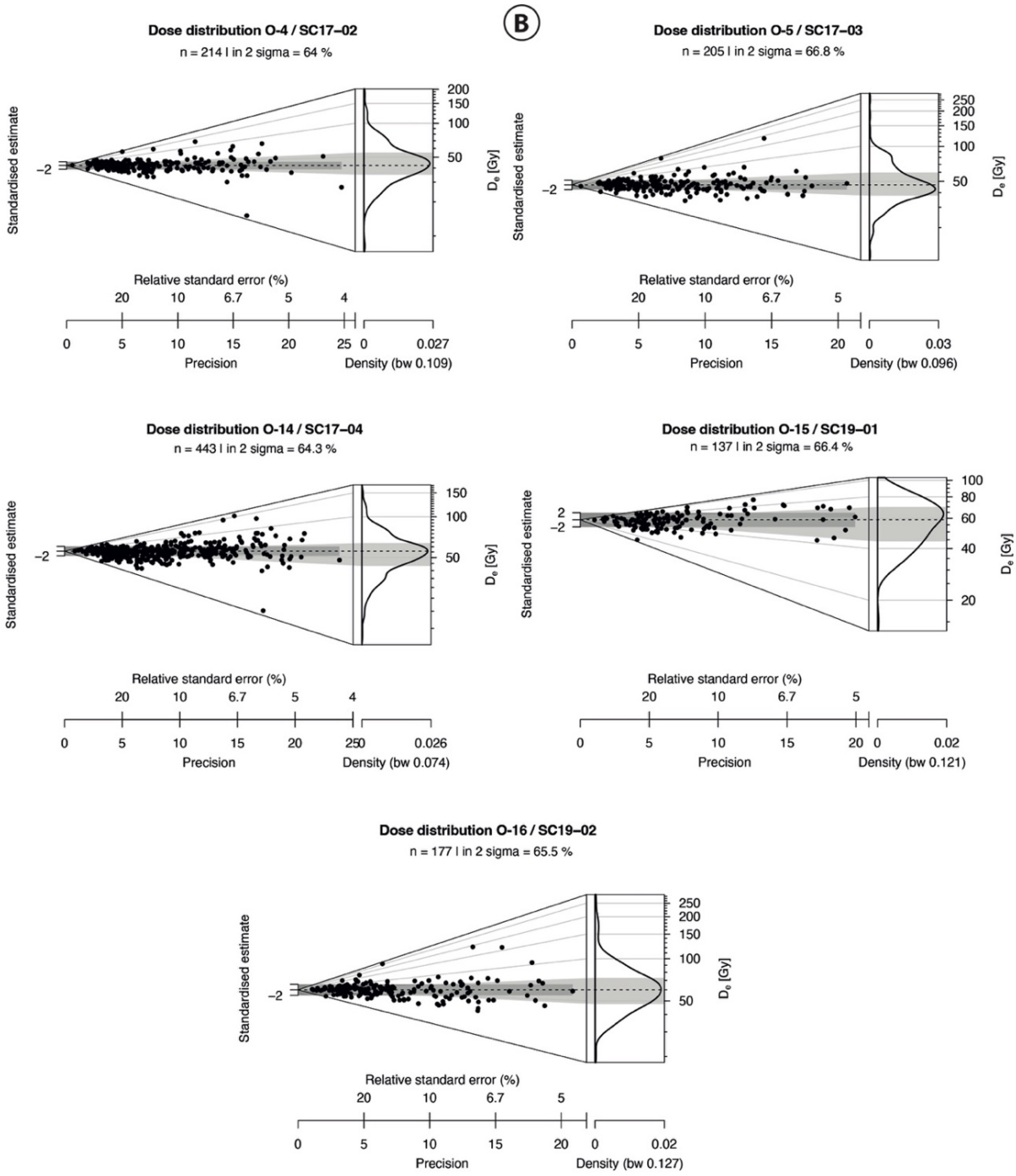

SOM Figure S17 (B). (Continued).

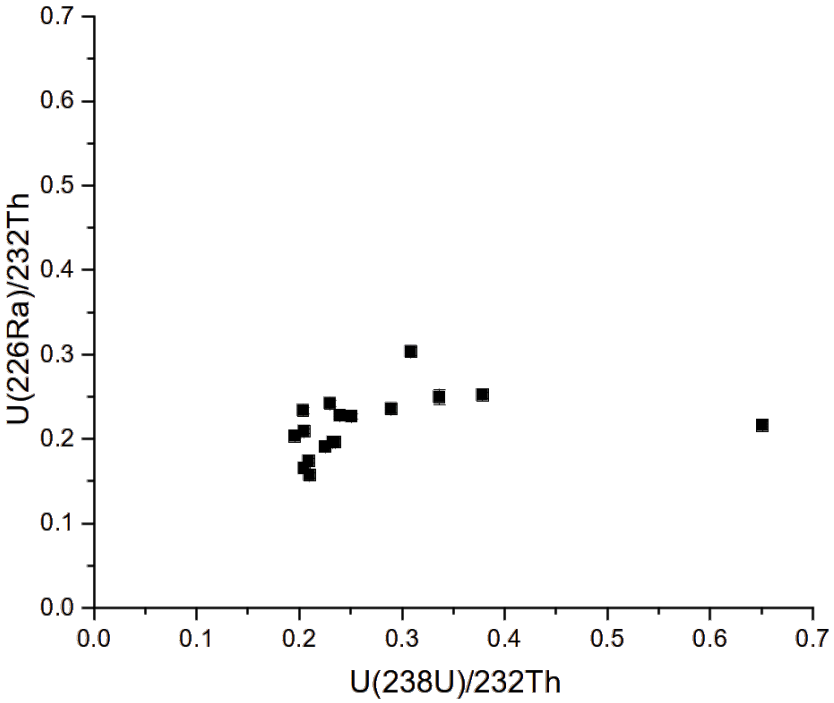

SOM Figure S18. Graph showing the U-series equilibrium state in the sediment samples. Radioelement contents were measured using a high-purity low-background Germanium gamma-spectrometer at the Bordeaux Luminescence Laboratory (IRAMAT-CRP2A).

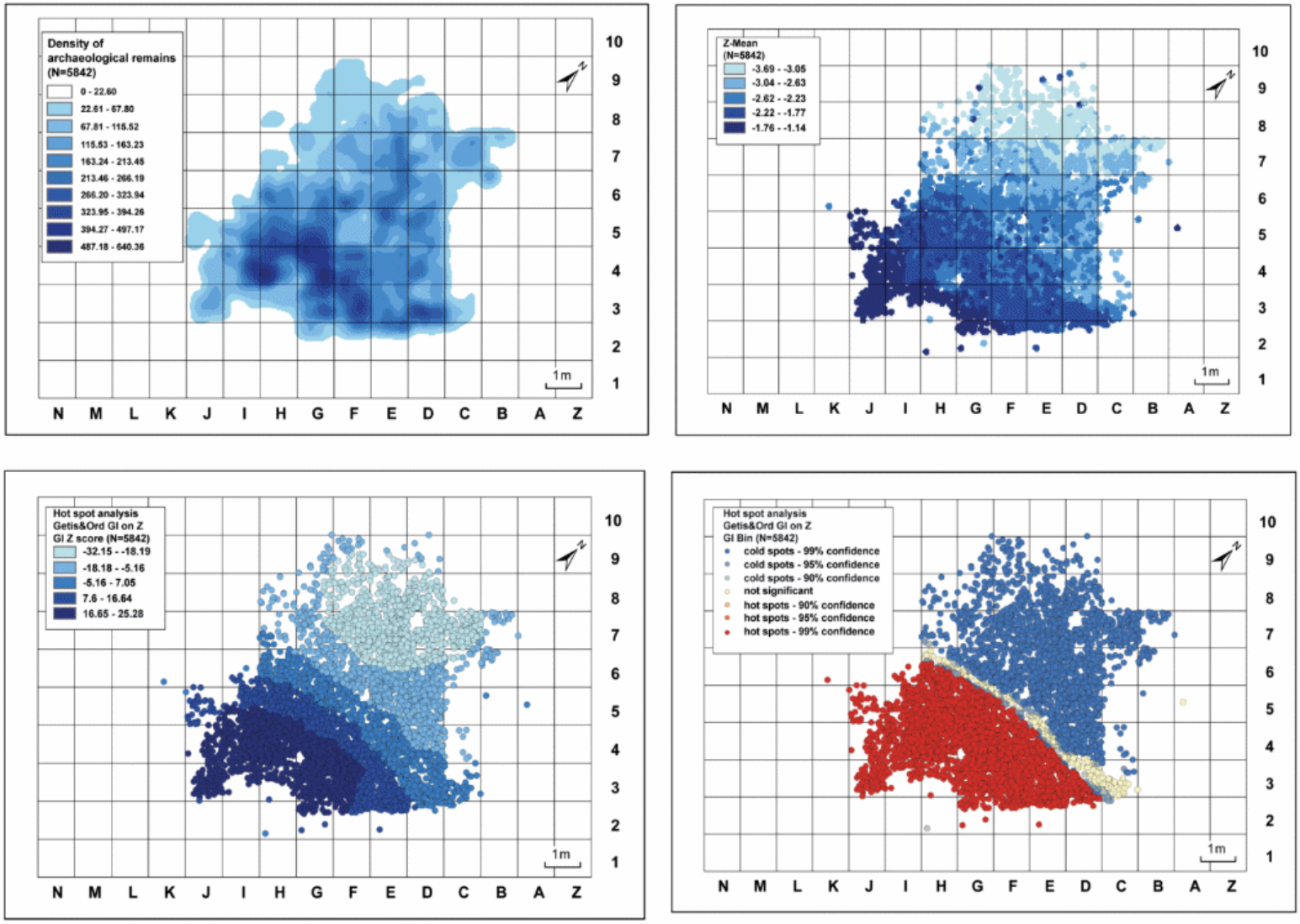

SOM Figure S19. Density map, Z-mean and hot spot analysis plots showing the spatial distribution of faunal and lithic remains from Lévêque's excavations. Analysis performed using ArcMap (Esri) software with the Spatial Analyst module.

4. Supplementary tables

SOM Table S1. Provenience of the intra-, peri- and off-site bulk sediment samples used for geochemistry (G). ID = numbers referenced in Figures S2-S7 and in PCA biplots (Figures 9A-B-C, main text).

ID	Section / Provenience/ Description of bulk sediment samples
G-1	Open-pit quarry (Paléosite): whitish alterites derived from Coniacian limestone
G-2	Open-pit quarry (Paléosite): grayish alterites derived from Turonian limestone
G-3	Open-pit quarry (Paléosite): reddish alterites with grayish mottling (clay with flint)
G-4	Open-pit quarry (Paléosite): grayish alterites derived from Coniacian limestone
G-5	Open-pit quarry (Paléosite): reddish alterites with grayish mottling (clay with flint)
G-6	Open-pit quarry (Paléosite): Coniacian quartz and glauconous sands
G-7	Mushroom farm adjacent to the site: grayish alterites (chimney)
G-8	Mushroom farm adjacent to the site: alterites (alteration feature)
G-9	Dissolution fissure in the axis of the diaclase adjacent to the JKLM area: alterites
G-10	Mushroom farm adjacent to the site: grayish alterites (chimney, *ca.* 29 m asl)
G-11	Coran River fluvial sands (modern stream bed medium sand)
G-12	Palaeolithic sequence: sagittal section
G-13	Palaeolithic sequence: sagittal section
G-14	Palaeolithic sequence: bedrock-derived sediment (facing the base of main sagittal section)
G-15	Palaeolithic sequence: bedrock-derived sediment (facing the base of main sagittal section)
G-16	Palaeolithic sequence: JKLM proximal zone
G-17	Palaeolithic sequence: JKLM proximal zone
G-18	Palaeolithic sequence: JKLM proximal zone
G-19	Palaeolithic sequence: frontal section

G-20	Palaeolithic sequence: sagittal section
G-21	Palaeolithic sequence: sagittal section
G-22	Palaeolithic sequence: sagittal section
G-23	Intra-site anthropoturbated historical deposits: frontal section
G-24	Intra-site anthropoturbated historical deposits: frontal section
G-25	Palaeolithic sequence: frontal section
G-26	Palaeolithic sequence: frontal section
G-27	Palaeolithic sequence: sagittal section
G-28	Palaeolithic sequence: JKLM proximal zone
G-29	Palaeolithic sequence: JKLM proximal zone
G-30	Palaeolithic sequence: JKLM proximal zone
G-31	Palaeolithic sequence: JKLM proximal zone
G-32	Palaeolithic sequence: sagittal section
G-33	Palaeolithic sequence: JKLM proximal zone
G-34	Mushroom farm: remnant of sedimentary deposit adjacent to the site (axis of the diaclase)
G-35	Mushroom farm: remnant of sedimentary deposit adjacent to the site (axis of the diaclase)
G-36	Mushroom farm and historical quarry adjacent to the site: alterites (alteration features)

SOM Table S2. Micromorphology sample list. ID = numbers reported in Figures S2-S6. S = Small, L = Large.

ID	Micromorphology sample ID	Provenience	Stratigraphic position	Number of thin sections
M-1	RPB-13-1	Back wall (cliff face)	Bedrock	1S
M-2	RPB-13-2	Frontal section	3f/2b	4L
M-3	RPB-13-3-a	Frontal section	4c	2L
M-4	RPB-13-3-b	Frontal section	3f	2L
M-5	RPB-13-3-c	Frontal section	3f	2L
M-6	RPB-13-4	Frontal section	5b/4c	2L
M-7	RPB-13-5	Sagittal section	3a	1L
M-8	RPB-13-6-a	Sagittal section	4c	2L
M-9	RPB-13-6-b	Sagittal section	4c	2L
M-10	RPB-13-6-c	Sagittal section	3f	2L
M-11	RPB-13-7-a	Sagittal section	1a	2L
M-12	RPB-13-7-b	Sagittal section	1a	2L
M-13	RPB-13-8	Frontal section	5b	3L
M-14	RPB-13-9	Frontal section	5c/5b	2L
M-15	RPB-13-10	Sagittal section	3b/3d/2a	3L
M-16	RPB-13-11	Open-pit quarry	Turonian limestone	1S
M-17	RPB-13-12	Open-pit quarry	Turonian limestone	1S
M-18	RPB-13-13	Open-pit quarry	Coniacian limestone	1S
M-19	RPB-13-14	Open-pit quarry	Coniacian limestone	1S
M-20	RPB-13-15	JKLM Frontal section	3b/2a	4L
M-21	RPB-14-1	JKLM Sagittal section	Bedrock	1S
M-22	RPB-14-2	JKLM Sagittal section	Bedrock	1S

M-23	RPB-14-3	JKLM Frontal section	2a	1S
M-24	RPB-14-4	JKLM Frontal section	2a	1L
M-25	RPB-14-8	Open-pit quarry	Glauconite sand	1S
M-26	RPB-15-1	Mushroom farm	Karstic infill	1L
M-27	RPB-15-2	JKLM Sagittal section	4a/3a	3L
M-28	RPB-16-1	JKLM Frontal section	5d	3L
M-29	RPB-16-2	JKLM Frontal section	5d	1L
M-30	RPB-16-3	JKLM Frontal section	5d/4a	1L
M-31	RPB-16-4	Frontal section	3f-reddish lens	1L
M-32	RPB-16-5	Frontal section	5c	2L
M-33	RPB-16-6	Frontal section	3f	1L
M-34	RPB-17-1	JKLM Sagittal section	4a/3a	3L
M-35	RPB-17-2	JKLM Sagittal section	4a	1L
M-36	RPB-18-1	Mushroom farm at J100	Q1	1L
M-37	RPB-21-1	JKLM Frontal section	4a/3c	3XL

SOM Table S3. List of the samples used for OSL and ^{14}C dating. ID = numbers reported in Figures S2-S6. B = Bones; UNG = Ungulate; UF = Ultrafiltration; AAA = acid/alkali/acid pretreatment; RHIN = Rhinoceros; AG = Gelatinization; MAM = Mammal; SED = Sediment; Ds = Dosimeter. Year = sampling date.

ID	Section	Code	Nature	Square	Year	Lab	Note
C-1	Sagittal + JKLM Sagittal	#3083	B-UNG	J4	2016	OxA-36529	UF
C-2	Sagittal + JKLM Sagittal	#1180	B-UNG	J5	2015	OxA-33284	UF
C-3	Sagittal + JKLM Sagittal	#1229	B-RHIN	J5	2015	OxA-36865	UF
C-4	Sagittal + JKLM Sagittal	#3867	B-UNG	J4	2017	OxA-40952	AG
C-5	JKLM Sagittal + JKLM Frontal	#3042	B-UNG	K5	2016	OxA-40933	AG
C-6	JKLM Frontal	#3044	B-UNG	K5	2016	OxA-40934	AG
C-7	JKLM Frontal	#3176	B-MAM	K5	2017	OxA-40935	AG
C-8	JKLM Frontal	#3177	B-UNG	K5	2017	OxA-41095	AG
C-9	JKLM Frontal	#4705	B-UNG	K5	2017	OxA-41096	AG
C-10	JKLM Frontal	#4701	B-UNG	K5	2017	OxA-41025	AF
C-11	Frontal	Sed-2015	SED	F10	2015	Beta - 442685	AAA
C-12	J100	#3703	B-UNG	J100	2018	OxA-38113	UF
O-1	Sagittal	SC15-05-D380	SED	I8	2015	IRAMAT-CRP2A	Ds
O-2	Sagittal	SC15-07-D393	SED	I8	2015	IRAMAT-CRP2A	Ds
O-3	Sagittal	SC15-06-D406	SED	I8	2015	IRAMAT-CRP2A	Ds
O-4	Sagittal	SC17-02-C337	SED	I5	2017	IRAMAT-CRP2A	Ds
O-5	Sagittal	SC17-03-C396	SED	J5	2017	IRAMAT-CRP2A	Ds
O-6	Sagittal	SC17-01-D331	SED	I6	2017	IRAMAT-CRP2A	Ds
O-7	Frontal	SC14-10-D098	SED	C8	2017	IRAMAT-CRP2A	Ds
O-8	Frontal	SC14-08-D129	SED	C8	2017	IRAMAT-CRP2A	Ds
O-9	Frontal	SC14-06-D207	SED	C8	2017	IRAMAT-CRP2A	Ds
O-10	Frontal	SC15-01-D018	SED	F10	2017	IRAMAT-CRP2A	Ds
O-11	Frontal	SC15-04-C308	SED	F10	2017	IRAMAT-CRP2A	Ds

O-12	Frontal	SC15-03-C349	SED	F10	2017	IRAMAT-CRP2A	Ds
O-13	Frontal	SC15-02-C372	SED	F10	2016	IRAMAT-CRP2A	Ds
O-14	JKLM Frontal	SC17-04	SED	K5	2017	IRAMAT-CRP2A	-
O-15	JKLM Frontal	SC19-01	SED	K4	2019	IRAMAT-CRP2A	-
O-16	J100	SC19-02	SED	J100	2019	IRAMAT-CRP2A	-

SOM Table S4. Main and secondary crystalline phases identified and quantified (%) by XRD. ID = numbers reported in Table S1 and in the PCA biplot (Figure 9A, main text).

ID	QZ	KAO	MUS	CAL	GOE	SME	APA	BIO	PLA	MIC
1	7.71	92.29	0	0	0	0	0	0	0	0
2	9.60	45.25	4.05	1.74	5.47	33.89	0	0	0	0
3	60.48	31.98	0	0	7.54	0	0	0	0	0
4	50.73	22.56	8.45	0	10.9	7.36	0	0	0	0
5	75.94	20.41	0	0	3.65	0	0	0	0	0
6	87.85	1.11	0	11.05	0	0	0	0	0	0
7	32.1	38.27	5.2	15.23	6.71	2.49	0	0	0	0
8	7.16	33.74	8.08	30.03	3.29	17.71	0	0	0	0
9	24.19	0.98	0	74.82	0	0	0	0	0	0
10	22.18	3.64	36.91	0.78	6.58	29.91	0	0	0	0
12	38.02	0.36	4.37	57.25	0	0	0	0	0	0
13	31.73	0.33	2.42	65.52	0	0	0	0	0	0
14	3.68	0	0.19	96.13	0	0	0	0	0	0
15	3.10	0	0	96.90	0	0	0	0	0	0
16	27.52	13.35	0	58.57	0.56	0	0	0	0	0
17	25.96	7.46	0	66.32	0.25	0	0	0	0	0
18	35.34	13.58	0	50.66	0.42	0	0	0	0	0
19	29.62	0	0	70.29	0.08	0	0	0	0	0
20	31.39	11.19	0	56.88	0.54	0	0	0	0	0
21	44.03	10.71	0	44.07	1.18	0	0	0	0	0
22	49.39	9.01	0	41.36	0.24	0	0	0	0	0
23	73.14	2.87	0	23.95	0.03	0	0	0	0	0
24	61.1	3.34	0	35.03	0.53	0	0	0	0	0
25	47.84	12.3	0	39.38	0.49	0	0	0	0	0
26	44.06	13.84	0	41.56	0.54	0	0	0	0	0
27	22	2.89	0	75.11	0	0	0	0	0	0
28	34.76	4.62	0	60.3	0.32	0	0	0	0	0
29	22.97	1.65	0	75.07	0.31	0	0	0	0	0
30	36.73	1.7	0	50.59	0	4.51	6.48	0	0	0
31	42.58	0.19	9.25	39.63	0.63	7.72	0	0	0	0
32	34.02	3.4	0	61.47	0	0.21	0	0	0.69	0.21
33	42.55	3.03	0	53.47	0	0.15	0	0	0.8	0
34	8.59	0	0	90.96	0	0	0	0.45	0	0
35	41.56	0.32	6.64	40.76	0.97	9.74	0	0	0	0
36	5.48	0.91	19.91	16.12	3.21	54.37	0	0	0	0

Note: QZ = quartz; KAO = kaolinite; MUS = muscovite; CAL = calcite; GOE = goethite; SME = smectite; APA = apatite; BIO = biotite; PLA = plagioclase; MIC = microcline. Traces of additional phases may be present.

SOM Table S5. Minimum and maximum percentages of crystalline phases identified and quantified by XRD (values excluding mushroom farm/historical quarry). “e-s” = extra-site; "i-s" = intra-site.

	QZ	KAO	MUS	CAL	GOE	SME	APA	BIO	PLA	MIC
Min	3.1	0	0	0	0	0	0	0	0	0
Max	87.85	92.29	36.91	96.9	10.9	54.37	6.48	0.45	0	0
Min e-s	5.48	0.91	0	0	0	0	0	0	0	0
Max e-s	87.85	92.29	36.91	74.82	10.9	54.37	0	0	0	0
Min i-s	3.1	0	0	23.95	0	0	0	0	0	0
Max i-s	73.14	13.84	9.25	96.9	1.18	7.72	6.48	0	0	0

Note: QZ = quartz; KAO = kaolinite; MUS = muscovite; CAL = calcite; GOE = goethite; SME = smectite; APA = apatite; BIO = biotite; PLA = plagioclase; MIC = microcline.

SOM Table S6. Major-minor elements (dose percentages) quantified by ICP-OES and loss on ignition (LOI) raw data. ID = numbers reported in Table S1 and in the PCA biplot (Figure 9B, main text).

ID	SiO_2	Al_2O_3	Fe_2O_3	MnO	MgO	CaO	Na_2O	K_2O	TiO_2	P_2O_5	LOI
1	50.83	27.07	0.62	0.0016	0.04	0.07	0.08	0.09	0.84	0	19.42
2	43.43	23.20	4.92	0.0077	1.04	1.30	0.12	1.20	0.60	0.070	23.13
3	70.18	12.80	5.48	0.0045	0.34	0.24	0.06	0.47	0.66	0.020	9.25
4	56.05	15.88	6.19	0.057	0.85	0.84	0.10	1.07	0.47	0.15	19.26
5	69.11	8.06	9.76	0.0090	0.20	0.20	0.04	0.31	0.59	0.040	11.42
6	94.55	0.91	0.29	0.0034	0.06	1.49	0.02	0.35	0.065	0	1.64
7	47.27	23.53	6.72	0.010	1.17	2.09	0.18	1.32	0.69	0.090	15.62
8	42.46	22.38	7.31	0.0096	1.38	5.52	0.14	1.22	0.54	0.050	18.52
9	38.83	5.96	2.24	0.022	0.45	18.97	0.27	0.84	0.30	0.13	30.84
10	51.76	23.85	6.77	0	1.12	1.37	0.11	1.29	0.82	0.10	12.33
11	83.57	0.70	0.41	0	0.09	7.97	0.04	0.13	0.055	0	6.84
12	35.41	3.51	1.65	0.012	0.28	28.72	0.12	0.36	0.18	3.65	25.25
13	33.71	3.23	1.03	0.0096	0.28	30.73	0.13	0.38	0.18	3.88	26.13
14	2.51	0.39	0.11	0.0032	0.16	53.74	0.02	0.04	0.019	0.13	42.39
15	2.21	0.33	0.09	0.0030	0.15	52.89	0.02	0.04	0.018	0.080	43.97
16	40.95	6.91	2.55	0.024	0.48	22.61	0.13	0.73	0.34	0.32	24.58
17	28.11	4.99	1.82	0.022	0.39	33.16	0.10	0.52	0.24	0.53	30.08
18	41.33	5.56	2.05	0.016	0.43	24.80	0.12	0.58	0.30	1.06	23.82
19	27.69	2.06	1.01	0.019	0.19	37.08	0.06	0.25	0.15	0.17	31.16
20	41.81	5.82	2.05	0.014	0.42	24.50	0.12	0.59	0.31	0.76	23.35
21	46.21	6.18	1.99	0.016	0.43	21.68	0.16	0.67	0.35	1.98	20.03
22	51.22	6.94	2.76	0.012	0.49	16.84	0.17	0.80	0.38	0.16	20.14
23	69.49	6.82	2.72	0.074	0.43	7.11	0.19	0.83	0.46	0.19	11.26
24	61.95	4.54	1.98	0.047	0.29	13.90	0.14	0.59	0.35	0.15	15.24
25	36.60	4.08	1.70	0.012	0.34	29.28	0.13	0.53	0.24	0.15	26.87
26	40.12	4.81	1.70	0.011	0.36	26.31	0.14	0.58	0.28	0.76	24.54

27	26.00	2.39	0.65	0.0059	0.23	36.18	0.08	0.28	0.13	1.48	32.31
28	29.52	2.74	1.04	0.018	0.27	33.78	0.22	0.32	0.16	8.00	22.79
29	21.19	1.97	0.61	0.0076	0.22	40.54	0.08	0.23	0.12	2.04	32.22
30	41.18	3.75	1.24	0	0.32	25.99	0.18	0.44	0.22	5.77	20.66
31	46.20	7.90	3.05	0.034	0.57	17.73	0.15	0.79	0.42	0.84	21.90
32	26.58	3.89	1.49	0	0.33	36.15	0.08	0.40	0.21	0.59	30.04
33	31.18	3.95	1.69	0.018	0.33	33.18	0.11	0.42	0.21	1.52	27.23
34	11.44	1.92	0.75	0	0.25	46.37	0.10	0.23	0.091	1.60	36.56
35	55.72	8.92	3.14	0.028	0.60	13.99	0.25	1.01	0.45	0.23	15.43

Note: 0 is assigned if values < limit of detection.

SOM Table S7. Trace elements (µg/g; ppm) quantified by ICP-MS (raw data) showing the highest inter-sample variability. ID = numbers reported in Table S1 and in the PCA biplot (Figure 9C, main text).

ID	Ba	Cr	Nb	Ni	Rb	Sr	V	Zn	Zr	Ce
1	126	23.5	290	90.5	5.31	9.4	21.0	0	602	161
2	163	168	16.1	82.1	161	37.8	146	169	106	41.5
3	78.1	96.6	16.1	22.3	52.3	22.2	149	30.2	396	41.5
4	164	109	11.4	42.3	115	30.4	142	87.0	82.0	52.1
5	59.8	126	14.3	22.9	38.2	16.9	182	33.2	496	42.3
6	37.5	14.2	1.19	3.3	12.4	7.7	9.5	8.2	29.2	7.53
7	165	208	17.5	108	165	42.7	183	180	112	68.1
8	186	174	15.4	82.3	154	44.4	187	146	116	52.3
9	141	48.6	7.40	20.2	53.4	58.7	48.9	45.0	137	40.8
10	180	173	19.6	101	153	44.2	189	160	149	74.3
11	24.4	9.0	0.85	2.8	5.05	22.7	8.2	11.4	39.9	8.13
12	79.0	31.1	4.26	13.1	26.6	58.8	42.7	63.6	96.3	29.3
13	76.6	24.0	3.95	9.9	26.1	67.5	23.9	80.4	90.5	24.7
14	7.5	6.9	0.44	0	3.04	85.4	3.6	9.5	9.10	3.24
15	6.9	4.9	0.40	0	2.56	86.5	3.4	0	7.56	2.56
16	114	49.7	7.45	21.1	51.6	39.1	61.2	63.4	136	47.3
17	80.2	35.4	5.32	14.7	36.2	53.2	44.6	51.5	100	32.9
18	95.3	40.6	6.35	16.3	41.2	54.2	46.8	65.7	150	42.6
19	41.1	20.5	3.07	6.4	17.7	64.7	23.4	19.5	74.8	18.4
20	95.1	42.9	6.76	16.1	41.1	48.6	50.9	52.2	159	42.7
21	118	45.3	8.13	17.4	48.0	59.7	57.5	71.0	158	46.6
22	130	51.3	8.41	24.5	53.1	56.2	69.4	47.4	171	52.1
23	152	53.6	9.46	19.7	62.7	37.7	57.3	58.8	244	60.4
24	99.9	39.0	7.07	12.8	41.6	40.0	43.2	37.5	176	41.6
25	84.4	29.8	5.06	11.1	33.3	67.3	38.8	31.3	109	32.0
26	102	35.9	5.98	13.9	38.6	64.9	40.4	47.7	140	37.1

27	50.5	18.0	2.80	6.6	18.9	66.8	17.4	50.0	69.7	20.4
28	87.0	21.5	3.43	10.7	21.9	82.6	21.9	104	80.4	20.6
29	55.6	19.0	2.73	6.5	16.9	78.5	15.6	53.0	75.6	16.6
30	103	28.6	4.49	12.1	27.5	76.6	26.3	77.5	137	28.6
31	130	57.9	8.52	24.5	53.2	50.8	70.3	65.4	201	57.8
32	67.0	31.4	4.25	11.9	27.0	67.3	34.5	42.4	98.7	26.9
33	74.5	33.3	4.34	11.6	26.9	64.9	37.0	57.1	109	28.3
34	45.1	15.6	1.87	7.4	14.2	89.4	17.6	47.7	52.8	13.1
35	149	64.7	9.14	27.2	68.3	49.5	75.2	55.4	169	57.1

Note: 0 is assigned if values < limit of detection; only trace elements with standard deviation (SD) > 20 are presented.

SOM Table S8. Hyperlinks to high-resolution scans of selected thin sections (see Figure S15 with sample labels underlined in blue).

Micromorphology sample ID	Hyperlinks to high-resolution scans
3-1/RPB-13-3a-1	http://geodig.synology.me/section/1070
3-2/RPB-13-3a-2	http://geodig.synology.me/section/1071
3-3/RPB-13-3a-3	http://geodig.synology.me/section/1072
3-4/RPB-13-3b-1	http://geodig.synology.me/section/1073
3-5/RPB-13-3b-2	http://geodig.synology.me/section/1074
3-6/RPB-13-3b-3	http://geodig.synology.me/section/1075
5-1/RPB-13-3c-1a	http://geodig.synology.me/section/1076
5-2/RPB-13-3c-1b	http://geodig.synology.me/section/1077
7-1/RPB-13-5a	http://geodig.synology.me/section/1068
7-2/RPB-13-5b	http://geodig.synology.me/section/1069
8-1/RPB-13-6a-1	http://geodig.synology.me/section/1061
8-2/RPB-13-6a-2	http://geodig.synology.me/section/1062
8-3/RPB-13-6a-3	http://geodig.synology.me/section/1063
9-1/RPB-13-6b-1	http://geodig.synology.me/section/1064
9-2/RPB-13-6b-2	http://geodig.synology.me/section/1065
10/RPB-13-6c-1	http://geodig.synology.me/section/1066
11/RPB-13-7a-1	http://geodig.synology.me/section/1332
11/RPB-13-7a-2	http://geodig.synology.me/section/1333
11/RPB-13-7a-3	http://geodig.synology.me/section/1334
11/RPB-13-7a-4	http://geodig.synology.me/section/1335
15-1/RPB-13-10-1	http://geodig.synology.me/section/1059
15-2/RPB-13-10-2	http://geodig.synology.me/section/1058
15-3/RPB-13-10-3	http://geodig.synology.me/section/716
15-4/RPB-13-10-4	http://geodig.synology.me/section/715
20-1/RPB-13-15-3	http://geodig.synology.me/section/1081
20-2/RPB-13-15-4	http://geodig.synology.me/section/1082
23/RPB-14-3	http://geodig.synology.me/section/1329
24/RPB-14-4	http://geodig.synology.me/section/1331

SOM Table S9. Circular statistics of Facies 4a-sup. (2014-2018 data). Analyses carried out on square metres with at least 30 measured archaeological remains; "*< 0.05"* = significant p-value (threshold < 0.05) rejecting the null hypothesis that the fabric corresponds to the distribution tested.

Top of Facies 4a	**J3**	**J4**	**J3-J4**
Number of Observations	48	100	148
Mean Vector (μ)	349.864°	342.362°	344.014°
Length of Mean Vector (r)	0.248	0.422	0.365
Concentration (k)	0.513	0.929	0.784
Circular Variance	0.752	0.578	0.635
Circular Standard Deviation	95.631°	75.312°	81.366°
Rayleigh Test (Z)	2.961	17.768	19.698
Rayleigh Test (p)	0.051	***1.92E-08***	***2.79E-09***
Rao's Spacing Test (U)	148	188.4	180.676
Rao's Spacing Test (p)	0.10 > p > 0.05	***< 0.01***	***< 0.01***
Watson's U^2 Test (Uniform. U^2)	0.213	1.141	1.235
Watson's U^2 Test (p)	***< 0.05***	***< 0.005***	***< 0.005***
Kuiper's Test (Uniform. V)	1.987	3.574	3.791
Kuiper's Test (p)	***< 0.025***	***< 0.01***	***< 0.01***
Watson's U^2 Test (von Mises. U^2)	0.062	0.324	0.268
Watson's U^2 Test (p)	0.1 > p > 0.05	***< 0.005***	***< 0.005***
Kuiper's Test (von Mises. V)	1.259	2.421	1.944
Kuiper's Test (p)	> 0.15	***< 0.01***	***< 0.025***

Analyses on axial data (0-180°) equivalent to doubled angles			
Rayleigh Test (Z)	2.946	8.204	10.193
Rayleigh Test (p)	0.052	***2.74E-04***	***3.74E-05***
Rao's Spacing Test (U)	163.5	187.2	199.081
Rao's Spacing Test (p)	***< 0.01***	***< 0.01***	***< 0.01***
Watson's U^2 Test (Uniform. U^2)	0.172	0.525	0.573
Watson's U^2 Test (p)	0.1 > p > 0.05	***< 0.005***	***< 0.005***
Kuiper's Test (Uniform. V)	1.602	2.68	2.598
Kuiper's Test (p)	0.15 > p > 0.10	***< 0.01***	***< 0.01***

SOM Table S10. Circular statistics of Facies 4a-inf. (2014-2018 data). Analyses carried out on square metres with at least 30 measured archaeological remains; "*< 0.05"* = significant p-value (threshold < 0.05) rejecting the null hypothesis that the fabric corresponds to the distribution tested.

Base of Facies 4a	**J4**	**J5**	**K4**	**K5**	**K4-K5**	**J4-J5**	**J5-K5**	**J4-K4**
Number of Observations	165	43	66	60	126	208	103	231
Mean Vector (μ)	337.083°	352.68°	227.694°	278.189°	256.544°	341.805°	323.176°	323.721°
Length of Mean Vector (r)	0.357	0.598	0.207	0.298	0.227	0.404	0.34	0.242
Concentration (k)	0.764	1.5	0.424	0.625	0.467	0.882	0.723	0.499
Circular Variance	0.643	0.402	0.793	0.702	0.773	0.596	0.66	0.758
Circular Standard Deviation	82.238°	58.129°	101.631°	89.105°	98.635°	77.187°	84.147°	96.536°
Rayleigh Test (Z)	21.026	15.362	2.839	5.343	6.506	33.875	11.915	13.512
Rayleigh Test (p)	***7.39E-10***	***6.14E-08***	0.059	***0.005***	***0.001***	***< 1E-12***	***6.69E-06***	***1.35E-06***
Rao's Spacing Test (U)	192.727	225.023	132.545	194	168.143	199.808	189.67	190.857
Rao's Spacing Test (p)	***< 0.01***	***< 0.01***	0.50 > p > 0.10	***< 0.01***	***< 0.01***	***< 0.01***	***< 0.01***	***< 0.01***
Watson's U² Test (Uniform. U²)	1.131	0.904	0.17	0.315	0.362	1.787	0.659	0.728
Watson's U² Test (p)	***< 0.005***	***< 0.005***	0.1 > p > 0.05	***< 0.005***	***< 0.005***	***< 0.005***	***< 0.005***	***< 0.005***
Kuiper's Test (Uniform. V)	3.413	3.206	1.783	2.225	2.24	3.984	2.746	2.886
Kuiper's Test (p)	***< 0.01***	***< 0.01***	***< 0.05***	***< 0.01***	***< 0.01***	***< 0.01***	***< 0.01***	***< 0.01***
Watson's U² Test (von Mises. U²)	0.074	0.134	0.03	0.05	0.033	0.062	0.052	0.045
Watson's U² Test (p)	0.1 > p > 0.05	***< 0.01***	> 0.5	0.25 > p > 0.15	0.5 > p > 0.25	0.15 > p > 0.1	0.25 > p > 0.15	0.25 > p > 0.15
Kuiper's Test (von Mises. V)	1.235	1.816	0.901	1.138	0.922	1.155	1.097	1.015
Kuiper's Test (p)	> 0.15	***< 0.05***	> 0.15	> 0.15	> 0.15	> 0.15	> 0.15	> 0.15

Analyses on axial data (0-180°) equivalent to doubled angles								
Rayleigh Test (Z) – 180°	0.487	5.137	0.437	0.349	0.241	1.058	0.47	1.488
Rayleigh Test (p) – 180°	0.614	***0.005***	0.646	0.706	0.786	0.347	0.625	0.226
Rao's Spacing Test (U) – 180°	204.182	181.907	142.364	196	177.143	218.077	210.39	180.738
Rao's Spacing Test (p) – 180°	< ***0.01***	< ***0.01***	0.50 > p > 0.10	< ***0.01***	< ***0.01***	< ***0.01***	< ***0.01***	< ***0.01***
Watson's U² Test (Uniform. U²) – 180°	0.161	0.334	0.049	0.098	0.065	0.141	0.126	0.125
Watson's U² Test (p) – 180°	0.1 > p > 0.05	< ***0.005***	> 0.5	0.5 > p > 0.25	> 0.5	0.15 > p > 0.1	0.25 > p > 0.15	0.25 > p > 0.15
Kuiper's Test (Uniform. V) – 180°	1.828	2.333	1.066	1.63	1.203	1.932	1.645	1.432
Kuiper's Test (p) – 180°	< ***0.05***	< ***0.01***	> 0.15	0.10 > p > 0.05	> 0.15	< ***0.025***	0.10 > p > 0.05	> 0.15

SOM Table S11. Circular statistics of Facies 3a (2014-2018 data). Analyses carried out on square metres with at least 30 measured archaeological remains; "*< 0.05"* = significant p-value (threshold < 0.05) rejecting the null hypothesis that the fabric corresponds to the distribution tested.

Facies 3a	J4	J5	K4	K4-K5	J4-J5	J4-K4	J5-K5
Number of Observations	33	54	65	93	87	98	82
Mean Vector (μ)	341.358°	37.354°	238.452°	246.921°	14.786°	272.758°	28.749°
Length of Mean Vector (r)	0.263	0.231	0.221	0.156	0.216	0.153	0.163
Concentration (k)	0.546	0.475	0.453	0.316	0.442	0.311	0.331
Circular Variance	0.737	0.769	0.779	0.844	0.784	0.847	0.837
Circular Standard Deviation	93.584°	98.072°	99.564°	110.39°	100.331°	110.941°	109.089°
Rayleigh Test (Z)	2.29	2.884	3.173	2.272	4.053	2.307	2.185
Rayleigh Test (p)	0.101	0.056	***0.042***	0.103	***0.017***	0.1	0.112
Rao's Spacing Test (U)	175	164.333	143.154	152.903	160.69	155.082	155.463
Rao's Spacing Test (p)	***< 0.01***	***< 0.01***	0.50 > p > 0.10	***< 0.05***	***< 0.01***	***< 0.01***	***< 0.01***
Watson's U^2 Test (Uniform. U^2)	0.171	0.227	0.229	0.193	0.276	0.187	0.195
Watson's U^2 Test (p)	0.1 > p > 0.05	***< 0.025***	***< 0.025***	***< 0.05***	***< 0.01***	***< 0.05***	***< 0.05***
Kuiper's Test (Uniform. V)	1.76	1.71	1.856	1.862	2.077	1.761	1.815
Kuiper's Test (p)	***< 0.05***	0.10 > p > 0.05	***< 0.05***	***< 0.05***	***< 0.01***	***< 0.05***	***< 0.05***
Watson's U^2 Test (von Mises. U^2)	0.067	0.098	0.077	0.088	0.082	0.071	0.097
Watson's U^2 Test (p)	0.1 > p > 0.05	***< 0.01***	***< 0.025***	***< 0.025***	***< 0.025***	***< 0.05***	***< 0.01***
Kuiper's Test (von Mises. V)	1.311	1.365	1.408	1.456	1.191	1.217	1.33
Kuiper's Test (p)	> 0.15	> 0.15	> 0.15	> 0.15	> 0.15	> 0.15	> 0.15

Analyses on axial data (0-180°) equivalent to doubled angles							
Rayleigh Test (Z)	1.576	3.089	2.133	2.849	3.115	2.481	3.694
Rayleigh Test (p)	0.208	***0.046***	0.118	0.058	***0.044***	0.084	***0.025***
Rao's Spacing Test (U)	167.818	161.333	123.846	141.935	162.276	137.673	160.244
Rao's Spacing Test (p)	< ***0.01***	< ***0.01***	0.90 > p > 0.50	0.50 > p > 0.10	< ***0.01***	0.50 > p > 0.10	< ***0.01***
Watson's U^2 Test (Uniform. U^2)	0.14	0.27	0.16	0.197	0.243	0.176	0.283
Watson's U^2 Test (p)	0.15 > p > 0.1	< ***0.01***	0.1 > p > 0.05	< ***0.05***	< ***0.025***	0.1 > p > 0.05	< ***0.01***
Kuiper's Test (Uniform. V)	1.734	2.052	1.723	1.898	1.798	1.527	2.055
Kuiper's Test (p)	0.10 > p > 0.05	< ***0.01***	0.10 > p > 0.05	< ***0.025***	< ***0.05***	> 0.1	< ***0.01***

SOM Table S12. Similarity tests of fabric series (2014-2018 data). Matrix of probabilities (p) from Moore's paired test. "*< 0.01*" = significant p-value (threshold < 0.05) rejecting the null hypothesis that the fabric series are similar.

		Facies 4a-sup.		**Facies 4a-inf.**				**Facies 3a**		
		J3	**J4**	**J4**	**J5**	**K4**	**K5**	**J4**	**J5**	**K4**
Facies 4a-sup.	J3	-----	0.9 > p > 0.5	0.5 > p > 0.1	***< 0.05***	0.1 > p > 0.05	***< 0.005***	0.9 > p > 0.5	0.5 > p > 0.1	***< 0.05***
	J4	0.253	-----	0.1 > p > 0.05	***< 0.05***	***< 0.001***	***< 0.005***	0.9 > p > 0.5	0.5 > p > 0.1	***< 0.001***
Facies 4a- inf.	J4	0.779	0.994	-----	***< 0.001***	***< 0.05***	0.5 > p > 0.1	0.5 > p > 0.1	***< 0.025***	0.1 > p > 0.05
	J5	1.106	1.063	1.585	-----	***< 0.001***	***< 0.001***	0.1 > p > 0.05	***< 0.001***	***< 0.001***
	K4	0.893	1.965	1.014	1.9	-----	0.5 > p > 0.1	***< 0.05***	***< 0.01***	0.995 > p > 0.990
	K5	1.338	1.379	0.69	2.101	0.868	-----	***< 0.01***	***< 0.005***	0.5 > p > 0.1
Facies 3a	J4	0.315	0.22	0.777	0.92	1.074	1.288	-----	***< 0.025***	0.1 > p > 0.05
	J5	0.847	0.795	1.135	1.512	1.26	1.36	1.125	-----	***< 0.005***
	K4	1.093	1.842	1	1.799	0.058	0.685	0.954	1.413	-----

SOM Table S13. List of the samples used for ^{14}C dating, associated dates and biochemical parameters.

ID	^{14}C date	%Yield	%C	%N	CN	δ13C (‰)	δ15N (‰)	Cal BP (IntCal20, 2 σ)	Lab code
C-1	34 350 +/- 550 BP	5.6	46.0	1.30	3.2	-20.60	4.90	37 733 – 40 710	OxA-36529
C-2	35 650 +/- 700 BP	2.6	43.70	0.76	3.2	-18.73	7.80	39 560 – 41 926	OxA-33284
C-3	35 100 +/- 650 BP	1.5	42.0	0.30	3.2	-20.10	6.30	39 100 – 41 565	OxA-36865
C-4	37 300 +/- 1300 BP	1.2	38.1	0.64	3.3	-19.74	4.96	39 961 – 44 018	OxA-40952
C-5	35 190 +/- 750 BP	3.9	47.3	0.86	3.2	-19.99	7.23	39 045 – 41 891	OxA-40933
C-6	31 100 +/- 450 BP	2.3	46.2	0.72	3.3	-18.74	11.52	34 593 – 36 318	OxA-40934
C-7	36 040 +/- 850 BP	2.0	43.9	0.71	3.2	-20.47	6.90	39 687 – 42 217	OxA-40935
C-8	35 360 +/- 940 BP	2.7	42.8	0.64	3.4	-20.50	4.52	38 663 – 42 165	OxA-41095
C-9	38 800 +/- 1300 BP	1.2	32.7	0.70	3.2	-19.96	8.81	41 284 – 44 960	OxA-41096
C-10	43 100 +/- 1800 BP	2.5	44.3	0.59	3.2	-21.09	7.23	43 011 – 51 642	OxA-41025
C-11	1 360 +/- 30 BP	-	0.55	-	-	-25.02	7.30	1 176 – 1 343	Beta- 442685
C-12	34 850 +/- 660 BP	2.9	44.2	0.73	3.4	-18.83	6.94	38 455 – 41 400	OxA-38113

Note: The %Yield, %C, %N, CN tests were performed for the testing of bones as an indication of the overall degree of preservation of the collagen proteins. For sample C-11, %C is a laboratory estimate between 0.50% and 0.60% corresponding to ~22 mg of carbon available from the combustion (graphitization).

SOM Table S14. SAR protocol adopted for the OSL multi-grains D_e determination (left) and single-grain D_e determination (right). The best parameters (temperature and duration) for the Preheats have been determined for each sample, through the Dose Recovery Tests measurements. The test dose has been chosen as being around 70% of the first given regeneration dose. Note that a final IR depletion ratio test has been conducted for each aliquot, to ensure the absence of K-feldspars signals in the measured signals (Duller, 2003).

	Multi-grains D_e determination	Single-grain D_e determination
1	Irradiation D_i (dose=0 for i=1)	Irradiation D_i (dose=0 for i=1)
2	Preheat @220°C or 200°C for 10s	Preheat @220°C or 200°C for 10s
3	OSL green LEDs @125°C for 100s => L_N or L_x	SG-OSL @125°C during 2s
4	Irradiation (test dose)	Irradiation (test dose)
5	Preheat @180°C for 0s	Preheat @180°C for 0s
6	OSL green LEDs @125°C for 100s => T_N or T_x	SG-OSL @125°C during 2s
7	OSL blue LEDs @280°C for 40s (optical cleaning)	OSL blue LEDs @280°C for 40s (optical cleaning)
8	Back to step 1 with dose D_{i+1}	Back to step 1 with dose D_{i+1}

SOM Table S15. Overdispersion values obtained with the Central Age Model (CAM) during Dose Recovery Test measurements. These values are considered to correspond to the intrinsic overdispersion of each sample. For samples O-6, O-4 and O-5 (i.e., SC17-01, SC17-02 and SC17-03) where the DRT measurements have not been conducted the OD value (in italics) considered is the mean value obtained for the two closest samples, namely O-14 and O-15 (i.e., SC17-04 and SC19-01). The ratio of the dose recovery test is indicated when relevant.

ID	Sample	OD (%) CAM	Dose recovery ratio
O-13	SC15-02	16 ± 2	1.03 ± 0.02
O-10	SC15-01	25 ± 2	0.93 ± 0.02
O-3	SC15-06	12 ± 2	0.96 ± 0.02
O-1	SC15-05	23 ± 3	0.93 ± 0.03
O-4	SC17-02	*12.5 ± 3*	-
O-5	SC17-03	*12.5 ± 3*	-
O-6	SC17-01	*12.5 ± 3*	-
O-14	SC17-04	16 ± 2	1.00 ± 0.02
O-15	SC19-01	9 ± 1	0.97 ± 0.01
O-16	SC19-02	8 ± 1	1.02 ± 0.02

SOM Table S16. Multi-grain (MG)-OSL measurements on medium and coarse-grain samples. ADM = Average Dose Model. Results of D_e and age in italics correspond to samples measured with few aliquots or only preheat plateau estimations (see text for further details); n is the number of aliquots used for De determination, N the total number of aliquots measured.

ID	Sample	Section	Note	Grain fraction	n/N	De (Gy) ADM	σ_d ADM (%)	Age ADM (ka)
-	SC14-02		Not suitable for dating	20-41 µm				
-	SC14-04		Not suitable for dating	20-41 µm				
O-9	SC14-06	C8 Frontal		20-41 µm	24/24	66.34 ± 1.49	0 ± 0	52.5 ± 3.8
O-8	SC14-08	C8 Frontal		20-41 µm	28/28	43.26 ± 0.91	0 ± 0	50.5 ± 3.1
O-7	SC14-10	C8 Frontal		20-41 µm	26/26	41.45 ± 0.89	0 ± 0	59.2 ± 3.9
O-11	SC15-04	F10 Frontal		180-250 µm	*5/24*	*0.62 ± 0.02*	*0 ± 0*	*0.8 ± 0.1*
O-12	SC15-03	F10 Frontal		180-250 µm	24*/24*	*4.51 ± 0.37*	*35 ± 5*	*3.2 ± 0.3*
O-2	SC15-07	U5 I8 Sagittal		180-250 µm	*4/24*	*3.05 ± 0.65*	*39 ± 13*	*2.6 ± 0.6*

SOM Table S17. Single-grain (SG)-OSL measurements. n is the number of grains that passed all tests, used for D_e determination, N the total number of grains that give a luminescence signal.

ID	Sample	Section	Grain fraction	n/N	De (Gy) ADM	σ_m (from DRT)	σ_d ADM	Age ADM (ka)
O-13	SC15-02	F10 Frontal	180-250 µm	184/305	52.9 ± 1.7	16 ± 2	27 ± 5	53.8 ± 3.4
O-10	SC15-01	F10 Frontal	180-250 µm	218/395	50.1 ± 1.6	25 ± 2	20 ± 5	59.9 ± 4.3
O-3	SC15-06	I8 Sagittal	180-250 µm	214/423	67.8 ± 2.2	12 ± 2	27 ± 3	40.5 ± 2.8
O-1	SC15-05	I8 Sagittal	180-250 µm	223/412	59.9 ± 1.9	23 ± 3	21 ± 4	45.5 ± 3.0
O-4	SC17-02	I5 Sagittal	180-250 µm	214/263	45.5 ± 1.4	12 ± 2	32 ± 4	45.5 ± 2.6
O-5	SC17-03	J5 Sagittal	180-250 µm	205/260 (ADM)	49.2 ± 1.6	12 ± 3	33 ± 4	47.9 ± 2.9
O-5	SC17-03	J5 Sagittal	180-250 µm	205 (FMM)	41.8 ± 0.6 (82.5%) 84.4 ± 3.2 (17.5%)	-	- (FMM)	40.6 ± 2.0
O-6	SC17-01	I6 Sagittal	180-250 µm	213/260	38.8 ± 1.17	12 ± 2	30 ± 3	50.6 ± 3.9
O-14	SC17-04	K5 Frontal	180-250 µm	443/552	54.8 ± 0.9	16 ± 2	26 ± 2	41.0 ± 2.0
O-15	SC19-01	K4 Frontal	200-250 µm	137/151	57.1 ± 1.4	9 ± 1	23 ± 2	39.3 ± 2.1
O-16	SC19-02	J100 / cave	200-250 µm	177/269	63.0 ± 2.1	8 ± 1	31 ± 3	40.1 ± 2.4

SOM Table S18. KUTh contents of the sediment, measured using a HP-LB gamma spectrometer in the IRAMAT-CRP2A laboratory, after Guibert and Schvoerer (1991). Estimated water content during burial is provided (mean values of the *in situ* water contents measured at the time of sampling). Derived alpha and beta dose rates are presented (a-value from Tribolo et al., 2001), as well as the gamma+cosmic dose rates, measured with Al_2O_3:C dosimeters or calculated. The total dose rate for each dated sample is also given.

ID	Sample	Estimated water content (%)	K (%)	U (from U(^{226}Ra)) (ppm)	Th (ppm)	Alpha dose rate (Gy/ka)	Beta dose rate (Gy/ka)	gamma+cos Dose rate (Gy/ka)	Total dose rate (Gy/ka)
O-9	SC14-06 MG /medium grain	12 ± 4	0.40 ± 0.08	1.40 ± 0.02	6.00 ± 0.05	0.11 ± 0.01	0.57 ± 0.01	0.58 ± 0.01	1.26 ± 0.05
O-8	SC14-08 MG / medium grain	12 ± 4	0.23 ± 0.01	1.07 ± 0.01	3.53 ± 0.04	0.07 ± 0.01	0.36 ± 0.01	0.42 ± 0.01	0.86 ± 0.02
O-7	SC14-10 MG / medium grain	12 ± 4	0.18 ± 0.01	0.62 ± 0.02	2.50 ± 0.05	0.05 ± 0.01	0.25 ± 0.01	0.40 ± 0.02	0.70 ± 0.02
O-11	SC15-04 MG /coarse grain	12 ± 4	0.20 ± 0.01	0.72 ± 0.01	3.06 ± 0.04	0.01 ± 0.01	0.26 ± 0.01	0.46 ± 0.02	0.73 ± 0.02
O-12	SC15-03 MG /coarse grain	12 ± 4	0.64 ± 0.01	1.53 ± 0.02	8.03 ± 0.07	-	0.70 ± 0.01	0.73 ± 0.02	1.43 ± 0.03
O-2	SC15-07 MG /coarse grain	12 ± 4	0.43 ± 0.01	1.18 ± 0.02	6.00 ± 0.06	-	0.49 ± 0.01	0.69 ± 0.02	1.19 ± 0.02
O-13	SC15-02 coarse grain	12 ± 4	0.48 ± 0.01	1.22 ± 0.02	6.22 ± 0.06	-	0.54 ± 0.01	0.45 ± 0.01	0.98 ± 0.01
O-10	SC15-01 coarse grain	12 ± 4	0.32 ± 0.01	1.11 ± 0.01	4.58 ± 0.05	-	0.39 ± 0.01	0.44 ± 0.01	0.84 ± 0.01
O-3	SC15-06 coarse grain	12 ± 4	0.80 ± 0.01	2.03 ± 0.02	9.71 ± 0.09	-	0.88 ± 0.01	0.80 ± 0.01	1.67 ± 0.05
O-1	SC15-05 SG /coarse grain	12 ± 4	0.70 ± 0.02	1.36 ± 0.02	7.84 ± 0.08	-	0.71 ± 0.01	0.60 ± 0.02	1.31 ± 0.03
O-6	SC17-01 SG /coarse grain	8 ± 4	0.25 ± 0.01	0.71 ± 0.02	3.29 ± 0.04	-	0.31 ± 0.01	0.45 ± 0.05	0.77 ± 0.01
O-4	SC17-02 SG /coarse grain	8 ± 4	0.33 ± 0.01	1.11 ± 0.01	4.41 ± 0.04	-	0.43 ± 0.01	0.57 ± 0.6	1.00 ± 0.01

O-5	SC17-03 SG /coarse grain	8 ± 4	0.34 ± 0.01	1.09 ± 0.01	4.79 ± 0.04	-	0.44 ± 0.01	0.59 ± 0.06	1.03 ± 0.01
O-14	SC17-04 SG /coarse grain	8 ± 4	0.45 ± 0.01	1.47 ± 0.02	6.51 ± 0.06	-	0.59 ± 0.01	0.74 ± 0.07	1.33 ± 0.01
O-15	SC19-01 SG /coarse grain	8 ± 4	0.65 ± 0.01	1.40 ± 0.02	8.91 ± 0.09	-	0.76 ± 0.01	0.69 ± 0.07	1.45 ± 0.01
O-16	SC19-02 SG /coarse grain	8 ± 4	0.70 ± 0.01	1.42 ± 0.02	8.60 ± 0.09	-	0.79 ± 0.01	0.78 ± 0.08	1.57 ± 0.01

5. References

Aitken, M.J., 1998. An Introduction to Optical Dating: The Dating of Quaternary Sediments by the Use of Photon-stimulated Luminescence. Oxford University Press, Oxford, 267 p.

Bachellerie, F., Caux, S., Crevecoeur, I., Gravina, B., Mallol, C., Maureille, B., Michel, A., Rougier, H., Tartar, E., Teyssandier, N., Bordes, J.G., Morin, E., 2014. Preliminary results from ongoing excavations at La Roche-à-Pierrot, Saint-Césaire. Poster presented at the XVII World UISPP Congress, Burgos, Spain, 1-7 September 2014.

Backer, A.M., 1993. Spatial distributions at La Roche à Pierrot, Saint-Césaire: Changing uses of a Rockshelter. In: Lévêque, F, Backer, A.M. and Guilbaud, M. (Eds.), Context of a Late Neandertal. Implications of Multidisciplinary Research for the Transition to Upper Paleolithic Adaptations at Saint-Césaire, Charente-Maritime, France, Monographs in World Archaeology n°16, Prehistory Press, Madison, pp. 105-127.

Backer, A.M., 1994. Site structure of Saint-Césaire: changing uses of a paleolithic rockshelter. PhD dissertation, University of New Mexico, 506 p.

Backer, A.M., 1997. Rapport sur le Sauvetage Urgent de 1997, Saint-Césaire (Charente-Maritime), rapport de fouilles programmées. DRAC Poitou-Charentes, SRA, 27 p.

Batschelet, E., 1981. Circular Statistics in Biology. Academic Press, London, 371 p.

Bish, D.L., 1993. Studies of clays and clay minerals using X-ray powder diffraction and the Rietveld method. In: Computer Applications to X-ray Powder Diffraction Analysis of Clay Minerals, Reynolds, Jr. R.C. and Walker, J.R. (Eds.), CMS workshop, lectures 5, pp. 79-112.

Couillet, A., Rougier, H., Todisco, D., Marot, J., Gillet, O., Crevecoeur, I., 2022. New Visual Analytics Tool and Spatial Statistics to Explore Archeological Data: The Case of the Paleolithic Sequence of La Roche-à-Pierrot, Saint-Césaire, France. Journal of Computer Applications in Archaeology, 5(1), 19-34.

Crevecoeur, I. 2017. Reprise des fouilles à La Roche-à-Pierrot, Saint-Césaire. In: Le troisième Homme, Cleyet-Merle, J.J., Shunkov, M.V., Geneste, J.M., Derevianko, A.P., Slimak, L., Krivoshapkin, A.I., Gravina, B., Turq, A., Maureille, B. (Eds.), Préhistoire de l'Altaï, Editions de la Réunion des musées nationaux, Grand Palais, Paris, p. 107.

Dietze, M., Kreutzer, S., Burow, C., Fuchs, M.C., Fisher, M., Schmidt, C. 2016. The abanico plot: Visualising chronometric data with individual standard errors. Quaternary Geochronology, 31, 12-18.

Duller, G.A.T., 2003. Distinguishing quartz and feldspar in single grain luminescence measurements, Radiation Measurements, 37(2), 161-165.

Fisher, N.I., 1993. Statistical Analysis of Circular Data. Cambridge University Press, Cambridge, 296 p.

Galbraith, R.F., Green, P.F., 1990. Estimating the component ages in a finite mixture. International Journal of Radiation Applications and Instrumentation. Part D. Nuclear Tracks and Radiation Measurements, 17(3), 197-206.

Galbraith, R.F., Roberts, R.G., Laslett, G.M., Yoshida, H., Olley, J.M., 1999. Optical dating of single and multiple grains of quartz from Jinmium rock shelter, northern Australia. Part I, Experimental design and statistical models. Archaeometry, 41(2), 339-364.

Guérin, G., Christophe, C., Philippe, A., Murray, A.S., Thomsen, K.J., Tribolo, C., Urbanová, P., Jain, M., Guibert, P., Mercier, N., Kreutzer, S., Lahaye C., 2017. Absorbed dose, equivalent dose, measured dose rates, and implications for OSL age estimates: Introducing the Average Dose Model. Quaternary Geochronology, 41, 163-173.

Guibert, P., Lahaye, C., Bechtel, F., 2009. The importance of U-series disequilibrium of sediments in luminescence dating: a case study at the Roc de Marsal Cave (Dordogne, France). Radiation Measurements, 44(3), 223-231.

Guibert, P., Schvoerer, M., 1991. TL dating: Low background gamma spectrometry as a tool for the determination of the annual dose. International Journal of Radiation Applications and Instrumentation. Part D, Nuclear Tracks and Radiation Measurements, 18(1), 231-238.

Kovach, W.L., 2011. Oriana–circular statistics for windows, version 4, Kovach Computing Services, Pentraeth, Wales, UK.

Kreutzer, S., Schmidt, Fuchs, M.C., C., Dietze, M., Fisher, M., Fuchs, M., 2012. Introducing an R package for luminescence dating analysis, Ancient TL, 30(1), 1-8.

Landler, L., Ruxton, G. D., Malkemper, E.P., 2018. Circular data in biology: advice for effectively implementing statistical procedures. Behavioral Ecology and Sociobiology, 72, 128, 1-10.

Lenoble, A., 2005. Ruissellement et formation des sites préhistoriques: référentiel actualiste et exemples d'application au fossile. BAR Publishing (British Archaeological Reports International Series), Oxford, England, 212 p.

Lévêque, F., 1993. The Castelperronian industry of Saint-Césaire: the upper level. In: Lévêque, F, Backer, A.M. and Guilbaud, M. (Eds.), Context of a Late Neandertal. Implications of Multidisci-plinary Research for the Transition to Upper Paleolithic Adaptations at Saint-Césaire, Charente-Maritime, France, Monographs in World Archaeology n°16, Prehistory Press, Madison, pp. 23-26.

Lévêque, F., 2002. Méthodes de fouilles. In: Géologie de la préhistoire: Méthodes, techniques, applications, Miskovsky, J.C. (Ed.), Géopré, Presses universitaires de Perpignan, Paris, pp. 415-423.

Menzies, J., 2000. Micromorphological analyses of microfabrics and microstructures indicative of deformation processes in glacial sediments. Geological Society, London, Special Publications, 176(1), 245-257.

Miskovsky, J.C., Lévêque, F., 1993. The sediments and stratigraphy of Saint-Césaire: contributions to the paleoclimatology of the site. In: Lévêque, F, Backer, A.M. and Guilbaud, M. (Eds.), Context of a Late Neandertal. Implications of Multidisciplinary Research for the Transition to Upper Paleolithic Adaptations at Saint-Césaire, Charente-Maritime, France, Monographs in World Archaeology n°16, Prehistory Press, Madison, pp. 9-14.

Murray, A.S., Wintle, A.G., 2000. Luminescence dating of quartz using an improved single-aliquot regenerative-dose protocol. Radiation Measurements, 32(1), 57-73.

Murray, A.S., Wintle, A.G., 2003. The single aliquot regenerative dose protocol: potential for improvements in reliability. Radiation Measurements, 37(4), 377-381.

Nicosia, C., Stoops, G., (Eds.), 2017. Archaeological Soil and Sediment Micromorphology. Wiley Blackwell, Chichester, UK, 496 p.

R Development Core Team, 2015. R; A Language and Environment for Statistical Computing. Vienna, Austria. URL: http://CRAN.R-project.org.

Rietveld, H.M., 1969. A profile refinement method for nuclear and magnetic structures. Journal of Applied Crystallography, 2, 65-71.

Stoops, G., 2003. Guidelines for Analysis and Description of Soil and Regolith Thin Sections. Soil Science Society of America, Madison, Wisconsin, USA, 184 p.

Stoops, G., Marcelino, V., Mees, F., 2010. Micromorphological Features and Their Relation to Processes and Classification: General Guidelines and Keys. In: Stoops, G., Marcelino, V., and Mees, F. (Eds.), Interpretation of Micromorphological Features of Soils and Regoliths, 2nd Edition, Elsevier, pp. 15-35.

Thomsen, K.J., Murray, A.S., Bøtter-Jensen, L., 2005. Sources of variability in OSL dose measurements using single grains of quartz. Radiation measurements, 39(1), 47-61.

Tribolo, C., Mercier, N., Valladas, H., 2001. Alpha sensitivity determination in quartzite using an OSL single aliquot procedure. Ancient TL, 19(2), 47-50.

Wintle, A.G., Murray, A.S., 2006. A review of quartz optically stimulated luminescence characteristics and their relevance in single aliquot regeneration dating protocols. Radiation Measurements, 41(4), 369-391.

Young R.A., 1993. The Rietveld Method. International Union Crystallography. Oxford University Press, New York, 298 p.

Zar, J.H., 2010. Biostatistical Analysis, 5th Edition. Pearson Prentice-Hall, Upper Saddle River, 944 p.